

2-14-2022

## Therapeutic Approaches to Alter Mineral Formation and Growth in Vascular Calcification

Amirala Bakhshiannik  
*Florida International University*, [abakh002@fiu.edu](mailto:abakh002@fiu.edu)

Follow this and additional works at: <https://digitalcommons.fiu.edu/etd>



Part of the [Medical Molecular Biology Commons](#), [Molecular, Cellular, and Tissue Engineering Commons](#), and the [Pharmaceutical Preparations Commons](#)

---

### Recommended Citation

Bakhshiannik, Amirala, "Therapeutic Approaches to Alter Mineral Formation and Growth in Vascular Calcification" (2022). *FIU Electronic Theses and Dissertations*. 4932.  
<https://digitalcommons.fiu.edu/etd/4932>

This work is brought to you for free and open access by the University Graduate School at FIU Digital Commons. It has been accepted for inclusion in FIU Electronic Theses and Dissertations by an authorized administrator of FIU Digital Commons. For more information, please contact [dcc@fiu.edu](mailto:dcc@fiu.edu).

FLORIDA INTERNATIONAL UNIVERSITY

Miami, Florida

THERAPEUTIC APPROACHES TO ALTER MINERAL FORMATION AND GROWTH IN  
VASCULAR CALCIFICATION

A dissertation submitted in partial fulfillment of

the requirements for the degree of

DOCTOR OF PHILOSOPHY

in

BIOMEDICAL ENGINEERING

by

Amirala Bakhshiannik

2022

To: Dean John L. Volakis  
College of Engineering and Computing

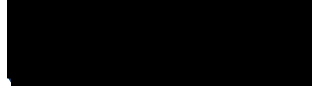
This dissertation, written by Amirala Bakhshiannik, and entitled Therapeutic Approaches to Alter Mineral Formation and Growth in Vascular Calcification, having been approved in respect to style and intellectual content, is referred to you for judgment.

We have read this dissertation and recommend that it be approved.

  
Jessica Ramella-Roman

  
DocuSigned by: Sharan Ramaswamy

  
Arvind Agarwal

  
DocuSigned by: Prem Chapagain

  
Joshua D. Hutcheson, Major Professor

Date of Defense: February 14, 2022

The dissertation of Amirala Bakhshiannik is approved.

---

Dean John L. Volakis  
College of Engineering and Computing

---

Andrés G. Gil  
Vice President for Research and Economic Development  
and Dean of the University Graduate School

Florida International University, 2022

© Copyright 2022 by Amirala Bakhshiannik

All rights reserved.

DEDICATION

To Azi, Pedar, Asal, and Soroush.

## ACKNOWLEDGMENTS

I would like to acknowledge my PhD advisor, Dr. Joshua D. Hutcheson, all of lab mates in Cardiovascular Matrix Remodeling Laboratory, Department of Biomedical Engineering, and University Graduate School at Florida International University for awarding Dissertation Year Fellowship. I also would like to extend my gratitude to our collaborators at University College London and University of Chicago.

ABSTRACT OF THE DISSERTATION  
THERAPEUTIC APPROACHES TO ALTER MINERAL FORMATION AND GROWTH IN  
VASCULAR CALCIFICATION

by

Amirala Bakhshiannik

Florida International University, 2022

Miami, Florida

Professor Joshua D. Hutcheson, Major Professor

Cardiovascular diseases represent the global leading cause of morbidity and mortality. Cardiovascular calcification is the most significant predictor of cardiovascular events, but no therapeutic options exist to prevent or treat mineral formation in the vasculature. The presence of bone-like mineral increases cardiac work required to move blood through systemic circulation and can lead to mechanical stress in atherosclerotic plaques, promoting plaque rupture events that cause heart attacks. Clinical trials correlated bisphosphonates (BiPs), common anti-osteoporosis pharmaceuticals, with contradicting cardiovascular outcomes. Here, we demonstrated the importance of treatment timing in BiP-induced mineral disruption or promotion. We showed that BiPs can alter morphological features of calcifications within the atherosclerotic plaque of hyperlipidemic mice, which may affect plaque rupture risk.

Osteogenic differentiation of resident vascular smooth muscle cells (VSMCs) and release of calcifying extracellular vesicles (EVs) mediate cardiovascular calcification, which imitates bone mineralization by osteoblasts. Formation of calcifying EVs by VSMCs requires caveolin-1 (CAV1), a scaffolding membrane protein. Targeting cellular mechanisms that involve CAV1 may represent ideal strategies to develop therapeutics for cardiovascular calcification.

We studied the effect of inhibiting several upstream and downstream molecules that are involved in CAV1 activation and trafficking. Interestingly, we showed that altering CAV1 trafficking does not negatively impact physiological mineralization of osteoblasts. We concluded that despite

shared mineralization characteristics, the mechanism(s) of bone and vascular calcification is/are distinct.

Furthermore, we demonstrated that epidermal growth factor receptor (EGFR) inhibition prevents vascular calcification by mitigating the biogenesis of calcifying EVs. We showed that EGFR inhibition reduces the release of pro-calcific CAV1-positive EVs and prevents calcification in osteogenic VSMC cultures and in chronic kidney disease mice fed a high-phosphate diet. EGFR inhibitors are clinically approved and widely used in cancer therapies and may represent an appropriate strategy to treat vascular calcification.

## TABLE OF CONTENTS

CHAPTER	PAGE
Chapter I: Introduction and Motivation .....	1
1.1. Statement of Problem.....	1
1.2. Specific Aims.....	2
Chapter II: Background.....	4
2.1. Pathological vs. Physiological Calcification .....	4
2.2. Calcification: Matrix Vesicles vs. Extracellular Vesicles.....	6
2.3. EVs with Non-Osteogenic Origins.....	9
2.4. Calcifying EVs in Cardiovascular Calcification.....	10
2.5. Smooth Muscle Cell-derived vesicles.....	12
2.6. Valvular Interstitial Cell-derived Vesicles.....	13
2.7. Macrophage-derived Vesicles.....	14
2.8. Summary .....	15
Chapter III: Aim 1 – Time-dependent Role of Bisphosphonates in Cardiovascular Calcification	17
3.1. Introduction .....	17
3.2. Methods.....	19
3.3. Results.....	22
3.4. Discussion .....	31
3.5. Summary .....	34
Chapter IV: Aim 2 – Mechanistic Study on Calcifying Extracellular Vesicle Biogenesis .....	35
4.1. Introduction .....	35
4.2. Methods.....	37
4.3. Results.....	41
4.4. Discussion .....	54
4.5. Summary .....	57
Chapter V: Aim 3 – Epidermal Growth Factor Receptor Inhibition Prevents Vascular Calcification.....	58
5.1. Introduction .....	58
5.2. Methods.....	60
5.3. Results.....	69
5.4. Discussion .....	83
5.5. Summary .....	86

Impact and Future Studies .....	87
References .....	88
Appendices .....	102
VITAE.....	107

## LIST OF TABLES

TABLE	PAGE
Table 1. Bone structural parameters for BiP-treated and control groups.....	30
Table 2. Summary statistics of each MR regression in the MESA cohort.....	70
Table 3. Summary statistics of each MR regression in the Framingham Heart Study (FHS).. ....	71
Table 4. Bone structural parameters for control, CKD, and EGFR-treated groups.....	82

## LIST OF FIGURES

FIGURE	PAGE
Figure 1. Schematic of EVs contributing to calcification.....	9
Figure 2. BiP treatment increases the plaque calcification in Apoe <sup>-/-</sup> mice.....	23
Figure 3. BiP treatment alters the micromorphology of the minerals in the plaque.....	24
Figure 4. BiP treatment affects the mineral morphology differently in males and females.....	26
Figure 5. BiP treatment does not affect the serum TNAP activity and total cholesterol. ....	27
Figure 6. Bone remodeling positively correlates with duration of BiP treatment.....	29
Figure 7. CAV1 silencing in osteoblasts does not prevent in vitro calcification. ....	42
Figure 8. Src tyrosine kinase inhibitor prevents in vitro calcification of VSMCs.....	43
Figure 9. Calpain inhibitor prevents in vitro calcification of VSMCs.....	45
Figure 10. ROCK inhibitor prevents in vitro calcification of VSMCs.....	47
Figure 11. Rac1 inhibitor prevents in vitro calcification of VSMCs.....	49
Figure 12. M $\beta$ CD increases in vitro calcification of VSMCs.....	51
Figure 13. M $\beta$ CD prevents in vitro calcification of osteoblasts.....	53
Figure 14. Serum EGFR positively correlates with coronary artery calcification. ....	72
Figure 15. EGFR inhibition prevents vascular calcification <i>in vivo</i> and <i>in vitro</i> .....	74
Figure 16. EGFR inhibition modulates CAV1 trafficking in VSMCs.....	76
Figure 17. EGFR inhibition redistributes CAV1 and TNAP <i>in vivo</i> .....	78
Figure 18. EGFR inhibition does not prevent osteoblast in vitro calcification.....	80
Figure 19. EGFR inhibition reverses deleterious effects on physiological bone mineralization...	81

## **Chapter I: Introduction and Motivation**

### **1.1. Statement of Problem**

Cardiovascular diseases represent the global leading cause of morbidity and mortality. Cardiovascular calcification is the most significant predictor of cardiovascular events but lacking available therapeutic options. Osteogenic differentiation of resident vascular smooth muscle cells (VSMCs), which elevates the expression of the genes, proteins, and enzymes required for mineralization, mediates cardiovascular calcification, which imitate bone mineralization by osteoblasts [1-3]. Pathological conditions, including aging, atherosclerosis, chronic kidney disease, bone disorders, and diabetes, may stimulate osteogenic alteration of VSMCs [4]. Release of calcifying extracellular vesicles, small organelles liberated by VSMCs and macrophages, promotes cardiovascular calcification [5]. Calcifying EVs in a collagen-rich extracellular matrix (ECM) initiate the calcification [2]. EV formation requires caveolin-1 (CAV1), a membrane scaffolding protein; CAV1 resides in caveolar domain, flask-shaped membrane invaginations, which regulate the membrane tension and intracellular vesicle trafficking. However, calcifying EV origin and formation mechanism(s) are unclear, which limit the development of therapeutic interventions for vascular calcification. Interestingly, the appearance of cardiovascular calcification correlates highly with decrease in bone mineral density, known as the calcification paradox [6]. Therefore, therapeutics designed to interfere with the formation of mineral in the cardiovascular system may show potential off-target effects on bone mineralization and vice versa. Of note, clinical trials revealed that bisphosphonates (BiPs), common anti-osteoporosis pharmaceuticals, can elicit unexpected cardiovascular events [7-9]. The positive cardiovascular outcomes in some patients warrant investigation to discover how BiPs associate with cardiovascular calcification. The current PhD dissertation addresses the gap of knowledge on the role of BiPs on cardiovascular calcification,

studies the mechanism of calcifying EV formation, and introduces a potential target to prevent vascular calcification.

## **1.2. Specific Aims**

We hypothesize that bisphosphonates (BiPs) contradicting outcomes originate from their interactions with minerals, which lead to major changes in mineral morphology. Though they do not present reliable therapeutic strategies to prevent cardiovascular calcification. Given the role of caveolin-1 (CAV1) in biogenesis of calcifying extracellular vesicles (EVs) in vascular smooth muscle cells (VSMCs), molecules which affect CAV1 activation and trafficking, specifically epidermal growth factor receptor (EGFR), represent ideal targets to prevent cardiovascular calcification. We will assess this hypothesis through the following specific aims:

***Specific Aim 1.*** Test the hypothesis that BiPs interact with cardiovascular calcification and stimulate mineral nucleation and growth in a time-dependent manner. Previous studies reported that BiPs lead to either positive or negative cardiovascular outcomes. Patients with no prior cardiovascular events appear to be protected from future events by BiPs, yet patients with a history of cardiovascular disease have worsened outcomes. However, a systematic and longitudinal study on the off-target effect(s) of BiPs on cardiovascular calcification has not been reported. We will perform a longitudinal study on a mouse model of atherosclerotic plaque calcification to investigate the time-dependency of BiP on *in vivo* calcification.

***Specific Aim 2.*** Assess the role of CAV1 interactors in VSMC-dependent calcification. The biogenesis of calcifying EVs from VSMC requires the presence of CAV1, the major scaffolding protein within plasma membrane invaginations, known as caveolar domains. Previous studies reported the interactions between CAV1 and Src family kinases, actin-binding protein filamin A, and Rho family of GTPases (including Rho-A protein kinase and Rac1) in various cell lines. In this aim, we will assess the role of Src tyrosine kinase, FLNA, Rho-associated protein kinase, Rac1, and methyl- $\beta$ -cyclodextrin (direct targeting of caveolar domains) in VSMC-dependent

calcification. Furthermore, we will investigate the off-target effects of these molecules on osteoblast mineralization. This aim will help us to identify new targets that specifically affect cardiovascular calcification without affecting physiological bone mineralization.

**Specific Aim 3.** Test the hypothesis that EGFR inhibition prevents caveolar domain endocytosis and the subsequent formation of calcifying EVs in VSMCs. EGFR is a well-known CAV1 interactor and resides in caveolar domains, thus, it may play a role during calcifying EV formation by VSMCs. Furthermore, EGFR inhibitors are associated with safe clinical therapies, which may provide a new approach for ectopic vascular mineralization. Of Note, calcification of arterial media commonly occurs in patients with chronic kidney disease (CKD). CKD patients with no detectable vascular calcification have 8-year all-cause survival rates of ~90% compared to 50% survivability in age-matched patients with medial calcification. In this aim, we will investigate the mechanism through which EGFR inhibition prevents VSMC-dependent calcification *in vitro* and *in vivo* in a CKD mouse model.

**Impact.** The proposed study will provide profound understanding of bisphosphonate effect(s) on cardiovascular calcification, reveal new mechanistic insight into calcifying EV formation, and test the efficacy of targeting the EGFR for therapeutic benefit in vascular calcification. CKD patients develop widespread vascular calcification and represent an appropriate population for future trials on repurposing EGFR inhibition for cardiovascular benefit.

## **Chapter II: Background**

### **2.1. Pathological vs. Physiological Calcification**

Calcification, the accumulation of calcium mineral, occurs primarily during either bone remodeling or pathological cardiovascular calcification. Interestingly, the appearance of calcific mineral in cardiovascular tissues associates strongly with a decrease in bone remodeling, a phenomenon known as the calcification paradox [10]. Despite this inverse relation, research in cardiovascular calcification has been informed by pioneering research in bone physiology. The striking similarities in cellular phenotypic changes and mineral deposition in the two tissues only further underscore the confusion surrounding the underlying causes of the paradox. In this section, we briefly introduce the general mineralization in either tissues and elaborate the fundamental building block of mineral, i.e. calcifying vesicles [11, 12].

#### ***Atherosclerotic plaque Calcification***

Atherosclerosis refers to the formation of fibrous cap in arterial intima, leading to focal elastin degradation, lumen deformation, and ultimately arterial occlusion [13-15]. Plaque calcification manifests as formation of calcium minerals within the atherosclerotic lesion [16]. Aging, hypertension, dyslipidemia, and inflammation increase the risk of atherosclerotic intimal calcification [13, 14, 17, 18]. Vascular smooth muscle cells (VSMCs) and macrophages play important role in plaque calcification [18]. Morphology and the size of minerals within the plaque determine its vulnerability to rupture and thrombosis [13, 14]. Cell apoptosis, stimulatory osteogenic proteins, calcium and phosphate ions, and lipids promote the intimal calcification. In general, apoptosis activates phagocytosis; however, oxidized lipids within the atherosclerotic plaque disrupt the phagocytosis [16, 19]. VSMCs and macrophages also produce oxidized low density lipoproteins (LDLs) [20]. Foam cells and cholesterol-enriched macrophages accumulate in intima hemodynamically preferable sites, at the onset of lesion formation. Later on, the plaque

develops to an developed plaque, which contains lipid-rich necrotic core with sporadic calcified spots surrounded by fibrotic cap of VSMCs and ECM [19].

### ***Medial Calcinosis***

The media is next to the intima and has a multi-layered structure starting with elastin fibrils in the basement, a complex of elastic laminae, vascular smooth muscle cells, collagen type I fibrils, and proteoglycans in the middle, and ended with an elastic lamina [14, 15, 21]. Media calcification represents the elastin degradation and formation of calcific minerals by vascular smooth muscle cells. Aging, chronic kidney disease (CKD), and diabetes mellitus mediate the medial calcinosis [13, 17, 18]. VSMCs adapt an osteogenic differentiation during medial calcification [22], which leads to mineral formation along elastic laminae, as the most probable site, and develops to a circumferential calcium crystals sheet [16]. Cell apoptosis provides also calcium and phosphate ions to continue the calcification process. Furthermore, lack of phagocytosis due to elastin barrier for local VSMCs and pH-imbalance accelerate media calcification [16].

### ***Cardiac valve calcification***

Cardiac valves maintain the physiological blood flow during the cardiac cycles. Aortic, pulmonary, and tricuspid valves contain three leaflets, while mitral valve is bicuspid [15]. The maximum thickness of the leaflets is 1 mm and consists of the fibrosa with circumferentially aligned collagen fibers, the spongiosa with proteoglycan and glycosaminoglycan contents, and ventricularis mainly composed of elastin [15, 23]. Valve endothelial and interstitial cells contribute in the valvular calcification [23]. Endothelial cells function as the entrance for inflammatory agents into the leaflet. Interstitial cells present in all three layers of the valve and maintain the microstructure of leaflet by ECM hemostasis; in pathological condition, these cells gain contractile cytoskeletal rearrangement by upregulation of the  $\alpha$ -smooth muscle actin and myosin heavy chain, which leads to imbalance ECM turnover, excreting more force to ECM, and ultimately fibrotic collagen accumulation,

elevated osteogenic markers, and calcification [23, 24]. Lipid accumulation including LDL and lipoprotein in the valve interstitium due to interrupted endothelium initiates valvular calcification. Further oxidation of lipoproteins, activation of inflammatory cells (macrophages and T lymphocytes), degradation of native ECM result in ultimate valvular mineralization [25].

### ***Bone mineralization***

The extracellular matrix of the bone mainly consists of the collagen fibers, non-collagenous proteins (proteoglycans, glycoproteins, Gla-proteins), trace amount of phospholipids, and hydroxyapatite [26, 27]. The feedback stimuli between cellular activity and ECM formation result in bone mineralization [27]. In physiological condition, osteoblasts (bone forming cells) mediate matrix mineralization, while the osteoclasts (bone absorbing cells) degrade the mineral. The interplay between these two cell types regulates bone remodeling [26, 27]. Osteoblasts release osteogenic and mineral precursors, also known as matrix vesicles, to promote mineralization [28]. Lysosomes play key role in biogenesis and intracellular trafficking of matrix vesicles. Formation of amorphous calcium phosphate starts in intracellular matrix vesicles and crystallization occurs after release into the ECM [28].

## **2.2. Calcification: Matrix Vesicles vs. Extracellular Vesicles**

Text for this section taken from:

[2] – A. Bakhshian Nik, J.D. Hutcheson, and E. Aikawa, 2017. Extracellular vesicles as mediators of cardiovascular calcification. *Frontiers in cardiovascular medicine*, 4, p.78.

Bonucci reported the appearance of “roundish bodies” in initiation of the calcification process in guinea pig and rat tibial-femoral epiphyseal plates in 1967 [29]. One year later, Anderson used electron microscopy on tissue sections to demonstrate vesicular structures in the mouse cartilage epiphysis [30]. Bone mineralization depends on secretion of matrix vesicles (MVs), with diameter of 30-400 nm [31, 32], from chondrocytes, osteoblasts, odontoblasts, tenocytes, and cementoblasts [33]. MVs released from specific sites on cell membranes (apical microvilli [31]) exhibit similar

cytosolic and plasma membrane profiles apparent in their cell of origin [34]. Compared to their parent cells, MVs carry augmented levels of acidic lipids such as phosphatidylserine (PS) and sphingomyelin, but diminished levels of neutral phospholipids of phosphatidylcholine and lysophospholipids [33]. Chondrocytes residing in the epiphyseal plate experience hypoxic conditions due to presence of collagen fibrils and proteoglycans, which restrict oxygen and nutrients delivery [35]. Development of blood microvessels into this zone creates oxidative stress caused by the sudden elevation in nutrients, oxygen, calcium ions ( $\text{Ca}^{2+}$ ) and phosphate ions (Pi). This process leads to formation of  $\text{Ca}^{2+}$ -enriched mitochondria, which results in secretion of  $\text{Ca}^{2+}$ -loaded vesicles into the cytosol. Formation of complexes of PS and  $\text{Ca}^{2+}$  either with Pi or annexins, diminishes the  $\text{Ca}^{2+}$  level within the cytosol, expedites actin depolymerization, and consequently MV pinch off, and their release into the extracellular environment [35]. Of note, apoptotic bodies originating from apoptotic cell membrane rearrangement during terminal stage of mineralization in epiphyseal plate differs from active formation and release of MVs [36]. Released MVs interact with glycosaminoglycans and propagate mineralization [37].

Chondrocyte differentiating factors such as thyroxine (T3), bone morphogenetic protein 6 (BMP-6), retinoic acid, and Indian hedgehog may give rise to MV generation by inducing changes in cell phenotypes [38]. Osteogenic cell types abundantly express annexin I, II, IV, V, VI, and VII. These proteins exhibit a high affinity to MV membrane, whereupon MVs bind to phospholipids and regulate mineralization. Specifically, annexins function either as voltage-gated channels or  $\text{Ca}^{2+}$  binding, mediate inflammation responses, and regulate structural properties of both cellular and MV membranes [32, 37, 39]. The most abundant proteins in MVs are annexins II, V, and VI which can accelerate the calcification process by providing required  $\text{Ca}^{+2}$  for mineralization. Additionally, other membrane proteins such as calbindin D9k can provide  $\text{Ca}^{2+}$  for MVs [40].

Pyrophosphate (PPi), originating from nucleotide pyrophosphatase phosphodiesterase (NPP1) hydrolysis of nucleoside triphosphates inhibits mineralization. Progressive ankylosis (ANK) carries PPi into extracellular milieu. Tissue non-specific alkaline phosphatase (TNAP, on the outer leaflet

of MV membranes) hydrolyzes PPi into free phosphate (Pi) and providing free Pi for complexing with  $\text{Ca}^{+2}$  and mineral formation [33, 35, 41]. Type III Na/Pi transporters (PiT-1) on the MV membrane facilitate Pi internalization. Bone morphogenetic protein 2 (BMP-2) and parathyroid hormone upregulate expression of these transporters [35]. Additionally, MVs contain phosphatases and membrane phosphohydrolases, such as TNAP, AMPase, ATPase, nucleoside triphosphate pyrophosphohydrolase (NTPPase, NPP1, and PC-1), and PHOSPHO-1 that elevate the intravesicular Pi concentration within the MVs [33, 42]. This highly concentrated environment, adjacent to the MV membrane, where  $\text{Ca}^{2+}$  and Pi meet, facilitates calcium phosphate precipitation followed by an increase in pH and mineral stabilization. Membrane associations are mediated by PS located on the luminal side of the MV lipid bilayer. PS is an anionic phospholipid with tendency to bind  $\text{Ca}^{2+}$ . The complexes of PS- $\text{Ca}^{2+}$ -Pi may serve as initial nuclei for hydroxyapatite precipitation [35, 39, 43]. Studies have also suggested that the mineralization process can begin intracellularly with contribution of pre-nucleation clusters within endosomes, which initiate mineralization in order to maintain  $\text{Ca}^{2+}$  and Pi in homeostatic concentration and fulfill energy trade-off [33].

During bone formation, extracellular matrix (ECM) remodeling facilitates homeostasis and angiogenesis. MVs are equipped with matrix metalloproteases (MMPs) that degrade and remodel the ECM [31, 44]. Particularly, MMP-2, MMP-3, MMP-9, and MMP-13 are located in MV membranes and play a key role in matrix remodeling and propagation of mineralization [33, 44, 45]. In ECM, collagen fibrils and proteoglycans provide charged regions, which are favorable sites for accumulation of the calcium phosphate nanoparticle clusters that form in MVs. The amorphous apatite resulting from this accumulation transforms into structured and crystalline mineral following ECM associations [33]. MVs interact with ECM proteins via their integrin receptors and surface motifs such as CD9, CD63, and Hsp70 [33] (**Fig. 1**). In addition to their remodeling potential and ECM binding, MVs in growth plate ECM can affect the proliferation and fate of resident cells, due to the activation of parathyroid hormones and gene-related peptide through their

loaded proteins [33]. This paracrine signaling property is like other subtypes of extracellular vesicles (EVs) ubiquitous to many cells and tissues.

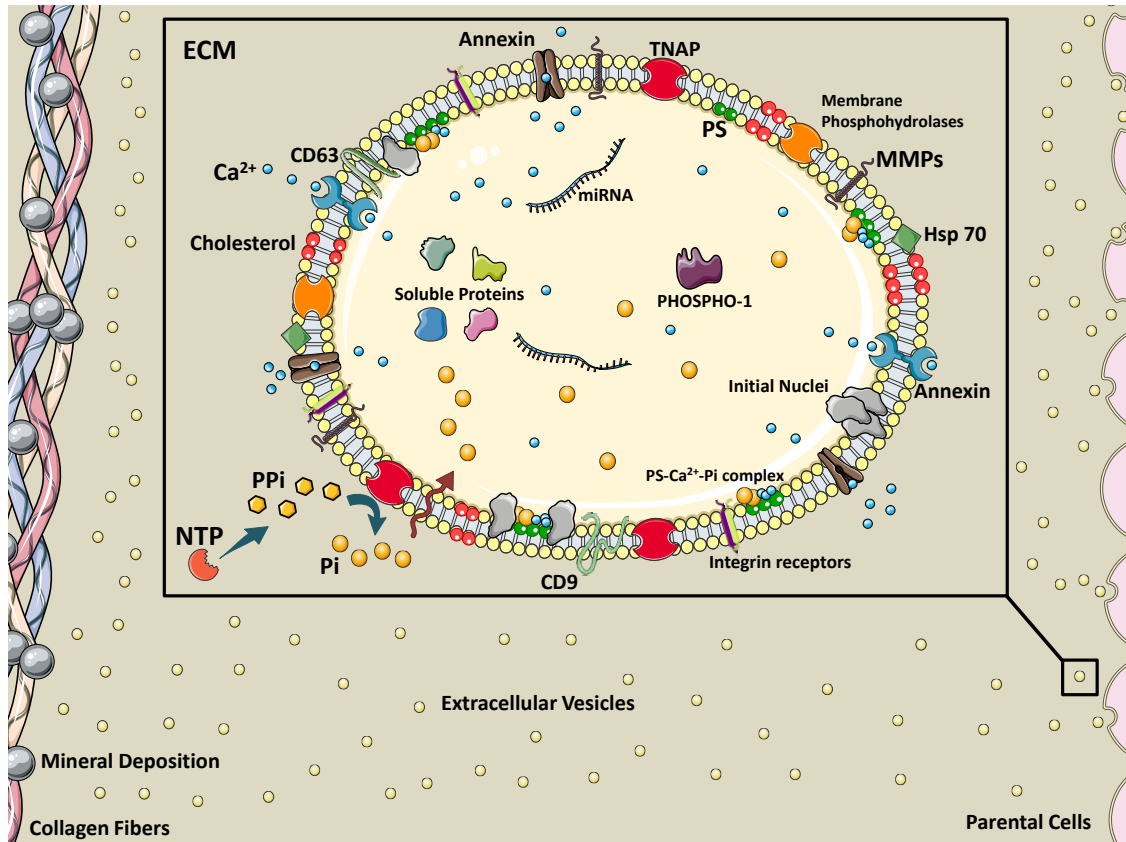


Figure 1. Schematic of EVs contributing to calcification. Osteogenic cells release EVs into ECM to nucleate bone or cardiovascular mineral. EV membrane contains a specific lipid profile that differs from parent cells. Annexins on EVs facilitate  $\text{Ca}^{2+}$  entrance, and tissue non-specific alkaline phosphatase (TNAP) activity converts PPI to phosphate ions (Pi), thereby providing the necessary ionic components for mineralization. PiT-1 transporters transfer Pi into the EV lumen. Coincidence of these ions and formation of  $\text{Ca}^{2+}$ -PS-Pi within the EV lead to mineral nucleation. Membrane enzymes and proteins interact with and attach to the ECM, directing the localization of calcification. Figure created using Servier Medical Art images (smart.servier.com).

### 2.3. EVs with Non-Osteogenic Origins

MVs represent one specific subtype of EVs. Generally, EVs function to maintain both intracellular and extracellular homeostasis. Two major mechanisms control EV release into the ECM: (i)

multivesicular bodies (MVB), containing several EVs wrapped by plasma membrane; and (ii) direct budding of a single EV from cellular plasma membrane [32]. Depending on the release mechanism, EVs are generally referred to as either exosomes or microparticles, respectively. Both EV types carry a subset of cargos representing their parental cell [37, 46]. EV cargo consists of a metabolically active membrane and an inner core, which typically carries RNAs, soluble and transmembrane proteins, and lipids [37, 46, 47]. MVB trafficking and fusion/fission from the plasma membrane requires activity of Rab GTPases, specifically Rab27a, Rab27b, Rab35, and Rab11 [48, 49]. EVs often contain sets of small RNAs, such as miRNA, tRNA, mRNA, piRNA, snRNA, Y-RNA, and vault RNA, which can be protected from RNase degradation and encoded at target cells [49, 50]. The difference in RNA ingredients of parental cells and EV cargo demonstrates the selective mechanism of RNA loading. EV RNA cargo can serve as biomarker that indicate the phenotypic state of parental cells, as well as messengers that can interact with other cells [49]. EVs play a key role in cell-cell interaction and data trafficking in both normal and pathological conditions. For instance, miRNA-enriched EVs from endothelial cells can regulate gene expression and resultant phenotypic transitions in smooth muscle cells [51]. Divergence from normal physiological conditions toward pathological ones, induces release of dysfunctional EVs with pathologic cargo and may affect tissue homeostasis and cellular phenotypes [32].

#### **2.4. Calcifying EVs in Cardiovascular Calcification**

Calcification contributes to pathological remodeling in different locations throughout the cardiovascular system, such as the arterial intima and media and the aortic valve [5, 52]. Numerous studies have demonstrated similarities between cardiovascular calcification and bone metabolism; similar to the bone, EVs may regulate the pathological calcification process within cardiovascular tissues [53]. In pathological environment, cells may have increased intercellular  $\text{Ca}^{2+}/\text{Pi}$  concentrations, thus to alleviate this condition, they release EVs with high levels of these ions [54]. Similar to bone, annexins present on calcifying EVs play a dual role of  $\text{Ca}^{2+}$  uptake and

counteracting the calcification inhibitory activity of fetuin-A during ectopic mineralization [32, 37]. High phosphate imbalance present in chronic kidney disease, may accelerate calcification nucleation in EVs [11]. In this condition, TNAP activity may accelerate the calcification process in both non-osteogenic and osteogenic EVs through removing PPI, a competitive inhibitor to  $\text{Ca}^{2+}$  associations with Pi [55]. EVs with calcifying potential may also contain imbalanced and dysfunctional miRNAs, which induce the gene expression and protein synthesis of osteogenic markers such as RUNX2, Smad1, osterix, TNAP, chaperones, and pro-inflammatory factors [32, 37]. Additionally, calcification of EVs may inhibit their ability to reach their target cells, further promoting a loss in tissue homeostasis and pathological remodeling [56] (**Fig. 1**).

Electron microscopy demonstrated the presence of needlelike hydroxyapatite nanocrystals, in EVs extracted from atherosclerotic lesions of apolipoprotein E-deficient mice [57]. EVs released into the atherosclerotic lesion have a Ca/P ratio of 0.66, indicating incomplete calcification (compared to the ratio in normal adult murine bones of 1.71 [58]). High resolution microcomputed tomography imaging revealed microcalcification in the fibrous cap of atherosclerotic plaques composed of calcified EV aggregates [55, 59]. These observations indicate a role for EVs in the formation and progression of cardiovascular calcification, but mechanistic studies demonstrating causality are difficult. One major challenge in EV research is to distinguish between different EV populations such as calcifying EVs, MVs, exosomes, apoptotic bodies, and microparticles, due to their shared size and shape characteristics [60]. Application of multiple and consecutive centrifugations followed by size-based filtration and sucrose gradient-based ultracentrifugation to isolate EVs of known density have been used to separate EVs from other cellular particles [46, 61]. EVs with various sizes and densities pellet based on the centrifugation speed, i.e. large, medium, and small EVs precipitate at low, moderate, and high speeds, respectively [46]. However, these techniques are often unable to separate the various EV populations. Calcifying EVs secreted by smooth muscle cells (SMCs) cultured under osteogenic conditions exhibit increased mass density compared to other EVs, likely due to mineral formation. Therefore, calcifying EVs precipitate more quickly

under the application of ultracentrifugation (~100000xg) [60], permitting enrichment of these EVs and subsequent proteomic profiling [46, 60]. Once proteomic fingerprints are established, membrane proteins (tetraspanins), ER-related proteins, mitochondrial proteins, exosomal markers, endosomal markers, and ECM factors (surface molecules and integrins) specific to various EV populations help map and separate EVs into sub-sets based on their origins [46].

Future works are needed to improve upon EV isolation techniques to reduce noise from non-calcifying EVs. Advancements in EV characterization tools may allow careful comparative studies to understand the similarities and differences between MVs and calcifying EVs liberated from the three reported cellular contributors to calcification in cardiovascular tissues: vascular SMCs, macrophages, and valvular interstitial cells (VICs).

## **2.5. Smooth Muscle Cell-derived vesicles**

VSMCs and osteoblasts share similar mesenchymal origins, and under pathological stresses VSMCs can exhibit an osteoblast-like phenotype [62]. In a hyperphosphatemic environment (e.g., chronic kidney disease) or inflammation-driven atherosclerosis, vascular SMCs upregulate expression of osteogenic differentiating genes [63] and release EVs enriched with osteogenic biomarkers [3]. Hyperphosphatemic and osteogenic conditions decrease inhibitors such as circulating fetuin-A [64] and matrix Gla protein [65], but increase TNAP and annexins II and VI in SMC-derived EVs. Similar to its function in bone, TNAP activity leads to increased available Pi and reduction of mineralization inhibitors such as PPI [1]. The formation of calcifying EVs begins with a series of intracellular trafficking processes that load the EVs with calcification-promoting factors. A specific trafficking protein, sortilin, is a key player in the formation of calcifying EVs secreted by vascular SMCs. Sortilin transports TNAP into VSMC-derived EVs, thereby increasing EV calcifying potential [1].

Imaging techniques revealed that, once released into the ECM, VSMC-derived calcifying EVs tend to aggregate and form microcalcifications in areas with sparse collagen, whereas, large

calcifications (larger than 200  $\mu\text{m}$ ) are bordered by dense collagen fibers [5]. Large calcifications (macrocalcifications) formed by accumulation and merger of small microcalcifications, forming mature mineral. Microcalcifications that form within the fibrous cap of vulnerable atherosclerotic plaques further potentiate plaque rupture, whereas larger macrocalcifications beneath stable fibrous caps may promote plaque stability. EVs collected from SMCs cultured in pro-calcific conditions and incubated within an *in vitro* collagen hydrogel system, mimicking aspects of atherosclerotic lesions, showed the progression of calcification from single calcifying EVs to EV aggregation and fusion to the formation of microcalcifications to growth into large calcifications [5]. Collagen acts as a scaffold to direct the shape and size of the calcifications that form from this growth process [5]. Collagen fibrils, specifically type I and III in arteries, bind to EV membranes and mediate calcification propagation in the ECM [62]. In addition to binding and directing the calcification of EVs, collagen may also play a role in phenotypic changes and EV formation within SMCs [66]. Discoidin domain receptor-1 (DDR-1), a collagen receptor, regulates SMC phenotype by sensing extracellular collagen. DDR-1-depleted SMCs exhibit elevated collagen production, EV release, and mineral deposition. DDR-1 functions as a regulator of TGF- $\beta$  signaling pathways, acting as a switch between pro-fibrocalcific and anti-fibrocalcific TGF- $\beta$  signaling [66]. Therapeutic strategies to control these pathways and prevent or reverse SMC-driven calcification will require a better understanding of the mechanisms that lead to their formation within the cell, nucleation of mineral outside the cell, and the role of the ECM in calcification propagation. SMC-derived EVs are the most studied type of calcifying EVs in cardiovascular tissues and the mechanisms identified in these cells may help inform research into other cellular drivers of cardiovascular calcification.

## **2.6. Valvular Interstitial Cell-derived Vesicles**

VIC phenotypic changes play a vital role in ECM remodeling and mineral deposition that lead to calcific aortic valve disease [67]. VICs have a high phenotypic plasticity and can transform from a fibroblastic phenotype to myofibroblast- or osteoblast-like cells in response to pathological

conditions such as hyperphosphatemia and pro-inflammatory cytokines. VICs exhibit high sensitivity to their mechanical environment and undergo phenotypic changes *in vitro* in response to changes in substrate stiffness and mechanical stretch [67]. VICs may also influence valvular endothelial cells (VECs) through EV secretion. Valve homeostasis depends on appropriate interactions between VECs and VICs [67, 68]. This intercellular interaction occurs when VECs take up VICs-derived EVs containing perinuclear proteins [52]. In calcifying milieu, VICs express osteogenic mRNAs of PiT-1, RUNX2, Msx2, and TNAP[69], and pro-calcific VIC EVs resemble MVs from chondrocytes and SMCs, demonstrating elevated annexins II, V, and VI [52]. VIC-derived EVs isolated from SV40T rats demonstrated elevated calcium [69], likely reflecting the presence of annexins. Excessive extracellular Ca<sup>2+</sup> and Pi exacerbates mineralization in VIC-derived EVs [69]. Though aortic valve calcification constitutes a major unmet clinical problem, investigations into the extracellular mechanisms through which mineral nucleation and growth occurs remain scant. More studies are needed to understand the role of VIC EVs in this process and the similarities and differences between these EVs and the more well-studied SMC-derived EVs.

## **2.7. Macrophage-derived Vesicles**

Atherosclerosis creates moderate hypoxia (2-5% oxygen compare to 21% normal condition) for local cells and leads to activation of pro-inflammatory responses such as Akt and  $\beta$ -catenin pathways in macrophages [70]. Additionally, oxidized lipids, IL-6 and TNF- $\alpha$  (pro-inflammatory cytokines), and mechanical stimuli contribute to both increased inflammation and subsequent ectopic calcification [71]. Pro-inflammatory macrophages secrete elastolytic cathepsins and collagen-degrading MMPs (e.g., MMP-2 and -9), and the resultant proteolytic ECM degradation and remodeling causes atherosclerotic plaque instability and rupture, the leading cause of cardiovascular morbidity[72, 73]. Inflammation precedes and may serve as a requisite step for the onset of both atherosclerotic and aortic valve calcification [73]. Monocytes internalize forming minerals and secrete more inflammatory cytokines and intensify pathologic condition [74].

Cytokines secreted by pro-inflammatory macrophages exacerbate calcification by activating apoptosis or osteogenic pathways activation in SMCs and VICs [11]. In addition to an indirect role in pro-calcific remodeling, macrophages can directly contribute to cardiovascular calcification through release of calcifying EVs in hyperphosphatemic milieu [11]. Macrophage-derived calcifying EVs contain the tetraspanin exosomal markers of CD9, CD63, CD81 and TSG101 [47, 75]. These EVs also share similarities with chondrocyte-derived MVs, including immuno-positivity for CD68 [75]. In EVs released by macrophages, calcium mineral nucleates on complexes containing S100A9 (a pro-inflammatory and pro-thrombotic factor[37]), PS, and annexin V on the EV membrane [32]. Accumulation and aggregation of these EVs results in mineral growth within atherosclerotic plaques. Of note, macrophages contribute to both vascular and valvular calcification; therefore, macrophage-derived EV calcification could provide a link between mineral depositions within these tissues.

## **2.8. Summary**

Calcifying EVs play an important role in the initiation and development of cardiovascular calcification. Though calcifying EVs in cardiovascular tissues appear to share commonalities with MVs, they could be derived from different origins within the cell, and may arise from exosomal pathways [64]. The overlapping characteristics between these vesicles underscore the fact that research in cardiovascular calcification has been informed by pioneering research in bone physiology. However, the noted differences between cardiovascular calcifying EVs and bone MVs warrant further investigation. The appearance of calcific mineral in cardiovascular tissues associates strongly with a decrease in bone mineral density—a phenomenon known as the calcification paradox [10]. Further, the type and quality of mineral that forms appear different in the two tissues [4]. Studies into the differences between the fundamental building blocks of calcification—calcifying EVs in cardiovascular tissues and MVs in bone—may provide new

insight into the observed divergence in mineral within these tissues and present therapeutic options that avoid unwanted off-target effects.

## Chapter III: Aim 1 – Time-dependent Role of Bisphosphonates in Cardiovascular Calcification

### 3.1. Introduction

Atherosclerosis represents the most common cause of cardiovascular disease [5, 76] and begins with low-density lipoprotein (LDL) accumulation in the intima [77]. Oxidized LDLs elicit an immune response in which stimulate vascular smooth muscle cells (VSMCs) [78] and endothelial cells to express adhesive molecules [77]. In turn, the presence of adhesive molecules mediates monocyte migration into the plaque and differentiation to macrophages and dendritic cells. These cells engulf the lipoproteins and become foam cells. Continuous lipoprotein accumulation leads to necrotic core formation [77]. VSMCs migrate to the lipid pool and proliferate, which along with constant LDL accumulation and inflammatory responses, thickens the intima. Excessive extracellular matrix (ECM) protein production, including collagen, elastin, and proteoglycans, forms the fibrous cap in the lesion. Vascular smooth muscle cells migration and osteogenic differentiation promote calcification within the atherosclerotic plaque [77]. Plaque calcification occurs in 53 and 32% of American male and female atherosclerotic patients, respectively [79]. Comprehensive analyses of coronary artery calcium have demonstrated a strong positive correlation between calcification and all-cause mortality, including cardiovascular and coronary disease [80]. Though overall calcium score positively predicts cardiovascular morbidity, local effects of calcification on plaque stability is determined by calcification size and morphology.

Recent clinical studies reported percent calcified plaque volume as a key factor for plaque stability [81]. Plaques with high percentages of calcification were more stable and less likely to rupture. Plaque vulnerability classically associates with low collagen content in the fibrous cap, which compromises its tensile strength [82]. *In silico* studies highlight the presence of destabilizing microcalcifications (5-15  $\mu\text{m}$ )—undetectable due to resolution limits of the traditional clinical imaging modalities—in the cap of the vulnerable plaques as a determinant of their biomechanical failure [59,83]. Large macrocalcification (> 50  $\mu\text{m}$ ) stabilizes the plaque through tissue stress factor

reduction. However, microcalcifications destabilize the plaque by creating stress foci within the fibrous cap due to large mismatch in material properties between the stiff minerals and the surrounding hyperelastic extracellular matrix [59, 67, 83-85]. Prospective clinical data from the Multi-Ethnic Study of Atherosclerosis (MESA) cohort corroborates the biomechanical model predictions linking microcalcification with plaque rupture [85]. These data suggest that coronary artery calcification volume directly contributes with higher risk of coronary heart disease and cardiovascular events. Interestingly, calcium density inversely correlates with cardiovascular event risk [85].

Patients with bone disorders are also at high-risk for cardiovascular events [17, 86]. Unbalanced bone turnover (either high or low bone formation rate) alters the serum calcium and phosphate levels and increases the risk of vascular calcification [87]. Bisphosphonates (BiPs), the most common osteoporotic treatment option, stabilize bone mineral through their high binding affinity to hydroxyapatite and decrease bone resorption by suppressing osteoclast activity [86]. BiPs act as non-hydrolyzable analogs of inorganic pyrophosphate (PPi), a common calcification inhibitor of ectopic calcification [2, 86, 88]. However, BiPs have demonstrated potential off-target effects on cardiovascular morbidity. BiP usage correlates with higher risk of cardiovascular/cerebrovascular events and arterial fibrillation in osteoporotic patients with a history of previous cardiovascular events [89, 90]. Retrospective clinical trials found paradoxical cardiovascular outcomes in patients taking BiPs. In women with chronic kidney disease, BiPs moderately reduced the hazard ratio of future cardiovascular events in patients with no previous cardiovascular events; yet, in patients with prior cardiovascular events, BiPs increased the hazard ratio of future events [9].

BiPs may affect vascular calcification through both direct alterations to plaque mineral and systemic effects on calcification mediators. Previous studies reported accumulation of BiPs in the arterial wall of both an atherosclerotic rabbit model and human plaques [91, 92]. Short-term BiP treatment elevated serum levels of parathyroid hormone and osteocalcin, key regulators of cardiovascular calcification [93, 94], in a female renal failure rat model [95]. BiPs prevented medial

calcinosis in a male renal failure rat model; however, it was parallel to reduction in bone mass density [96]. BiPs altered the mineral microstructure in Apolipoprotein E-deficient (*Apoe*<sup>-/-</sup>) mice fed an atherogenic diet, indicating a direct interaction between BiPs and mineral within the plaque [76]. Given the long term administration of BiPs for osteoporosis treatment [97], further studies are needed to assess how BiPs affect vascular calcification over the course of plaque development.

Here, we investigated the effect of BiP treatment on atherosclerotic plaque calcification when given at early, intermediate, and late stages of atherosclerosis. We began BiP administration to Apolipoprotein E-deficient (*Apoe*<sup>-/-</sup>) mice at three different periods of plaque development based on previous reports [5, 57, 98]: before mineral formation (early), during plaque remodeling and mineral deposition (mid-term), or after the formation of mature, calcified plaques (late stage). Our data indicate that beginning BiP treatments in either early or late stages promote plaque calcification; however, early BiP treatment resulted in narrower mineral size distribution compared to the late-stage treatment. Interestingly, beginning the BiP treatment during active plaque remodeling led to lower levels of plaque calcification compared to the other treatment groups. These data may provide insight into potential cardiovascular-related off-target effects of BiPs.

### **3.2. Methods**

#### ***In vivo Study***

The animal study was approved by the Institutional Animal Care and Use Committee (IACUC) at Florida International University under protocol 17-022 and conformed to current NIH guidelines. Eight-week-old mice homozygous genotype for the *Apoe*<sup>tm1Unc</sup> mutation (B6.129P2-*Apoe*<sup>tm1Unc</sup>/J, *ApoE*<sup>-/-</sup>, n = 40, 20 per biological sex) were purchased from the Jackson Laboratory (Bar Harbor, Maine, USA). After two weeks of incubation and feeding with a regular chow diet, the animals (10 weeks old) were fed with an atherogenic diet (ENVIGO, TD.88137 adjusted calories diet 42% from fat) for 25 weeks. Mice were split into four groups (5 males and females per treatment): Week 5,

Week 10, and Week 15, in which animals received subcutaneous injections of bisphosphonate ibandronate sodium (2 mg/kg/mouse, APEXBIO, B1772) twice per week, following 5, 10, and 15 weeks of the atherogenic diet, respectively. The control group received drug vehicle, phosphate-buffered saline (PBS, 1X, Caisson Labs, PBL01). For the injections, animals were partially anesthetized using isoflurane (1%, Patterson Veterinary, 07-893-1389, in 2 L.min<sup>-1</sup> oxygen flow). At the study end point (after 25 weeks of diet), the mice received a tail vein injection of a calcium tracer, OsteoSense 680EX (80 nmol/kg/mouse, PerkinElmer, NEV10020EX). After 48 hours, the animals were anesthetized with isoflurane (1%, in 2 L.min<sup>-1</sup> oxygen flow) followed by retro-orbital bleeding for blood collection. Mice were then immediately euthanized by laceration of the diaphragm before tissue collection. The hearts and aortas were resected and fixed in formalin (10% w/v, Fisher Scientific, SF100) for 2 hours. The blood samples were centrifuged at 2,000×g for 15 minutes to isolate the serum.

### ***Calcification Morphological Quantification***

After resection, the aortas were imaged using a near-infrared scanner (LI-COR Odyssey) to visualize the atherosclerotic plaque calcification burden. The signals were localized and quantified using edge detection algorithms in a custom MATLAB script, which quantified the total area of the calcium tracer, and normalized to the total scanned aorta area. The resected aortic roots were embedded using Tissue-Plus OCT (Fisher Scientific, 23-730-571) and cryosectioned (18 μm/section). The sections were imaged using a confocal microscopy system (Eclipse Ti, Nikon). To assess total, mean, and maximum calcification area, a custom image analysis script was developed in MATLAB. After filtering the background and smoothing the images, individual microcalcifications were identified as connected pixels in binarized images. The script reported the summation of the pixels, average area of the connected pixels, and the maximum connected area for each image as total, mean, and maximum calcification area, respectively. Connected areas smaller than 5 pixels were excluded from analyzed data.

### ***Serum Alkaline Phosphatase Activity and Total Cholesterol Assessment***

To assess the activity of mouse serum tissue non-specific alkaline phosphatase (TNAP), a colorimetric assay kit (BioVision, K412) was used. The samples were diluted 1:20 in assay buffer, and 80  $\mu$ L of each sample were mixed with 50  $\mu$ L of 5 mM pNPP solution and incubated for 60 min at 25°C. The colorimetric change resulting from the reaction was detected using a multi-mode reader (BioTek, Synergy HTX) to measure absorbance at 405 nm.

To quantify the serum total cholesterol, a Wako Free Cholesterol E kit (FUJIFILM Medical Systems USA, 99902601) was used. Briefly, 10  $\mu$ L of each serum sample were resuspended in 1 mL of assay color reagent and incubated at 37°C for 5 min. The colorimetric change resulting from the reaction was detected using a plate reader to measure absorbance at 600 nm.

### ***X-ray Computed Tomography (X-ray CT)***

Femurs were dissected from mice, wrapped in parafilm and imaged directly in a Nikon XT H 225 scanner (macro-CT, Nikon Metrology, Tring, UK). The raw transmission images were reconstructed using commercial image reconstruction software package (CT Pro 3D, Nikon Metrology, Tring, UK), which employs a filtered back-projection algorithm. The scan was performed using 80 kV beam energy, 70  $\mu$ A beam current, and a power of 5.6 W. A PerkinElmer 1620 flat panel detector was used, with 200  $\mu$ m pixel size. The resulting effective pixel size was 5  $\mu$ m. The exposure time per projection was 0.5 s, and a total of 1601 projections were acquired, resulting in a scanning time of approximately 13 minutes per sample. Bone structural parameters, including thickness and volume fraction (the ratio of bone volume (BV) to total volume (TV)), for both cortical and trabecular regions were assessed using a plug-in module, BoneJ [99], in ImageJ (NIH, USA) [100].

## *Statistics*

Data are presented as the mean of independent replications, and error bars represent the standard error of the mean. The reported n values represent independent biological replicates. Statistical significance between groups was calculated using two-way ANOVA with mixed-effects model in GraphPad Prism 8. A p-value less than 0.05 was considered statistically significant. In the case of comparisons between two groups, the statistical significance was calculated using Welch's t-test with p-values less than 0.05 significant.

## **3.3. Results**

### *BiP treatment increases the atherosclerotic plaque calcification in a mouse model*

Visualization and quantification of the calcium tracer OsteoSense from resected aorta revealed significantly elevated plaque calcification in all BiP-treated animals compared to the control group (**Fig. 2, A**), regardless of BiP regimen beginning time and sex. In male mice, early (week 5) and late (week 15) BiP treatments showed the highest plaque calcification compared to control and mid-term BiP administration (week 10), as shown in **Fig. 2, B**. However, female mice exhibited no significant difference across the BiP treated groups in terms of plaque calcification burden along the aorta (**Fig. 2, C**). Interestingly, female mice showed significantly higher levels of calcification compared to males when the BiP treatment began at 10 weeks of the atherogenic diet. The level of calcification remained similar between males and females in control, week 5, and week 15 groups (**Fig. 2, D to G**). These data demonstrate that BiP may interact with the ectopic atherosclerotic plaque calcification and increase the rate of mineral formation.

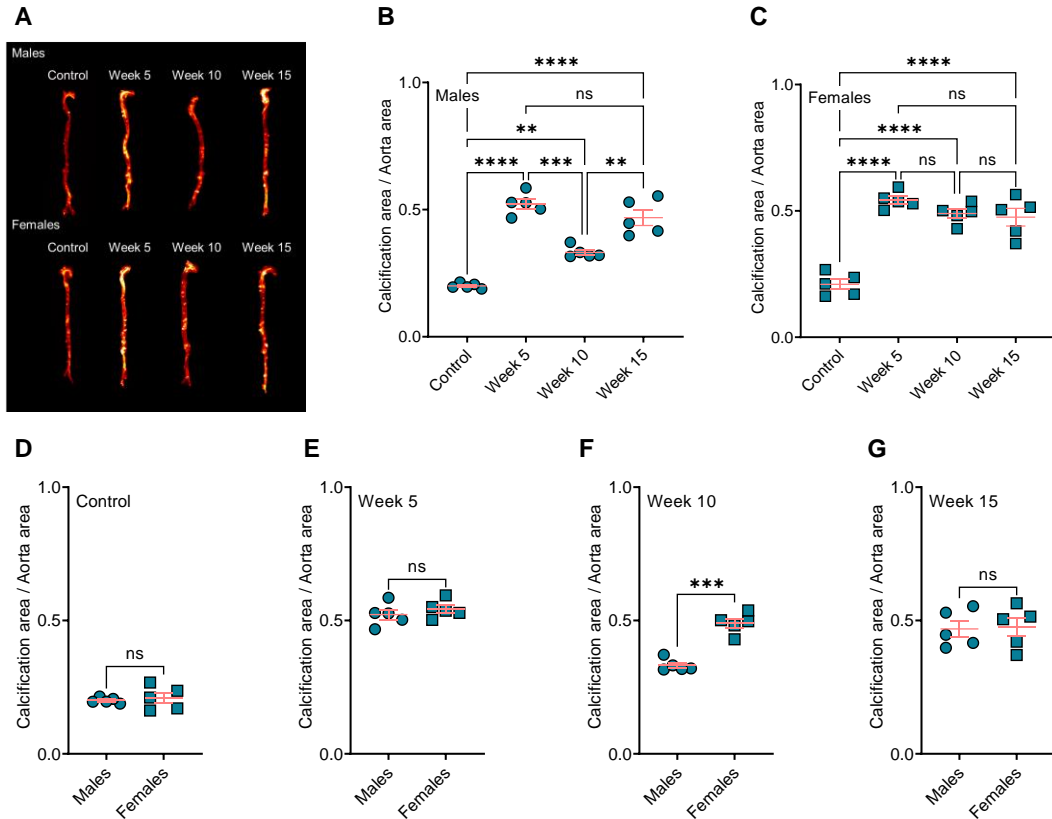


Figure 2. BiP treatment increases the plaque calcification in *Apoe*<sup>-/-</sup> mice. (A) visualization of the calcium burden using a near-infrared calcium tracer, OsteoSense; (B and C) quantification of OsteoSense signal and correlation to total calcification in male and female mice, respectively; (D to G) comparison of total calcification between male and female mice in each group. \* $P < 0.05$ , \*\* $P \leq 0.01$ , \*\*\* $P \leq 0.001$ , and \*\*\*\* $P \leq 0.0001$ , two-way ANOVA with Tukey's post-hoc test for comparison between multiple groups, and Welch's t-test for comparison between two groups.

### ***BiP treatment alters the size of mineral in the atherosclerotic plaque***

Analysis of the mineral morphologies in the aortic roots of the mice showed BiP treatment significantly increased the total calcification area in both male and female groups, compared to the control mice (**Fig. 3, A, B, E, and F**). Similar to the plaque calcification along the aorta, both week 5 and week 15 male groups had a significantly higher level of total calcification area, compared to the week 10 group (**Fig. 3, B**). However, no significant changes were observed between the female BiP-treated groups. The average calcification size was significantly bigger in early BiP-treated group (week 5) compared to the control, week 10, and week 15 groups. The mean calcification area

showed no significant differences between the male control, week 10, and week 15 groups (**Fig. 3, C**). In female mice, the mean calcification area increased in both week 5 and week 15, compared to the control and week 10 groups. No significant changes were observed between the control and week 10 groups (**Fig. 3, G**). Maximum calcification area, the largest mineral detected in a plaque, increased in all BiP-treated groups compared to the control, regardless of sex. The largest calcified area in the male groups was detected in both week 5 and week 15. In female groups, early BiP treatment increased the maximum mineral size in the plaque compared to other time points, with no significant differences between week 10 and 15 (**Fig. 3, H**).

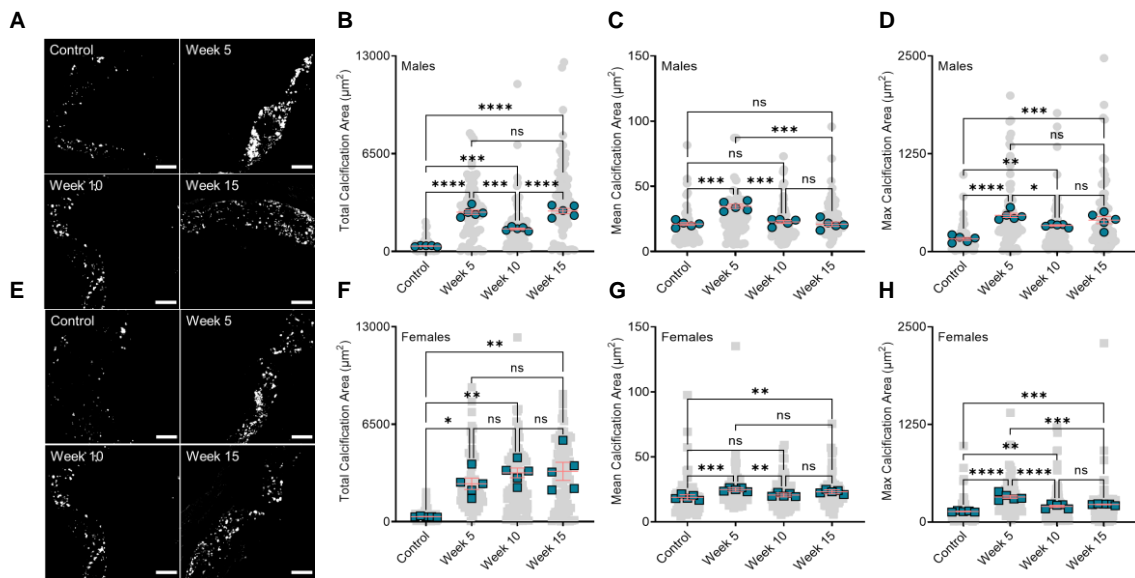


Figure 3. BiP treatment alters the micromorphology of the minerals in the plaque. (A) visualization of the minerals in the atherosclerotic plaques of male mice (20X, scale bar 100 μm); (B) total plaque calcification in male mice; (C) mean calcification area (mean of mineral size) in male animals; (D) maximum calcification area in male mice; (E) visualization of the minerals in the atherosclerotic plaques of male mice (20X, scale bar 100 μm); (F) total plaque calcification in female mice; (G) mean calcification area (mean of mineral size) in female animals; (H) maximum calcification area in female mice. \*P < 0.05, \*\*P ≤ 0.01, \*\*\*P ≤ 0.001, and \*\*\*\*P ≤ 0.0001, two-way ANOVA with Tukey's post-hoc test.

Comparing male and female mice, we observed no significant differences in total calcification area in the control, week 5, and week 15 treatment groups. However, BiP treatment beginning at 10 weeks of diet significantly increased the total calcification area in the female mice compared to the male mice (**Fig. 4**, panel **A**). The mean calcification area (mineral average size) remained unchanged between the males and females in the control, week 10, and week 15; however, in week 5, the male mice showed a significantly elevated mean calcification area compared to the females (**Fig. 4**, panel **B**). Regardless of the time at which BiP treatment began, the maximum calcification area in the male groups was higher than the females; however, no significant differences were detected in the control group between males and females (**Fig. 4**, panel **C**). These data suggest that BiP treatment may interact with and alter the morphology of mineral in the plaque.

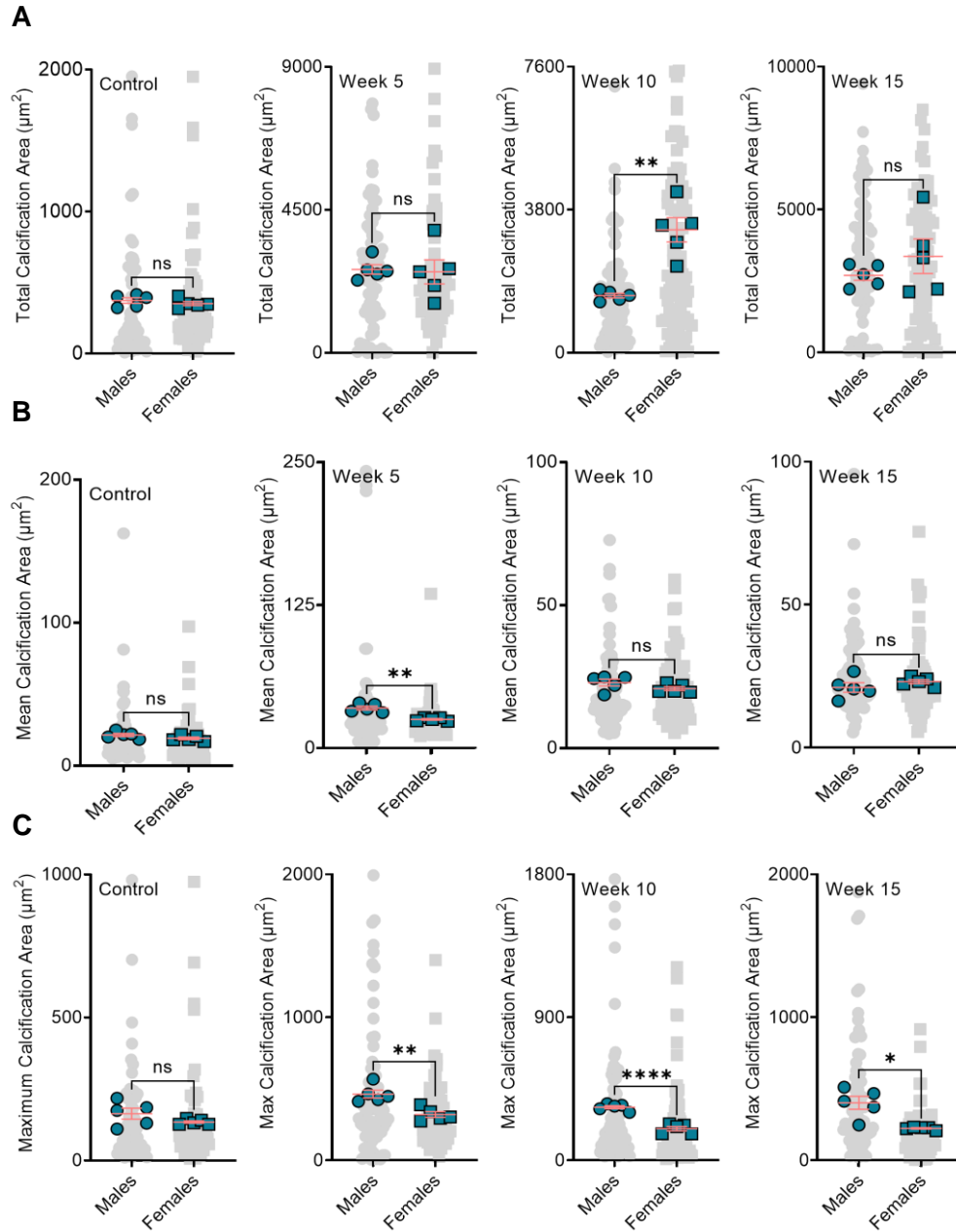


Figure 4. BiP treatment affects the mineral morphology differently in males and females. Panel (A) comparison of total plaque calcification between male and female mice; Panel (B) comparison of mean calcification area between male and female mice; Panel (C) comparison of maximum calcification area between male and female mice. \* $P < 0.05$ , \*\* $P \leq 0.01$ , \*\*\* $P \leq 0.001$ , and \*\*\*\* $P \leq 0.0001$ , Welch's t-test.

***BiP treatment does not affect serum alkaline phosphatase nor cholesterol***

We measured the level of alkaline phosphatase, an enzyme required for calcification, in the serum collected at the study endpoint. We observed no significant differences between the BiP-treated and the control groups across either sex (**Fig. 5, A and B**). Furthermore, the total serum cholesterol remained unchanged across BiP-treated groups compared to the controls for both male and female mice (**Fig. 5, C and D**).

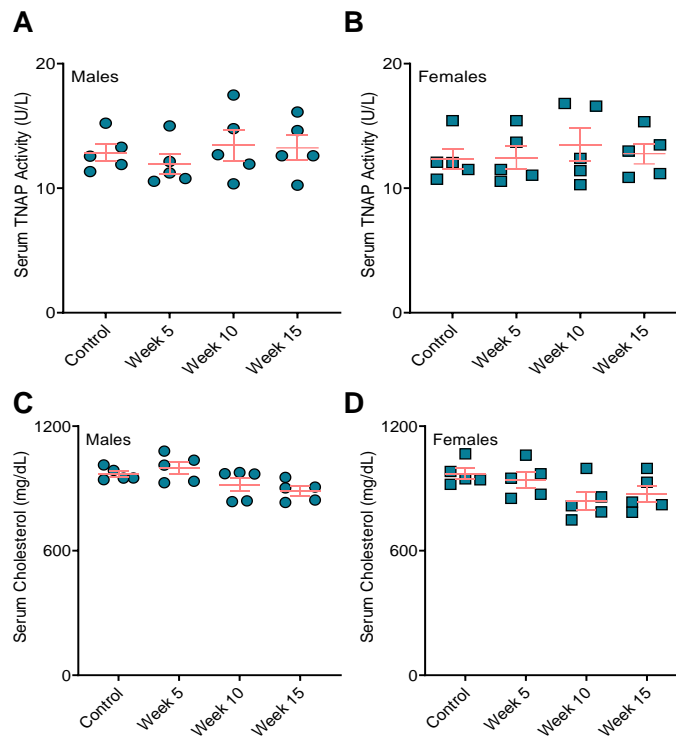


Figure 5. BiP treatment does not affect the serum TNAP activity and total cholesterol. Serum TNAP activity in (A) male mice and (B) female mice; serum total cholesterol in (C) male mice and (D) female mice. No statistically significance observed across the groups, two-way ANOVA with Tukey's post-hoc test.

***Bone remodeling correlates positively with the BiP treatment duration***

Analyses of the resected bones showed dramatic increased bone volume in BiP-treated mice compared to the control group. The longer treatment with BiP (i.e., beginning the BiP treatment at the early time point) results in a higher bone volume in both cortical and trabecular areas (metaphyseal and epiphyseal regions), as shown in **Fig. 6**, panel **A** and **B**. The cortical bone thickness followed a similar trend and exhibited a positive correlation with the duration of BiP treatment. The thickness of the trabecular bone, both metaphyseal and epiphyseal regions, was significantly increased in the longest BiP-treated group (beginning of BiP regimen after 5 weeks of diet); this parameter remained unchanged for week 10 and week 15 groups compared to the control mice. **Table 1** summarizes the bone microstructure parameters analyzed for each group.

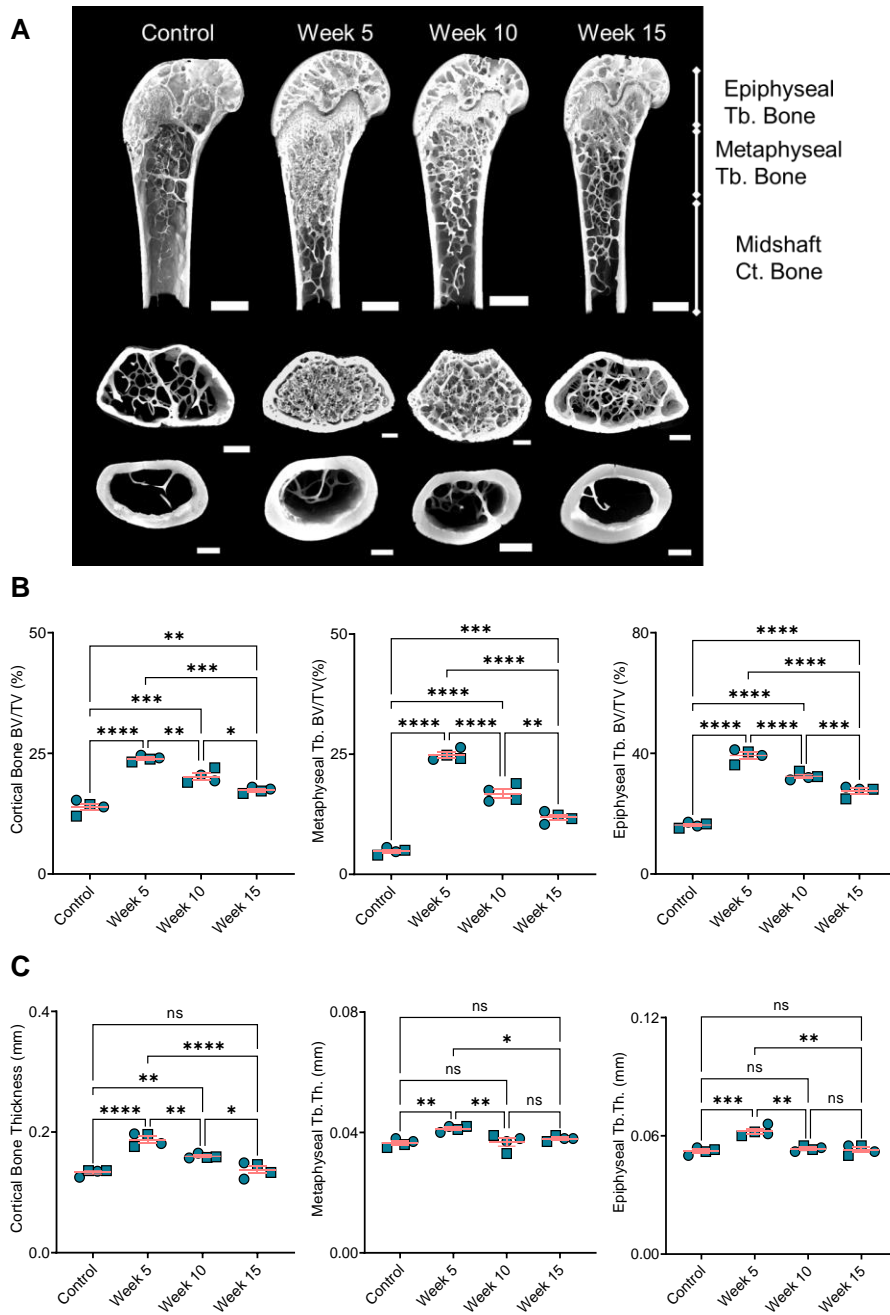


Figure 6. Bone remodeling positively correlates with duration of BiP treatment. (A) reconstruction of femoral bone microstructure for the different treated and untreated groups; Panel (B) bone volume fraction (bone volume/total volume) for cortical and trabecular regions; Panel (C) bone thickness for cortical and trabecular regions. \* $P < 0.05$ , \*\* $P \leq 0.01$ , \*\*\* $P \leq 0.001$ , and \*\*\*\* $P \leq 0.0001$ , two-way ANOVA with Tukey's post-hoc test.

Table 1. Bone structural parameters for BiP-treated and control groups.

<b>Parameter</b>	<b>Control N = 4</b>	<b>Week 5 N = 4</b>	<b>Week 10 N = 4</b>	<b>Week 15 N = 4</b>
<b>Distal femur</b>				
<i>Epiphyseal Trabecular Bone</i>				
BV/TV (%)	16.22±0.37	39.3±0.96	32.4±0.5	27.48±0.76
Tb.N (mm <sup>-1</sup> )	7.63±1.11	12.86±0.11	12.82±0.32	12.05±0.34
Tb.Th (mm)	0.052±0.001	0.062±0.001	0.053±0.001	0.053±0.001
Tb.Sp (mm)	0.59±0.06	0.41±0.02	0.42±0.02	0.43±0.02
BS/BV (mm <sup>2</sup> /mm <sup>3</sup> )	0.065±0.002	0.059±0.003	0.057±0.003	0.062±0.003
EF	0.017±0.003	0.033±0.005	0.034±0.009	0.016±0.003
EF <sub>max</sub>	0.885±0.004	0.902±0.005	0.887±0.004	0.88±0.009
EF <sub>min</sub>	-0.82±0.003	-0.825±0.008	-0.812±0.007	-0.81±0.009
DA	1.43±0.05	1.39±0.04	1.42±0.03	1.4±0.07
<i>Metaphyseal Trabecular Bone</i>				
BV/TV (%)	4.82±0.29	24.8±0.5	16.8±0.75	11.86±0.5
Tb.N (mm <sup>-1</sup> )	4.1±0.3	13.1±0.09	11.02±0.07	7.62±0.49
Tb.Th (mm)	0.036±0.001	0.041±0.001	0.037±0.001	0.038±0.001
Tb.Sp (mm)	0.56±0.094	0.29±0.04	0.27±0.015	0.44±0.022
BS/BV (mm <sup>2</sup> /mm <sup>3</sup> )	0.092±0.003	0.085±0.001	0.092±0.003	0.092±0.01
EF	0.12±0.02	0.07±0.005	0.086±0.017	0.07±0.03
EF <sub>max</sub>	0.835±0.019	0.87±0.002	0.86±0.012	0.855±0.03
EF <sub>min</sub>	-0.67±0.036	-0.765±0.013	-0.71±0.022	-0.73±0.052
DA	1.77±0.14	1.6±0.15	1.522±0.09	1.78±0.09
<b>Femoral midshaft</b>				
<i>Cortical Bone</i>				
Mean Ct.Th (mm)	0.133±0.002	0.187±0.004	0.159±0.001	0.137±0.005
BV/TV (%)	13.9±0.48	23.9±0.25	20.2±0.6	17.3±0.24
Ps.Pm (mm)	5.65±0.11	5.37±0.2	5.35±0.22	5.33±0.18
Ec.Pm (mm)	4.75±0.11	4.2±0.18	4.15±0.2	4.17±0.21
J (mm <sup>4</sup> )	0.49±0.03	0.455±0.04	0.417±0.007	0.5±0.1

Data were collected using X-ray Computed Tomography of distal femur and femoral midshaft. Values represent the mean±SEM.

BV/TV= Bone Volume/Total Volume; Tb.N= Trabecular Number; Tb.Th= Trabecular Thickness; Tb.Sp= Trabecular Separation; BS/BV= Specific Bone Surface: Bone Surface Area/Bone Volume; EF= Ellipsoidal Factor; DA= Degree of Anisotropy; Ct.Th= Cortical Thickness; Ps.Pm= Periosteal Perimeter; Ec.Pm= Endocortical Perimeter; J= Polar Moment of Inertia.

### 3.4. Discussion

Atherosclerotic plaque calcification in *Apoe*<sup>-/-</sup> mice fed a chow diet begins around 45-60 weeks of age [101]; however, feeding the mice an atherogenic diet (21% fat and 15% cholesterol) accelerates plaque calcification dramatically following 10-12 weeks of the diet [98, 102]. *Apoe*<sup>-/-</sup> mice fed an atherogenic diet develop early plaque, including lipoproteins accumulation, immune system activation, and formation of cholesterol-rich foam cells between 4 to 14 weeks of feeding. Lipid cores develop following 14 to 16 weeks of the diet, and fibrous cap formation and mature plaque development occur over 18 to 20 weeks of the diet [103]. Here, we studied the role of BiP treatment on atherosclerotic plaque calcification in *Apoe*<sup>-/-</sup> mice. The animals received BiP treatment twice per week at three different time points: after 5 weeks of the diet, when the plaque formation has started but prior to calcification formation; after 10 weeks of diet, at the onset of plaque calcification; and after 15 weeks of diet, when the plaque is developed and contains calcified regions.

We showed that the total calcification burden was increased by both the early (week 5) and late (week 15) BiP treatment regimens in male mice compared to the control group. The early BiP treatment led to a higher mean calcification area (bigger mineral size average) compared to the late one, which may stabilize the plaque by reducing the rupture risk. Given the fact that maximum calcification area was comparable between early and late BiP treatment groups, a smaller mineral size average in the week 15 group means the presence of a wider range of mineral size distribution, which may influence the plaque stability. In terms of mid-term BiP treatment (week 10), smaller average and maximum mineral size were observed compared to other BiP treated male mice. In the female mice, even though the total calcification remained unchanged across the BiP-treated groups, the early treatment showed higher average and maximum mineral size compared to the mid-term group. The average size of the early and late treated group was similar, with reduction in maximum mineral size for the late BiP-treated group, which indicates a narrower distribution of the mineral

size, which may contribute in plaque stability. It should be mentioned that mouse plaques do not rupture, which limited us to perform biomechanical analyses in this study. However, our data suggest that timing of BiP intervention in relation to ongoing atherosclerotic remodeling could influence mineral morphology and thus plaque stability. Previous studies using electron microscopy revealed that timing of BiP regimen affects the morphology and topography of the mineral aggregates (less than  $5 \mu\text{m}^2$ ) of the plaque microcalcifications [76]; longer BiP treatment led to bigger individual mineral aggregates with higher surface roughness, while later time points reduced both mineral aggregates size and surface roughness [76]. Furthermore, mineral aggregates associated with later BiP treatment beginning showed qualitatively disorganized and loose morphologies [76]. Along with these outcomes, our data support the fact that BiP potentially alters the morphology of the microcalcifications, which may play role in plaque stability.

We showed that early and late BiP treatment initiations affected the total calcification area similarly in male and female mice. However, for mid-term BiP regimen, during plaque remodeling and mineral deposition onset, total calcification area was higher in female mice compared to males. Interestingly, the mean calcification area (average of the mineral size) was similar across males and females in this group; yet, male mice showed bigger maximum calcification area compared to the females, which suggest a wider mineral size distribution in males. These results may indicate a critical timing in respect of BiP usage. Recent clinical studies indicate a negative correlation between the cumulative BiP dosage (an indication of portion of day covered) to hazard ratio of hospitalization due to atherosclerotic cardiovascular events [104]. Interestingly, in intermediate group, female patients indicated higher hazard ratio (0.958) compared to associated male patients (0.897) [104]. Furthermore, these clinical outcomes support our data that the longer BiP usage duration may lead to bigger minerals, but narrow size distribution, which *in silico* studies suggest as stable plaque with lower rupture risk [59, 105].

In humans, 95% of the serum TNAP originate from bone and liver [106], and unbalanced bone turnover, aging, and chronic kidney disease correlate with abnormal elevated serum TNAP [107,

108]. Postmenopausal women showed no increase in serum TNAP, however, it increased in osteoporotic postmenopausal women [107]. BiPs lowered serum TNAP in osteoporotic postmenopausal women and men with heterotopic ossification [107, 109, 110]. Yet, our results showed unchanged TNAP in serum across the treated and untreated groups. Thus, elevated plaque calcification in all treated groups appears to be independent of systemic TNAP changes.

Clinical trials reported serum LDL reduction in osteoporotic females treated with BiPs; however, the level of high density lipoprotein and lactate dehydrogenase remained unchanged [111-113]. Of note, we showed total cholesterol remained unchanged in all animals, regardless of the BiP treatment. This may originate from the fact that these animals (*Apoe<sup>-/-</sup>*) are deficient in cholesterol clearance and continuous feeding with an atherogenic diet maintains hypercholesterolemia. Thus, our data indicate that BiP treatment did not affect the total cholesterol level, which may demonstrate that BiP treatment does not affect the lipid metabolism and plaque progression in *Apoe<sup>-/-</sup>* mice.

The outcomes from bone microstructure analyses demonstrate the substantial effect of BiP treatment on bone remodeling. These results reveal a time-dependency of BiP regimen with the final bone volume and thickness in cortical and trabecular areas. Of note, we showed a positive correlation between bone remodeling and increased plaque calcification for early BiP treatment in *Apoe<sup>-/-</sup>* mice. Long term BiP treatment led to increased mineralization in both bone and atherosclerotic plaque. However, for later time points, beginning BiP treatment after 10 and 15 weeks of diet, the data demonstrate a negative correlation between bone remodeling and plaque calcification. Both cortical and trabecular bone volumes are significantly higher in the week 10 group, compared to week 15, while plaque calcification for the latter is significantly higher compared to former. Previous studies reported that BiP may imitate the effects of pyrophosphate, a mineralization inhibitor in the cardiovascular system; however, our data did not support the inhibitory role of BiP to reduce cardiovascular calcification to non-treated controls. Importantly, the choice of animal models or patients in clinical trials may affect the BiP outcomes; atherosclerotic plaque calcification represents a complex process in which several cell types,

including VSMCs and macrophages [114, 115], are involved, thus, the BiP treatment may affect multiple aspects of plaque progression and calcification.

### **3.5. Summary**

Atherosclerotic plaque calcification represents a significant predictor of lesion vulnerability. Patients with bone disorders are prone to develop ectopic cardiovascular calcification. Clinical trials correlated BiPs, a common osteoporotic pharmaceutical family, with contradicting cardiovascular outcomes. Here, we demonstrated the importance of treatment timing in BiP-induced mineral disruption or promotion. We indicated that BiP can alter key morphological features of the microcalcifications within the atherosclerotic plaque of *Apoe*<sup>-/-</sup> mice, which may determine the risk of plaque rupture. Early beginning of BiP regimen, i.e., before calcification initiates, increased the total calcification in both males and females, however, it led to narrower mineral size distribution. Later regimen timings, either after mineralization starts or when the plaque is developed, result in wider mineral size distribution, which correlates with plaque destabilization and a higher risk of rupture. Interestingly, early BiP regimen elevated mineralization in both bone and atherosclerotic plaque. However, BiP regimen correlates negatively with bone mineralization and plaque calcification if given after the onset of plaque mineralization.

## **Chapter IV: Aim 2 – Mechanistic Study on Calcifying Extracellular Vesicle Biogenesis**

### **4.1. Introduction**

Previous studies revealed that calcification of mesenchymal stem cells requires actin-based contractility induced by dexamethasone in commonly used osteogenic culture [116, 117], but the associated mechanisms linking contraction to mineral formation remain unclear. Cell contraction activates Src tyrosine kinase (STK), a component of the focal adhesion complex, which mediates epidermal growth factor receptor (EGFR) and caveolin-1 protein (CAV1) phosphorylation [118]. CAV1 plays a key role in biogenesis of calcifying EVs, by mediating endocytosis of the caveolar domains ( $\Omega$ -like invaginations on the plasma membrane [119]) [1]. CAV1 knockdown led to significant reduction of TNAP activity and consequently, in vitro calcification of vascular smooth muscle cells [1]. STK and EGFR also share many downstream signal transduction mediators [120]. EGFR (HER1) exists within the larger ErbB family of tyrosine kinase receptors with three other members: HER2, HER3, and HER4. Except for HER2, ErbB family members bind extracellular ligands with the epidermal growth factor (EGF) motif [121]. HER2 does not bind these ligands; however, it is activated by heterodimerization with EGFR. Phosphorylated residues of EGFR and HER2 function as docking sites for scaffolding proteins, including CAV1 [121, 122]. Clinical studies revealed a robust correlation between HER2 with mammographic calcifications in breast cancer [122]. Activation of HER2 depends on EGFR phosphorylation [121], which enhances the CAV1 phosphorylation efficiency [123]. STK promotes caveolar domains detachment [124], and phosphorylated CAV1 interactions with actin stress fiber forming molecules facilitates inward trafficking of these domains [125, 126].

In endothelial cells, caveolae endocytosis occurs through CAV1 interaction with F-actin cross-linking protein filamin A (FLNA). FLNA reduces CAV1 internalization with no changes in actin stress fiber formation [127, 128]. Of note, STK enhances the interaction between CAV1 and FLNA,

and mediates trafficking of caveolar domains [127]. FLNA plays role in phosphorylation of small GTPases of the Rho family, also known as RhoA/Rho kinase or ROCK, which is involved in actin stress fiber formation and cellular contractility [129]. A previous study on neural progenitor cells indicated FLNA and ROCK interactions regulate cell morphology [130]. Furthermore, elevated cellular contractility recruits ROCK to caveolar domains [131]. ROCK translocation to caveolar domains and consequent ROCK-CAV1 interactions result in ROCK-dependent force production in rat artery [132], demonstrating the interconnectivity between CAV1 and actin dynamics.

Rac1, another member of the Rho family, regulates cell locomotion by mediating actin polymerization and filament formation during the protrusion-retraction cycle. ROCK and Rac1 function in inhibitory feedback loops in cell locomotion, where ROCK reduces the activity of Rac1 and vice versa [133]. ROCK drives contraction at the trailing edge, while Rac1 facilitates the extension at the leading edge [134]. In VSMCs, angiotensin II promotes Rac1 recruitment to the caveolar domains, where it interacts with CAV1 [135]. In sum, vascular calcification occurs downstream of altered actin dynamics, the formation of calcifying EVs requires CAV1 endocytosis and trafficking, and CAV1 is functionally linked to the actin cytoskeleton and actin-altering proteins. However, the direct relation between actin dynamics, CAV1 trafficking, and calcifying EV biogenesis has not been previously reported. Here, we investigated the role(s) of actin interactors in calcification of VSMCs and osteoblasts. The outcomes of this study could yield new mechanistic insight in physiological and pathological mineralization and may help identify therapeutic targets to prevent VSMC-dependent calcification, a direct contributor to cardiovascular morbidity.

## 4.2. Methods

### *Osteogenic Stimulation and In vitro Calcification*

Primary human coronary artery vascular smooth muscle cells (VSMCs, ATCC, PCS-100-021) were cultured using vascular smooth muscle cell media and growth kit (ATCC, PCS-100-042). VSMCs (passage 4-6) were harvested using 0.05% trypsin-EDTA solution (Caisson Labs, TRL04) and seeded with a density of 26,320 cells.cm<sup>-2</sup> and incubated for 72 hours at 37°C, 5% CO<sub>2</sub> with controlled humidity prior to treatment. VSMCs were treated with either control media, consisting of DMEM (HyClone, SH30022.01), 10% v/v bovine calf serum (iron-supplemented, R&D Systems, S11950), and 1% v/v penicillin-streptomycin (Gibco, 15070-063), or with an osteogenic media (OS) optimized to induce calcification [5, 136]. OS media were supplemented with 10 mM β-glycerophosphate (Sigma, 13408-09-8), 0.1 mM L-ascorbic acid (Sigma, 113170-55-1), and 10 nM dexamethasone (Sigma, 50-02-2). To assess the role of various inhibitors, including PP2 (Src tyrosine kinase inhibitor, 4 μM, Santa Cruz Biotechnology, sc-202769), Calpain inhibitor (5 μM, Cayman Chemical Company, 14921), Y-27632 (RhoA protein kinase inhibitor, 10 μM, Santa Cruz Biotechnology, sc216067), InSolution Rac-1 inhibitor II (12.5 μM, EMD Millipore, 553512), and methyl-β-cyclodextrin (mβCD, 1 mM, Cayman Chemical Company, 21633), were added to the OS media. An equal volume of the vehicle was added to the control and OS groups for each inhibitor. We found that 28 days in OS culture media led to robust calcification by VSMCs; therefore, all cultures (n = 3, independent donors, male and female) were treated for 28 days and media were replaced every three days.

Osteoblasts (from human fetus, hFOB 1.19, ATCC, CRL-11372) were cultured and grown in DMEM containing 10% v/v bovine calf serum and 1% v/v penicillin-streptomycin. Osteoblasts (passage 4-6) were harvested using 0.25% trypsin-EDTA solution (Caisson Labs, TRL01), seeded with a density of 5,200 cell.cm<sup>-2</sup>, and incubated for 24 hours at 37°C and 5% CO<sub>2</sub> with controlled humidity. The cells were treated in three groups of control, OS, and OS supplemented with

inhibitors, including PP2 (4  $\mu$ M), Calpain inhibitor (5  $\mu$ M), Y-27632 (10  $\mu$ M), Rac-1 inhibitor (12.5  $\mu$ M), and methyl- $\beta$ -cyclodextrin (1 mM), for 21 days and media were changed every three days.

### ***Alizarin Red S Staining and Quantification***

At the end of experiments (28 and 21 days of treatment for VSMCs and osteoblasts, respectively), media were removed, and the cells were fixed using formalin (10%, Fisher Chemical, SF100) for 15 min. To visualize *in vitro* calcification, Alizarin Red S stain (ARS, Ricca, 500-32) was added to the wells and incubated for 30 min at room temperature. The stain was then removed, and the cells were washed three times with milliQ water. To quantify the *in vitro* calcification, ARS stain was extracted using acetic acid (1.67 M, Fisher Chemical, A38S) on a shaker. After 30 min, the supernatants were collected, briefly vortexed, and heated at 85°C for 10 min. The samples were then cooled on ice for 5 min and centrifuged at 20,000 $\times$ g for 15 min to remove background particles. Sample absorbance of 405 nm light was measured using a multi-mode reader (BioTek, Synergy HTX).

### ***Quantitative Real Time Polymerase Chain Reaction***

Following 14 days in control, OS, or OS plus m $\beta$ CD media, osteoblasts were lysed in 1 mL TRIzol solution (Invitrogen, 15596018). Total RNA was isolated according to the manufacturer's protocol. To perform the quantitative real time polymerase chain reaction (qRT-PCR), Power SYBR Green RNA-to-CT 1-Step Kit (Applied Biosystems, 4391178) was used. Isolated template RNA (50 ng) were added to each reaction for qRT-PCR. The results were normalized to Glyceraldehyde 3-phosphate dehydrogenase (GAPDH) expression level as the housekeeping control. The relative gene expression levels were calculated using comparative CT method, considering control groups as the reference. The following human primers were purchased from Integrated DNA Technologies (IDT); *GAPDH* Forward: CTTCGCTCTCTGCTCCTCCTGTTCG and Reverse:

ACCAGGCGCCCAATACGACCAAAT; *RUNX2* Forward: GCTCTCTAACCACAGTCTATGC  
and Reverse: AGGCTGTTTGATGCCATAGT; *ALPL* Forward:  
GGAGTATGAGAGTGACGAGAAAG and Reverse: GAAGTGGGAGTGCTTGTATCT;  
*Osteocalcin (BGLAP)* Forward: TCACACTCCTCGCCCTATT and Reverse:  
CCTCCTGCTTGGACACAAAA; *COL1A1* Forward: ACATCCCACCAATCACCT and Reverse:  
GTCATCGCACAACACCTT.

### ***Alkaline Phosphatase Activity Assay***

To assess the activity of intracellular tissue non-specific alkaline phosphatase (TNAP), a colorimetric assay kit (BioVision, K412) was used. VSMCs (n = 3) and osteoblasts (n = 3) following 14 days of treatment with control, OS, and OS plus any of the inhibitors, were lysed in 120  $\mu$ L assay buffer. Each sample (80  $\mu$ L) was mixed with 50  $\mu$ L of 5 mM pNPP solution and incubated for 60 min at 25°C. The colorimetric change resulting from the reaction was detected using a plate reader to measure absorbance at 405 nm. The results were normalized to the total protein for associated samples measured by a BCA protein assay (BioVision, K813).

### ***RNA interference***

To assess the role of CAV1 in in vitro mineralization of osteoblasts, CAV1 was knocked down in either control or OS cultures. RNA silencing was performed using 20 nM validated CAV1 siRNA (Ambion, 4390824) and On-target plus non-targeting pool (negative control, Dharmacon, D-001810-10-20). Following the culture of the osteoblasts, DharmaFECT (Dharmacon, T-2001-02) was used for CAV1 silencing. The siRNA and media were replaced every three days for 21 days.

### ***Gel Electrophoresis and Protein Immunoblotting***

VSMCs and osteoblasts were lysed in RIPA lysis and extraction buffer supplemented with protease inhibitor. After adding Laemmli SDS-sample buffer (1:4 v/v, Boston BioProducts, BP-110R) to

each lysate, the samples were denatured at 100°C for 10 min, loaded into 7.5-12% 1-mm SDS-PAGE gel (15 to 20 µg protein per lane), and run at 170 V. The proteins were then transferred to Trans-Blot turbo nitrocellulose membranes (BIO-RAD, 1704158) at 25 V for 7 min. To quantify the total protein, the membranes were stained using 2% w/v Ponceau stain (Alfa Aesar, AAJ6074409) for 20 min, followed by one wash with 5% acetic acid and milliQ water for 5 min. After imaging, the intensity of each lane was measured in ImageJ for total protein normalization. Membranes were blocked with 5% w/v bovine serum albumin (HyClone, SH30574.01) in TBS-Tween (1X) for 1 hour. The membranes were incubated with primary antibodies of interest, including CAV1 (1:200, Abcam, ab2910) and TNAP (1:200, Invitrogen, 702454) overnight at 4°C. After three washes with TBS-Tween (1X), the membranes were incubated with secondary antibody (1:1000, Li-Cor) for 1 hour, followed by three washes with TBS-Tween (1X). The protein bands were visualized with Odyssey CLx scanner (Li-Cor), and quantified using Image Studio Lite software (Li-Cor).

### ***Immunofluorescence Staining and Imaging***

VSMCs were fixed after 14 days of culture using formalin (10%) for 15 min and washed with PBS. A solution of PBS and Triton X (0.1% v/v) permeabilized the plasma membrane for 10 min at room temperature. To avoid non-specific antibody binding, the cells were incubated with a blocking buffer solution, consisting of BSA (1% w/v) and glycine (22.5 mg/mL) in PBS for 30 min at room temperature. Next, the cells were incubated for 2 hours with primary antibody against CAV1 (1:200) and washed three times with PBS. Cells were then incubated with a secondary antibody, Alexa Fluor 594 (1:500, Abcam, ab150080), for 1 hour at room temperature, followed by three washes with PBS. To visualize actin filaments, samples were incubated for 20 min with Phalloidin-iFluor 488 conjugate (1:50, Cayman Chemical, 20549) followed by three washes with PBS.

### ***In vitro Total Cholesterol Quantification***

Following 14 days in control, OS, or OS plus m $\beta$ CD media, VSMCs and osteoblasts were lysed in a lysis solution of hexane (Sigma-Aldrich, 178918) and isopropanol (Fisher Chemicals, A417-1) in a ratio of 3:2 (250  $\mu$ L/well) and centrifuged at 14,000 rpm for 10 min. The aqueous phase from each sample was extracted and dried using a vacuum chamber. The samples were then resuspended in 10  $\mu$ L isopropanol. To quantify the in vitro total cholesterol, a Wako Free Cholesterol E kit (FUJIFILM Medical Systems USA, 99902601) was used. Briefly, 10  $\mu$ L of each sample were resuspended in 1 mL of assay color reagent and incubated at 37°C for 5 min. The colorimetric change resulting from the reaction was detected using a plate reader to measure absorbance at 600 nm.

### ***Statistics***

Data are presented as the mean of independent replications, and error bars represent the standard error of the mean. The reported *n* values represent independent biological replicates. Statistical significance between groups was calculated using one-way ANOVA with Tukey's post-hoc test in GraphPad Prism 8. A p-value less than 0.05 was considered statistically significant. In case of comparison between two groups, the statistical significance was calculated using t-test with p-values less than 0.05.

## **4.3. Results**

### ***Osteoblasts mineralization is independent from caveolin-1***

We studied the role of CAV1 knockdown in mineralization of osteoblasts. Following 21 days of treatment with OS media supplemented with either siCAV1 or scrambled RNA, osteoblasts mineralized in both cultures (**Fig. 7**). Thus, we concluded that in vitro calcification of osteoblast does not depend on CAV1.

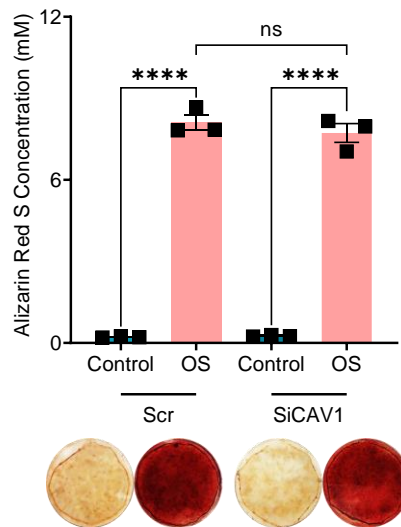


Figure 7. CAV1 silencing in osteoblasts does not prevent in vitro calcification.

***Src tyrosine kinase plays role in calcification of vascular smooth muscle cells.***

Following 14 days of treatment, intracellular CAV1 levels within VSMCs in OS culture increased significantly compared to the control group (**Fig. 8, A**). Interestingly, co-treatment with OS media and PP2 (Src tyrosine kinase inhibitor) elevated the intracellular CAV1 compared to both control and OS cultures. Intracellular TNAP levels exhibited a similar trend as CAV1; OS media significantly elevated the TNAP level compared to control group, while Src tyrosine kinase inhibitor significantly increased the intracellular TNAP compared to both control and OS conditions (**Fig. 8, B**). However, Src tyrosine kinase inhibition significantly reduced intracellular TNAP activity in OS media (**Fig. 8, C**). Along with the reduction in TNAP activity, Src tyrosine kinase completely prevented in vitro calcification of VSMCs (**Fig. 8, D**). Qualitative analysis of confocal micrographs (**Fig. 8, E**) indicated thicker stress fibers and CAV1 alignment parallel to actin filaments in VSMCs cultured under OS media compared to control group; Src tyrosine kinase reduced the density of the stress fibers and formed clusters of CAV1 in VSMCs. Interestingly, Src tyrosine kinase did not prevent in vitro mineralization of osteoblasts (**Fig. 8, F**).

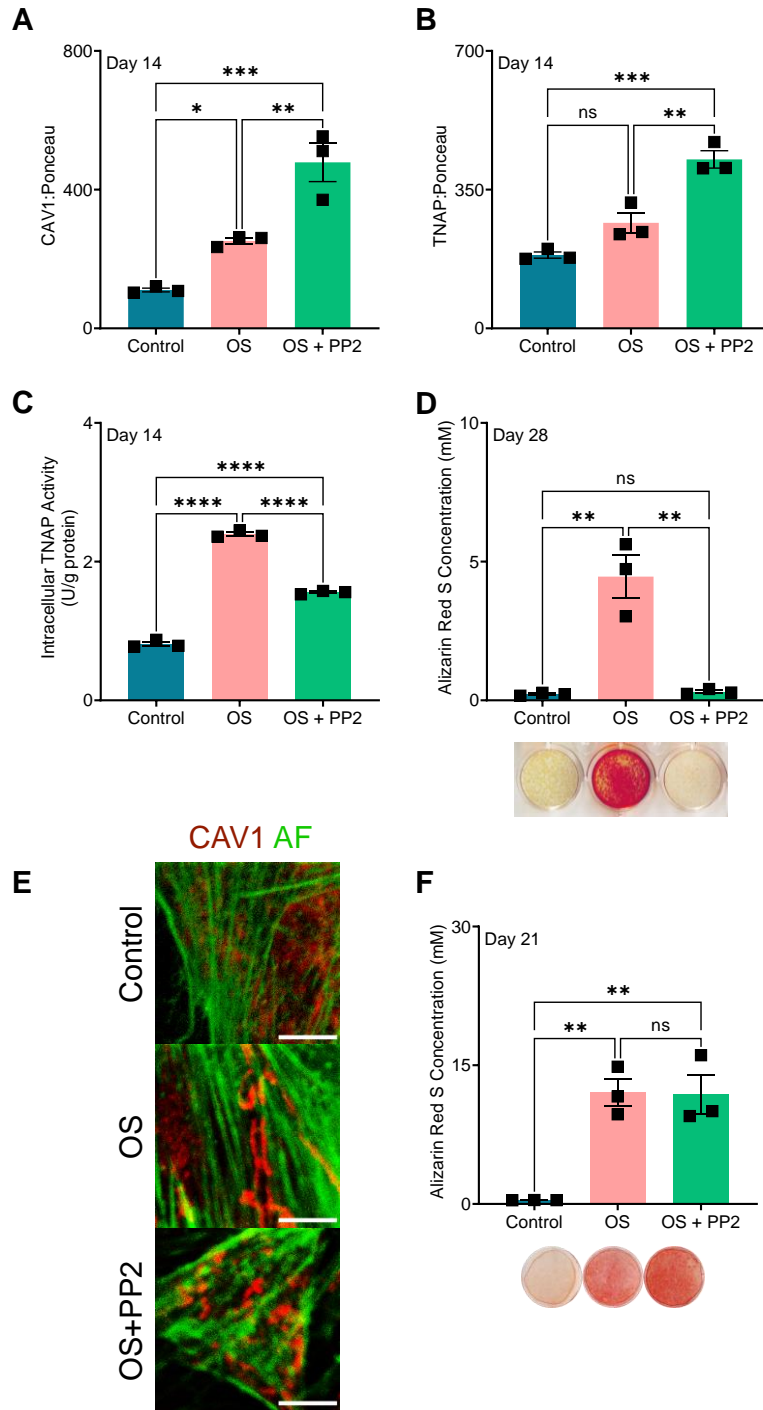


Figure 8. Src tyrosine kinase inhibitor prevents in vitro calcification of VSMCs. (A and B) Intracellular CAV1 and TNAP protein in VSMCs after 14 days of culture; (C) Intracellular TNAP activity in VSMC cultures following 14 days of treatment; (D) Alizarin red staining and quantification in VSMC cultures after 28 days; (E) Immunofluorescence staining of VSMCs after 14 days of treatment (400×, scale bar 10 μm); and (F) Alizarin red staining and quantification in osteoblasts cultures following 21 days. \*P < 0.05, \*\*P ≤ 0.01, \*\*\*P ≤ 0.001, and \*\*\*\*P ≤ 0.0001, ANOVA with Tukey's post-hoc test.

***Filamin A is involved in calcification of vascular smooth muscle cells***

Calpain inhibitor (prevents cleavage of FLNA c-terminal fragment [137]) significantly increased intracellular CAV1 and TNAP protein levels in VSMCs (**Fig. 9, A and B**). However, calpain inhibitor significantly reduced intracellular TNAP activity in OS cultures (**Fig. 9, C**). Alizarin red staining and quantification revealed that calpain inhibitor completely prevented VSMCs in vitro calcification (**Fig. 9, D**). These results suggest that FLNA cleavage is required for TNAP activation and calcification of VSMCs in OS culture. Immunofluorescence staining of the VSMCs treated with Calpain inhibitor showed clusters of CAV1 between actin filaments, compared to the CAV1 organization along filaments in OS culture (**Fig. 9, E**). Calpain inhibitor increased the in vitro mineralization of the osteoblasts, which indicates prevention of FLNA cleavage potentially promotes bone mineralization (**Fig. 9, F**).

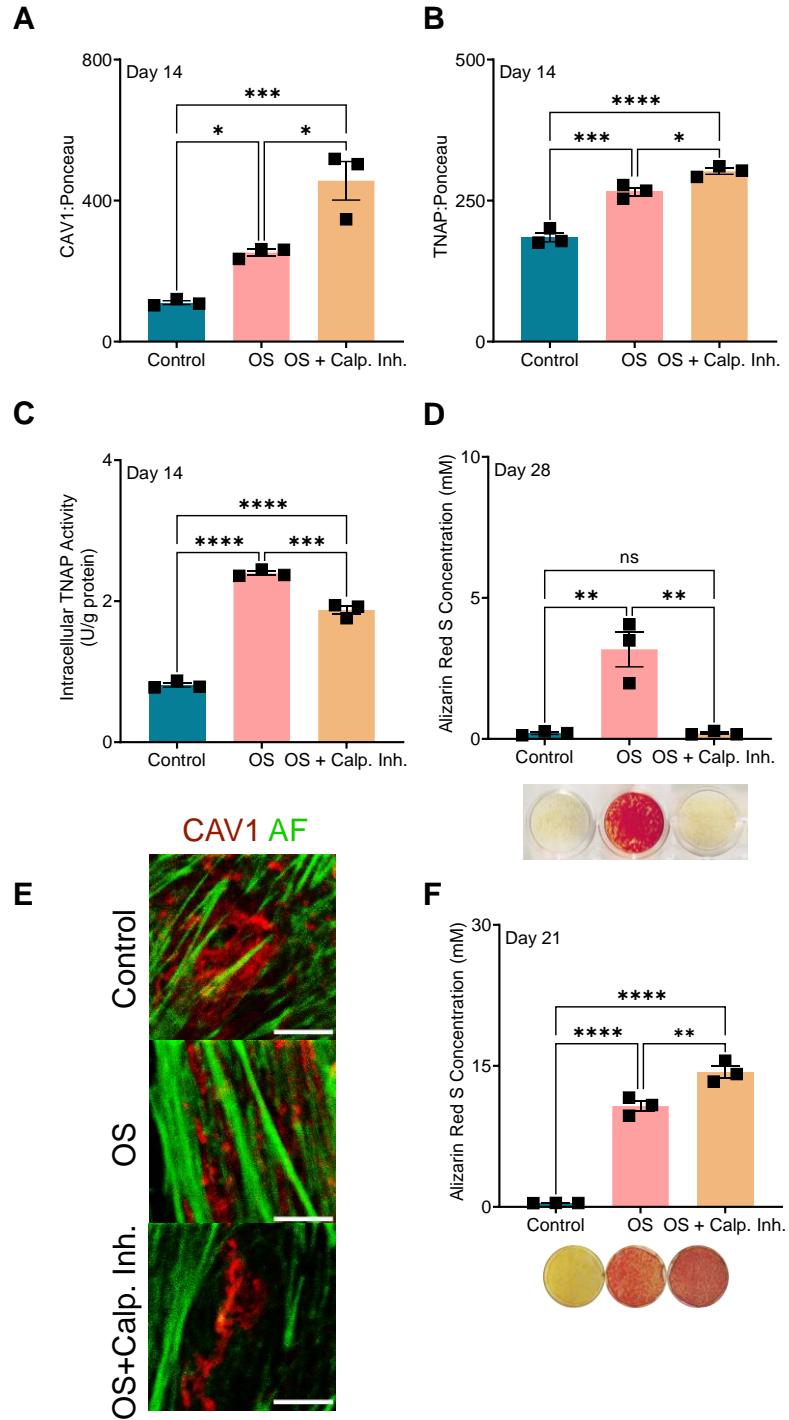


Figure 9. Calpain inhibitor prevents in vitro calcification of VSMCs. (A and B) Intracellular CAV1 and TNAP protein in VSMCs after 14 days of culture; (C) Intracellular TNAP activity in VSMC cultures following 14 days of treatment; (D) Alizarin red staining and quantification in VSMC cultures after 28 days; (E) Immunofluorescence staining of VSMCs after 14 days of treatment (400 $\times$ , scale bar 10  $\mu$ m); and (F) Alizarin red staining and quantification in osteoblasts cultures following 21 days. \* $P < 0.05$ , \*\* $P \leq 0.01$ , \*\*\* $P \leq 0.001$ , and \*\*\*\* $P \leq 0.0001$ , ANOVA with Tukey's post-hoc test.

***Rho-associated protein kinase inhibition prevents in vitro calcification of vascular smooth muscle cells***

Y-27632, a cell-permeable small molecule, inhibits the activity of the ROCK [138]. Our results showed that ROCK inhibition leads to elevated intracellular CAV1 in VSMCs (**Fig. 10, A**). The level of intracellular TNAP and TNAP activity increased in both OS and OS co-treated with ROCK inhibitor, with no significant differences between these two groups (**Fig. 10, B and C**). Despite no changes in TNAP activity level in ROCK inhibited cultures, Alizarin red staining showed complete prevention of in vitro calcification of VSMCs following 28 days of treatment (**Fig. 10, D**). ROCK inhibitor Y-27632 reduces cellular contractility by affecting actin filament formation [139]; our confocal micrograph showed thin and disrupted stress fiber in VSMC cultures treated with ROCK inhibitor compared to OS cultures. ROCK inhibition also affected the distribution of CAV1 by forming protein clusters (**Fig. 10, E**). Interestingly, ROCK inhibition using Y-27632 did not prevent in vitro mineralization of osteoblasts (**Fig. 10, F**).

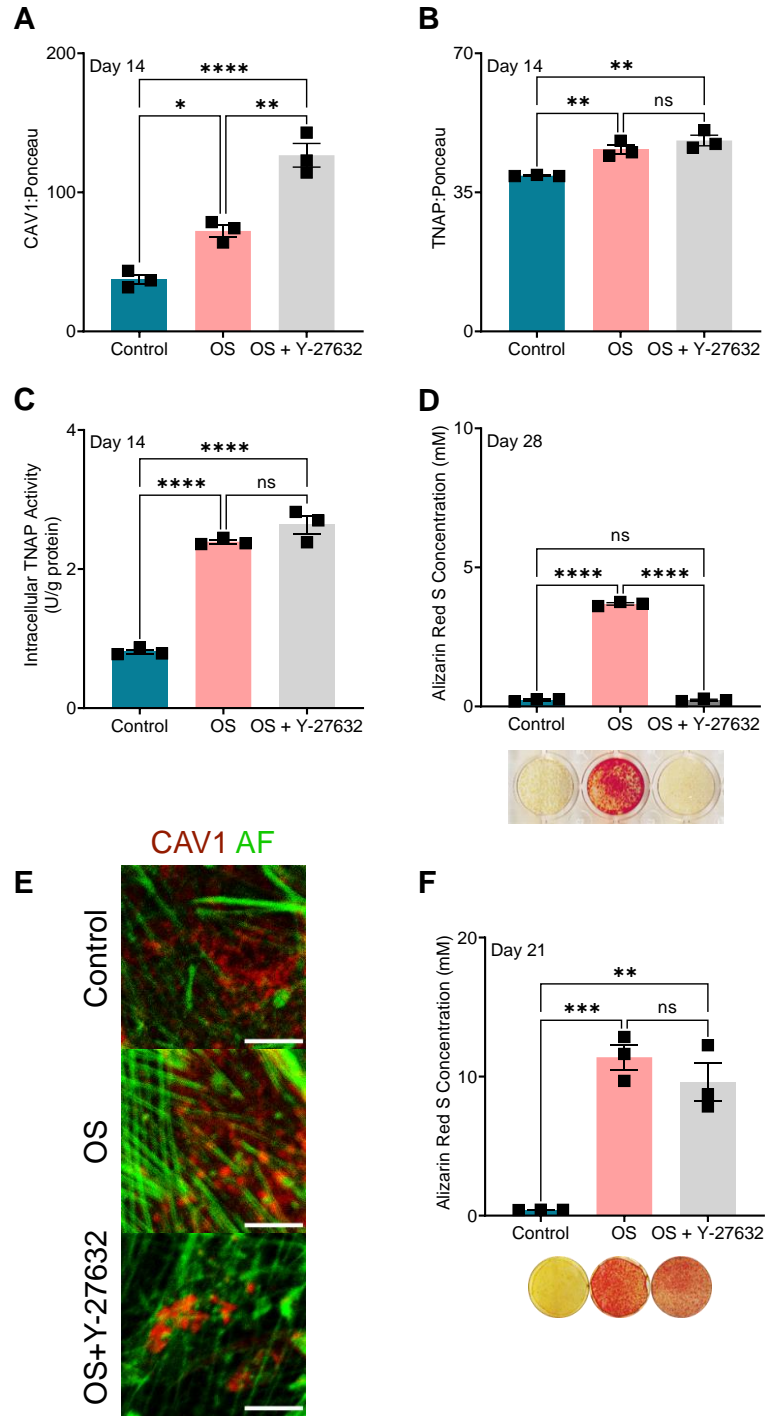


Figure 10. ROCK inhibitor prevents in vitro calcification of VSMCs. (A and B) Intracellular CAV1 and TNAP protein in VSMCs after 14 days of culture; (C) Intracellular TNAP activity in VSMC cultures following 14 days of treatment; (D) Alizarin red staining and quantification in VSMC cultures after 28 days; (E) Immunofluorescence staining of VSMCs after 14 days of treatment (400 $\times$ , scale bar 10  $\mu$ m); and (F) Alizarin red staining and quantification in osteoblasts cultures following 21 days. \* $P < 0.05$ , \*\* $P \leq 0.01$ , \*\*\* $P \leq 0.001$ , and \*\*\*\* $P \leq 0.0001$ , ANOVA with Tukey's post-hoc test.

***Rac1 inhibition prevents vascular smooth muscle cell calcification in vitro***

Rac1 inhibition increased the intracellular protein levels of CAV1 and TNAP compared to both control and OS conditions (**Fig. 11, A and B**). Interestingly, intracellular TNAP activity, which was significantly elevated in OS cultures, decreased to control levels in Rac1 inhibited VSMCs (**Fig. 11, C**). Following 28 days of culture, Rac1 inhibition completely prevented VSMCs calcification (**Fig. 11, D**). Our fluorescence staining showed qualitatively stronger stress fibers with clusters of CAV1 between filaments in Rac1-inhibited VSMCs (**Fig. 11, E**). However, Rac1 did not affect mineralization of the osteoblasts (**Fig. 11, F**).

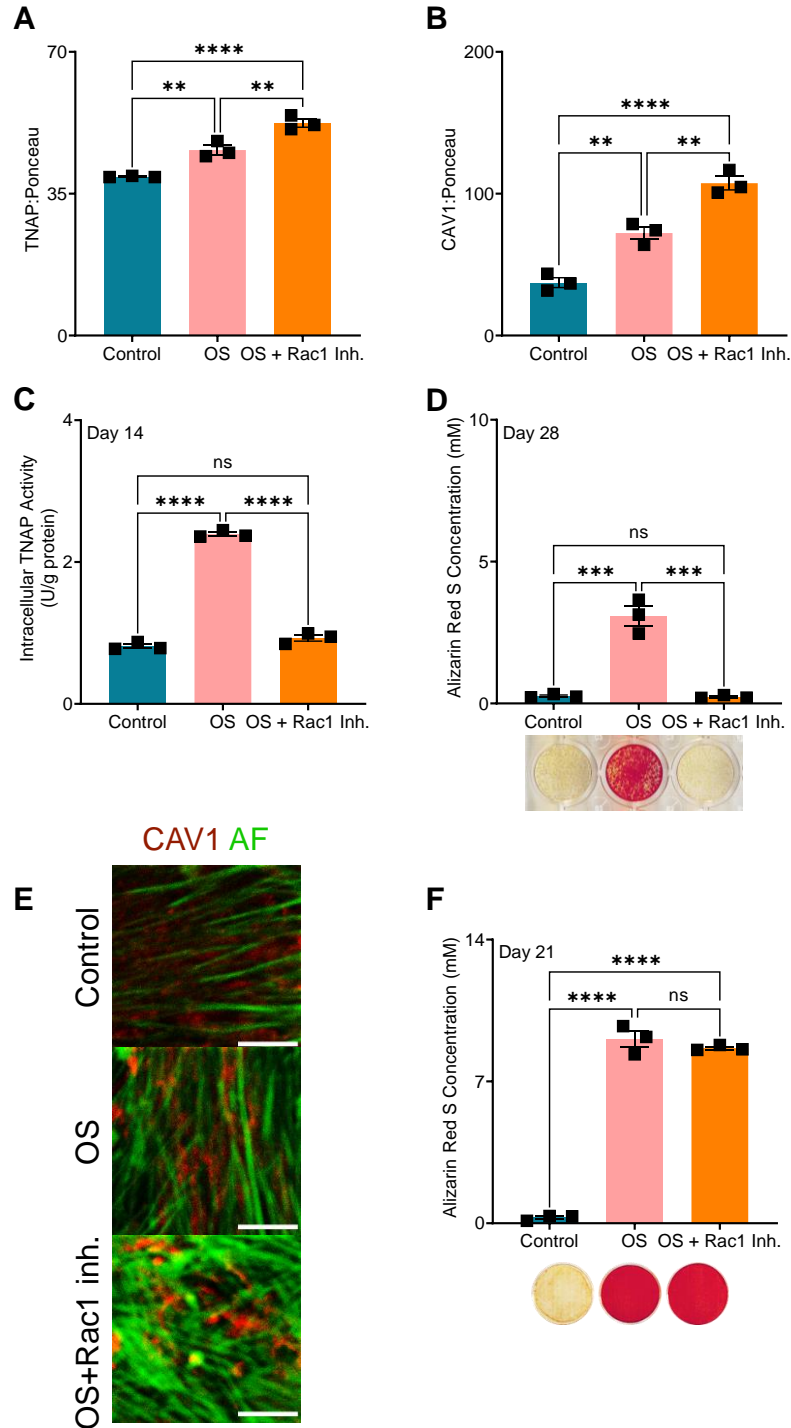


Figure 11. Rac1 inhibitor prevents in vitro calcification of VSMCs. (A and B) Intracellular CAV1 and TNAP protein in VSMCs after 14 days of culture; (C) Intracellular TNAP activity in VSMC cultures following 14 days of treatment; (D) Alizarin red staining and quantification in VSMC cultures after 28 days; (E) Immunofluorescence staining of VSMCs after 14 days of treatment (400 $\times$ , scale bar 10  $\mu$ m); and (F) Alizarin red staining and quantification in osteoblasts cultures following 21 days. \* $P < 0.05$ , \*\* $P \leq 0.01$ , \*\*\* $P \leq 0.001$ , and \*\*\*\* $P \leq 0.0001$ , ANOVA with Tukey's post-hoc test.

***Targeting cholesterol-rich domains in VSMCs membrane increases in vitro calcification***

CAV1 protein resides in caveolar lipid raft domains, which contain high level of cholesterol. Methyl- $\beta$ -cyclodextrin (m $\beta$ CD) selectively removes the cholesterol from plasma membrane [140, 141] and disrupts caveolar domains [142]. Our results showed increased intracellular CAV1 in both OS and OS co-treated with m $\beta$ CD in VSMCs compared to non-treated controls; however, m $\beta$ CD reduced intracellular CAV1 compared to OS culture alone (**Fig. 12, A**). OS media increased the level of total cholesterol in VSMCs and removing the cholesterol domains from the membrane using m $\beta$ CD significantly increases the total cholesterol measured in the VSMCs (**Fig. 12, B**). Intracellular TNAP activity increased in OS cultures co-treated with m $\beta$ CD compared to both control and OS media (**Fig. 12, C**). Elevated TNAP activity associated with significantly higher in vitro calcification of VSMCs compared to OS culture (**Fig. 12, D**).

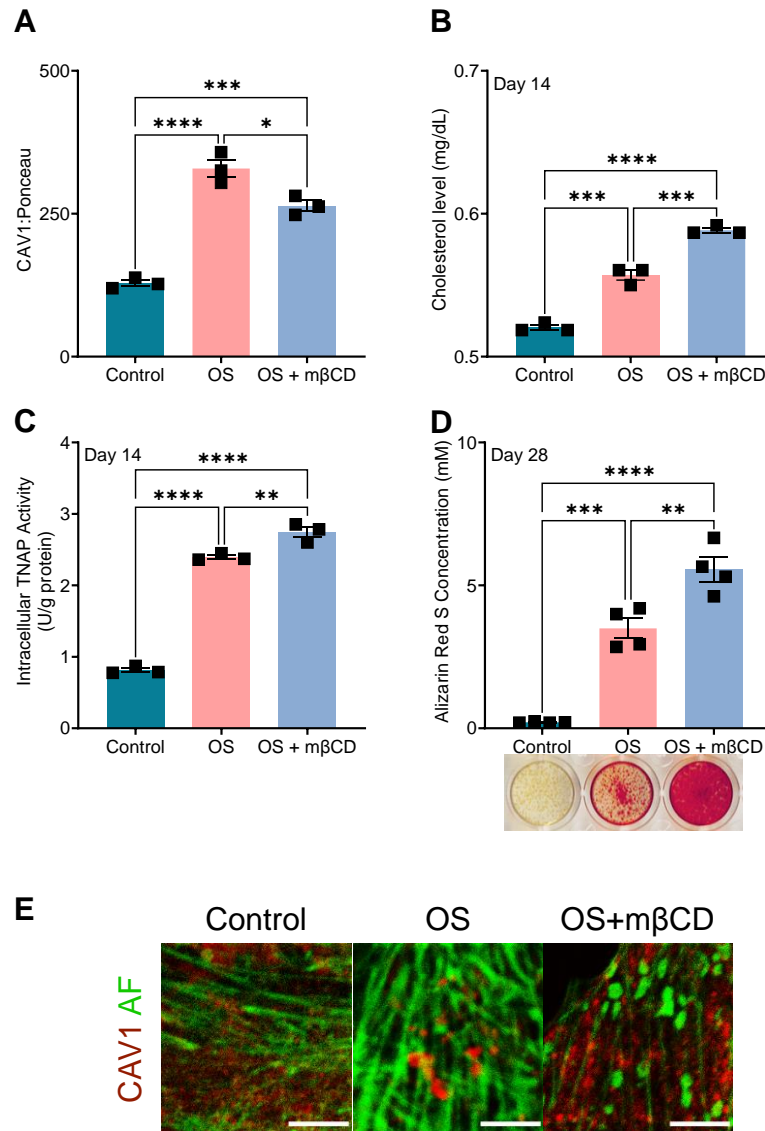


Figure 12. mβCD increases in vitro calcification of VSMCs. (A) Intracellular CAV1 in VSMCs after 14 days of culture; (B) Intracellular cholesterol level following 14 days of treatment in VSMCs; (C) Intracellular TNAP activity in VSMC cultures following 14 days of treatment; (D) Alizarin red staining and quantification in VSMC cultures after 28 days; (E) Immunofluorescence staining of VSMCs after 14 days of treatment (400×, scale bar 10 μm). \*P < 0.05, \*\*P ≤ 0.01, \*\*\*P ≤ 0.001, and \*\*\*\*P ≤ 0.0001, ANOVA with Tukey's post-hoc test.

mβCD prevented mineralization of osteoblasts after 21 days of treatment (**Fig. 13, A**). Interestingly, mβCD treatment decreased intracellular TNAP activity to the control level (**Fig. 13, B**). OS media increased intracellular CAV1 in osteoblasts; interestingly, co-treatment with OS media and mβCD dramatically reduced CAV1 level to the control level (**Fig. 13, C**). Like VSMC cultures, mβCD

increased the total intracellular cholesterol measured in osteoblasts (**Fig. 13, D**). Following 14 days of culture, the expression of *RUNX2* in osteoblasts under both OS media and OS supplemented with m $\beta$ CD was reduced (**Fig. 13, E**), indicating a commitment to osteogenic differentiation [143, 144]. m $\beta$ CD increased the expression of *BGLAP* in osteoblasts to higher level compared to OS media (**Fig. 13, H**). However, both *COL1A1* and *ALPL* expression were significantly reduced by m $\beta$ CD treatment in OS cultures (**Fig. 13, F and G**).

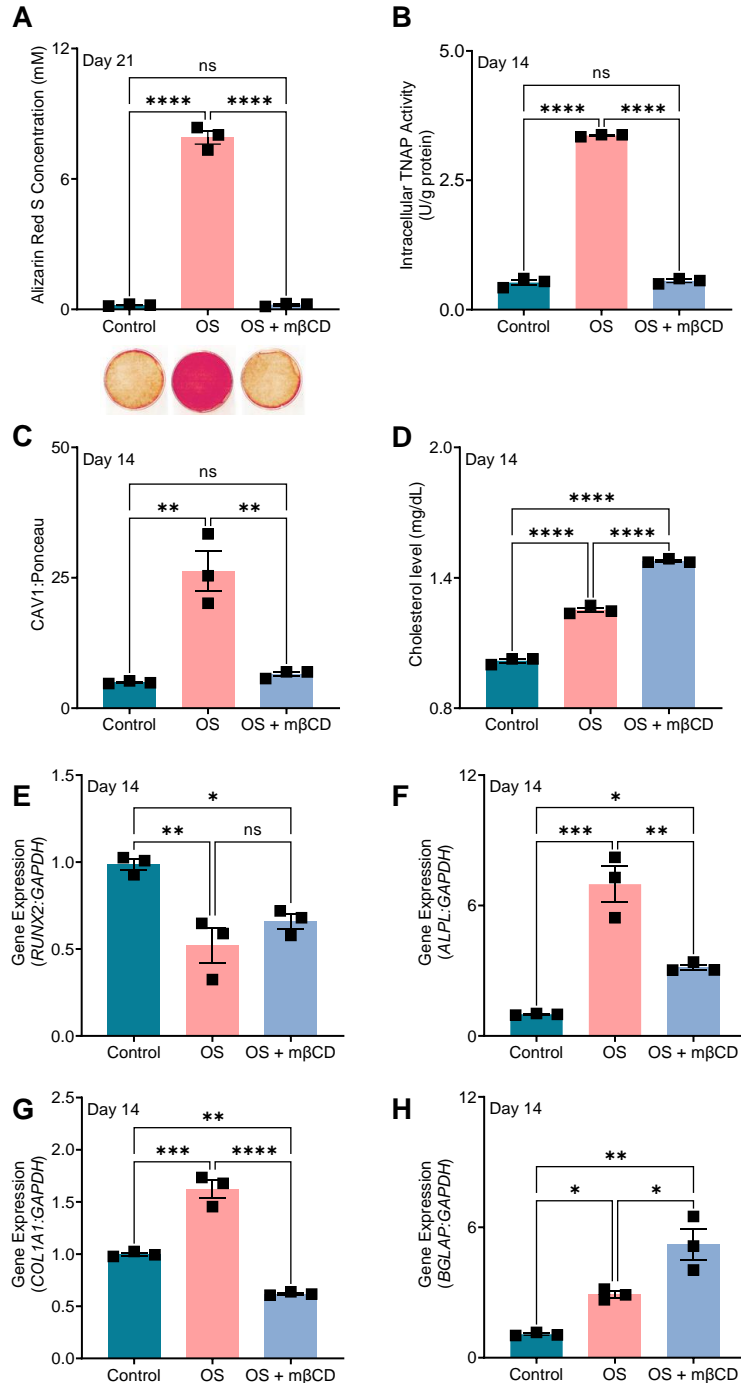


Figure 13. MβCD prevents in vitro calcification of osteoblasts. (A) Alizarin red staining and quantification in osteoblasts cultures after 21 days; (B) intracellular TNAP activity in osteoblasts following 14 days of treatment; (C) Intracellular CAV1 in osteoblasts after 14 days of culture; (D) Intracellular cholesterol level following 14 days of treatment in osteoblast; (E, F, G, and H) gene expression changes in osteoblasts following 14 day of treatment for *RUNX2*, *ALPL*, *COL1A1*, and *BGLAP*, respectively. \* $P < 0.05$ , \*\* $P \leq 0.01$ , \*\*\* $P \leq 0.001$ , and \*\*\*\* $P \leq 0.0001$ , ANOVA with Tukey's post-hoc test.

#### 4.4. Discussion

The formation of cardiovascular calcification involves VSMC-derived calcifying EVs that serve as nucleating foci for mineralization. This process mimics physiological bone mineralization by osteoblasts. However, reduction in bone mineral density correlates with elevated cardiovascular calcification—a phenomenon known as the “calcification paradox [6].” Yet, the cellular processes that distinguish VSMC-dependent calcification from osteoblasts are unclear. Previous studies reported that a membrane scaffolding protein, CAV1, actively participates in the biogenesis of calcifying EVs in VSMCs. CAV1 abundantly resides in caveolar domains, cholesterol-rich membrane rafts that play a critical role in cardiovascular physiology [145]. CAV1 may represent a key to understand the divergence between VSMC and osteoblast mineralization. Silencing of CAV1 reduced intracellular TNAP activity and in vitro calcification of VSMCs. However, in vivo studies in CAV1<sup>-/-</sup> mice revealed increased bone mass density. Our data showed that CAV1 knockdown does not affect the in vitro mineralization of osteoblasts, which supports our hypothesis that CAV1 is required for VSMC mineralization specifically. Here, we investigated known CAV1 interactors in modulating VSMC and osteoblast calcification.

We showed that Src tyrosine kinase (a non-receptor membrane protein) inhibition prevents VSMC-dependent calcification but does not affect mineralization by osteoblasts. Src tyrosine kinase inhibition elevated intracellular CAV1 level and altered CAV1 patterns within VSMCs. Furthermore, Src tyrosine kinase inhibition increased TNAP protein levels but decreased TNAP activity. CAV1 endocytosis and trafficking through the Golgi apparatus activates TNAP in VSMCs [1]. Our data suggest that although the OS media still leads to increased TNAP protein, Src inhibition disrupts CAV1 trafficking and prevents TNAP activation. Of note, several clinical trials are studying the efficacy of STK inhibitors in cancer therapy, diabetes, and chronic kidney disease [146, 147]. However, STK inhibitors as a diverse family require comprehensive studies for their potential cardiovascular therapeutic outcomes.

We also assessed the role of FLNA modulation in VSMC-dependent calcification. FLNA is a F-actin crosslinking protein that interacts with CAV1 during caveolar domain endocytosis [127]. FLNA-knockdown endothelial cells constrained CAV1 to the plasma membrane, while in control group CAV1 was detected on intracellular vesicles, thus, FLNA mediates CAV1 trafficking within the cell [127]. Our results indicate elevated intracellular CAV1 in Calpain inhibited cultures, which may result from altered CAV1 trafficking due to FLNA stabilization. Furthermore, fluorescence staining showed clusters of CAV1 in Calpain inhibited VSMCs, which supports disrupted CAV1 trafficking. Similar to Src tyrosine kinase inhibitor, Calpain inhibition increased the level of intracellular TNAP, but reduced TNAP activity in VSMCs. These results further indicate that disrupting CAV1 trafficking affects TNAP activation. Interestingly, targeting FLNA solely prevents calcification of VSMCs without affecting osteoblast mineralization. Several studies reported the targeting of FLNA to hinder tumor progression in cancer mouse models [148, 149] and neurological disorders [150], but no cardiovascular-related *in vivo* study has been reported. Future studies will assess the role of FLNA targeting and its therapeutic efficacy in cardiovascular-related pathologies.

Previous studies demonstrated that differentiation and calcification of mesenchymal stem cells require cytoskeletal rearrangements that lead to actin filaments thickening [116]. Actin filaments regulate cellular contractility [151], and osteogenic stimulation increased cell contraction. Disrupting the actin filaments reduces the calcification [152]. We also showed that *in vitro* calcification of VSMCs requires cellular contractility. ROCK plays a role in VSMC contraction, by regulating focal adhesions and stress fiber formation [153]. Y-27632 targets p160ROCK (a protein serine/threonine kinase [154, 155]) and actively prevents stress fibers formation [156], and consequently reduces osteogenic-mediated VSMC contraction. Fluorescence images showed that ROCK inhibition in our VSMCs cultures qualitatively reduced the density and thickness of the stress fibers. ROCK inhibition also redistributed CAV1 in VSMCs. Similar to the calpain and Src inhibition data, intracellular CAV1 was elevated in ROCK-inhibited VSMCs, which may indicate

disrupted CAV1 trafficking. However, neither intracellular TNAP nor TNAP activity was affected by ROCK inhibition. These outcomes suggest that ROCK inhibitor prevents vascular calcification differently from the other CAV1 interactors. ROCK inhibition did not hinder in vitro calcification of osteoblasts. Further studies are needed to investigate the efficacy and safety of ROCK inhibition strategies in cardiovascular pathologies.

We showed that Rac1 inhibition attenuated in vitro calcification of the VSMCs. Rac1, promotes non-contractile stress fiber assembly [157]. Our fluorescence images qualitatively indicated stronger actin filaments with clusters of CAV1 following Rac1 inhibition. Furthermore, intracellular CAV1 increased in response to Rac1 inhibition, which may suggest disrupted CAV1 trafficking. Despite elevated intracellular TNAP protein, the activity of this enzyme significantly decreased, similar to the trends observed with calpain and Src inhibition. Rac1 inhibition did not prevent osteoblast mineralization.

The effects of m $\beta$ CD may represent the most interesting results in this chapter. Removal of caveolar domains from VSMCs significantly increased in vitro calcification, but completely abrogated the osteoblasts mineralization. The elevated VSMC-dependent calcification associated with increased intracellular TNAP activity. Our results showed elevated intracellular CAV1 in both OS cultures and m $\beta$ CD treated VSMCs. Previous studies reported that m $\beta$ CD prevents stress fiber assembly [141], which is consistent with our observations. We expected that depolymerization of the actin stress fibers would reduce VSMC-dependent calcification; however, we observed the opposite outcome. Interestingly, m $\beta$ CD hinders osteoblasts mineralization by affecting osteogenic differentiation. Reduced *COL1A1* expression in osteoblasts suggests an inability to synthesize a mature extracellular matrix for mineral deposition. Decreased ALPL expression also led to a significant reduction in intracellular TNAP activity. For both VSMCs and osteoblasts, intracellular cholesterol unexpectedly increased in m $\beta$ CD cultures. This may be due to lipid addition mechanisms within cells that compensates for constant cholesterol depletion at the membrane

[158]. Further studies are needed to clarify the relation between cholesterol-depletion, CAV1 trafficking, and calcification.

#### **4.5. Summary**

VSMC calcification depends on CAV1 protein and endocytosis of caveolar domains [1, 5]. Thus, CAV1 and its interactors may represent ideal targets to develop therapeutic options to prevent VSMC-dependent calcification. We studied the role of inhibiting of several upstream and downstream molecules that are involved in CAV1 activation and trafficking. Interestingly, we showed that altering CAV1 trafficking does not negatively impact physiological mineralization of osteoblasts. We concluded that despite shared mineralization characteristics, the mechanism(s) of calcification is/are different in these cells. This suggests the possibility of developing therapeutic strategies that prevent vascular calcification, but not bone mineralization. In Chapter V, we investigate the therapeutic potential of a known CAV1 interactor and build upon our observations that altered CAV1 trafficking affects mineralization.

## **Chapter V: Aim 3 – Epidermal Growth Factor Receptor Inhibition Prevents Vascular Calcification**

Text for Chapter V taken from:

[159] – A. Bakhshian Nik, H. H. Ng, P. Sun, F. Iacoviello, P. R. Shearing, S. Bertazzo, D. Mero, B. B. Khomtchouk, and J. D. Hutcheson. "Epidermal Growth Factor Receptor Inhibition Prevents Caveolin-1-dependent Calcifying Extracellular Vesicle Biogenesis." *BioRxiv*, 2021.

### **5.1. Introduction**

Medial calcinosis manifests as the formation of calcium phosphate mineral in the media layer of arterial walls, leading to vascular stiffening, dysfunction, and cardiac overload [160, 161]. Medial calcinosis highly correlates with cardiovascular morbidity and mortality [162]. Calcification of arterial media commonly occurs in patients with chronic kidney disease (CKD) [161, 163]. CKD patients with no detectable vascular calcification have 8-year all-cause survival rates of around 90% compared to 50% survivability in age-matched patients with medial calcification [164]. Imbalanced serum calcium and phosphorous levels elevate the risk of medial calcinosis in CKD patients. Impaired renal excretion of phosphorous also leads to abnormal bone remodeling and mediates osteogenic differentiation of vascular smooth muscle cells (VSMCs) in the arterial walls [165].

Osteogenic differentiation of resident VSMCs and release of calcifying extracellular vesicles (EVs) mediate nucleation and growth of ectopic vascular calcification [162, 166]. This process mimics aspects of the physiological mineralization of osteoblasts and chondrocytes in bone via release of matrix vesicles [167]. Although calcifying EVs released into the vascular wall and bone matrix vesicles contribute to similar endpoints of mineralization, they originate through different pathways [33, 168]. The development of pharmaceuticals for vascular calcification targeting mechanisms specific to vascular calcifying EVs could avoid deleterious off-target effects on bone. Formation of calcifying EVs by VSMCs requires caveolin-1 (CAV1), a scaffolding membrane protein [169]. CAV1 resides in caveolar domains, small invaginations (50-100 nm) on the plasma membrane,

which consist of the caveolin protein family, cholesterol, sphingolipids, and receptors [170, 171]. Caveolar functions include intra/extracellular lipid transfer, endocytosis, mechanotransduction, and signaling mediation [171, 172]. Calcifying VSMCs release CAV1-enriched EVs, and CAV1 knockdown abrogates calcification in these cells [169].

Epidermal growth factor receptor (EGFR) is a tyrosine kinase transmembrane glycoprotein [173], which localizes abundantly in caveolar domains. EGFR interacts with and modulates CAV1 trafficking [174] and recruits signaling proteins to caveolar domains [175]. EGFR actively participates in human cancer progression, and EGFR tyrosine kinase inhibition has become a widely utilized strategy in cancer therapies [176]. Both CAV1 and EGFR are elevated during breast cancer progression [177], and clinical studies indicate that overexpression of EGFR in breast cancer associates with increased ectopic calcification [178]. In cardiovascular pathogenesis, elevated EGFR activity correlates with oxidative stress and chronic inflammation [179]. EGFR inhibition in apolipoprotein E-deficient mice fed a high-fat diet prevented atherosclerotic plaque development [179]. However, the role of EGFR in VSMC-mediated calcification has not been reported.

Here, we computationally analyzed 7651 individuals in the Multi-Ethnic Study of Atherosclerosis (MESA) and Framingham cohorts, revealing a positive correlation between genetically mediated serum EGFR and coronary artery calcification (CAC) measured by computed tomography. Given these associations and the known interactions between CAV1 and EGFR, we hypothesized that EGFR inhibition would prevent vascular calcification by mitigating the biogenesis of calcifying EVs. We showed that EGFR inhibition reduces the release of pro-calcific CAV1-positive EVs and prevents calcification in osteogenic VSMC cultures and in CKD mice fed a high-phosphate diet. The EGFR inhibitor treatment also significantly reversed bone mineral loss in the CKD mice. Given the demonstrated clinical safety, our data suggest that EGFR inhibition could represent a viable therapeutic strategy to prevent vascular calcification in patients with CKD.

## 5.2. Methods

### *Identification of Instrumental Variables for Mendelian Randomization*

Instrumental variables (IVs) were selected using an agnostic p-value threshold, i.e.  $p < 5 \times 10^{-6}$ , as advised by the methodological literature on Mendelian Randomization (MR) [180]. Single nucleotide polymorphisms (SNPs) associated with significantly elevated serum EGFR concentration ( $p < 5 \times 10^{-6}$ ) from a previous proteomics study were compared against genotyped SNPs in the Multi-Ethnic Study of Atherosclerosis (MESA) SNP Health Association Resource (SHARe), and all SNPs presented in both the proteomics study and MESA genotyping data associated beyond this p-value threshold were included as IVs for the MR analysis [181]. In total, three SNPs of rs12666347, rs2371816, and rs7806938 were included. The same 3 IVs and measure of CAC were used to replicate the significance of the MR analysis and validate results in the Offspring Cohort of the Framingham Heart Study (FHS).

### *Calculation of SNP-EGFR and SNP-CAC Association in the MESA and FHS Cohorts*

Effect sizes of each SNP on EGFR concentration, as well as their standard errors, were extracted from the publicly available summary statistics [181]. To calculate the effect sizes of each SNP on calcification levels, we identified 1,896 individuals from the FHS Offspring cohort, and 5,755 individuals who completed MESA Exam 1 who had available genotyping information. For each of these individuals, genotyping information, age, sex, study site, race, and Agatston score were extracted. Agatston scores are a measure of CAC determined through cardiac imaging, with an increasing Agatston score representing increased CAC. Associations between each IV SNP and CAC is calculated using logistic regression, treating Agatston scores as a binary variable ( $= 0$  vs  $> 0$ ) and including age, sex, study site, and race as covariates in the model. All analyses were conducted using the R programming language.

### ***Mendelian Randomization***

Following identification of SNP-CAC and SNP-EGFR association and standard error values, MR analysis was performed to determine the presence and estimate the magnitude of causal effect that elevated serum EGFR has on CAC. 11 different regressions were included in the MR analysis to correct for possible pleiotropic effects, a possible source of confounding. Included regressions were simple median, weighted median, penalized median, inverse-variance weighted (IVW), penalized IVW, robust IVW, penalized-robust IVW, MR-Egger, penalized MR-Egger, robust MR-Egger, and penalized-robust MR-Egger. MR analysis was performed using the Mendelian Randomization package in R [182, 183] (R Core Team, 2021; Yavorska and Staley, 2021). We accounted for multiple testing errors using a Bonferroni-adjusted 0.05 significance level of 0.0045 (0.05/11).

### ***Chronic Kidney Disease and Vascular Calcification Mouse Model***

The *in vivo* study was approved by the Institutional Animal Care and Use Committee (IACUC) at Florida International University under protocol AN20-006 and conformed to current NIH guidelines. The experimental design was based upon procedures established in a previous study to induce CKD and vascular calcification in mice [184]. 8-week-old wild type C57BL/6J mice (n = 38, 19 per biological sex) were fed an adenine-supplemented diet (0.2%, TestDiet, Richmond, IN) for 6 weeks to induce severe kidney injury. The mice then received a diet containing 1.8% phosphate (TestDiet, Richmond, IN) and 0.2% adenine for an additional two weeks to induce medial calcinosis. Along with this calcifying diet, a group of mice (n = 19) received daily tyrphostin AG1478 (10 mg/kg mouse, Millipore Sigma, T4182) via oral gavage. The remaining mice (n = 19) received vehicle treatment (1% w/v, carboxymethylcellulose sodium salt, Sigma, C5678). For non-diseased controls, a third group of mice (n = 12, 6 per biological sex) were fed a regular chow diet and received the vehicle for the final two weeks. During the oral gavage, animals were partially anesthetized using isoflurane (1%, Patterson Veterinary, 07-893-1389, in 2 L.min<sup>-1</sup> oxygen flow).

All animals received a tail vein injection with the calcium tracer OsteoSense 680EX (80 nmol/kg mouse, PerkinElmer, NEV10020EX) 48 hours prior to euthanization. At study endpoint, mice were anesthetized with isoflurane (1%, in 2 L.min<sup>-1</sup> oxygen flow) followed by retro-orbital bleeding for blood collection. Mice were then immediately euthanized by laceration of the diaphragm before tissue collection. After resection, the aortas were imaged using a near-infrared scanner (LI-COR Odyssey) to visualize the vascular calcification burden. A custom MATLAB script quantified the total area of the calcium tracer, which was normalized to the total scanned aorta area.

Immediately after scanning, the tissue was incubated in a digestive solution [185] of sucrose (0.25 M, Sigma, S7903), NaCl (0.12 M, Fisher Chemical, BP358), KCl (0.01 M, Fisher Chemical, P217), Tris hydrochloride (0.02 M, Fisher Chemical, BP153), and collagenase (600 U/mL, Worthington Biochemical, LS004174) for 2 hours at 37°C. The solution was then centrifuged at 1,000×g for 15 min to remove cell debris and at 33,000×g for 30 min to remove microvesicles. Finally, the supernatants were ultracentrifuged (Beckman Coulter, Optima MAX-TL) at 100,000×g for 1 hour to isolate the EVs of interest. The pellet was suspended in RIPA lysis and extraction buffer (G Biosciences, 786-489) supplemented with pierce protease inhibitor (Thermo Scientific, A32963). To yield sufficient protein concentration for analysis, EVs isolated from 2 to 3 aortas were pooled.

### ***Osteogenic Stimulation, In vitro Calcification, and Extracellular Vesicle Isolation***

Primary human coronary artery vascular smooth muscle cells (VSMCs, ATCC, PCS-100-021) were cultured using vascular smooth muscle cell media and growth kit (ATCC, PCS-100-042). VSMCs (passage 4-6) were harvested using 0.05% trypsin-EDTA solution (Caisson Labs, TRL04) and seeded with a density of 26,320 cells.cm<sup>-2</sup> and incubated for 72 hours at 37°C, 5% CO<sub>2</sub> with controlled humidity prior to treatment. VSMCs were treated with either control media, consisting of DMEM (HyClone, SH30022.01), 10% v/v bovine calf serum (iron-supplemented, R&D Systems, S11950), and 1% v/v penicillin-streptomycin (Gibco, 15070-063), or with an osteogenic media (OS) optimized to induce calcification [5, 136]. OS media were supplemented with 10 mM

$\beta$ -glycerophosphate (Sigma, 13408-09-8), 0.1 mM L-ascorbic acid (Sigma, 113170-55-1), and 10 nM dexamethasone (Sigma, 50-02-2). To assess the role of EGFR inhibition, tyrphostin AG1478 (Millipore Sigma, T4182) was dissolved in the vehicle (DMSO:Methanol, 1:1) and added to OS media to a final concentration of 2.5  $\mu$ M. An equal volume of the vehicle was added to the control and OS groups. We found that 28 days in OS culture media led to robust calcification by VSMCs; therefore, all cultures (n = 3, independent donors, male and female) were treated for 28 days and media were replaced every three days. On days 6, 13, 20, and 27 the media were replaced by an extracellular-vesicle-free (EV-free) media (ultracentrifuged for 15 hours at 100,000 $\times$ g at 4 $^{\circ}$ C to remove background EVs common in the serum). After 24 hours, conditioned media were collected on days 7, 14, 21, and 28. Collected media were centrifuged at 1,000 $\times$ g for 5 min to remove cell debris. EV isolation was performed using ultracentrifugation at 100,000 $\times$ g for 1 hour.

Osteoblasts (from human fetus, hFOB 1.19, ATCC, CRL-11372) were cultured and grown in DMEM containing 10% v/v bovine calf serum and 1% v/v penicillin-streptomycin. Osteoblasts (passage 4-6) were harvested using 0.25% trypsin-EDTA solution (Caisson Labs, TRL01), seeded with a density of 5,200 cell.cm<sup>-2</sup>, and incubated for 24 hours at 37 $^{\circ}$ C and 5% CO<sub>2</sub> with controlled humidity. The cells were treated in three groups of control, OS, and OS supplemented with tyrphostin AG1478 (2.5  $\mu$ M) for 21 days and media were changed every three days. Compared to VSMCs, we observed more rapid mineralization in osteoblasts cultured in OS with full matrix mineralization apparent after 21 days. Similar to the VSMC experiments, EV-free media were added to the cultures on days 6, 13, and 20, and collected 24 hours later on days 7, 14, and 21. Collected media were centrifuged at 1,000 $\times$ g for 5 min to remove cell debris. Matrix vesicles were isolated using the ultracentrifugation at 100,000 $\times$ g for 1 hour.

### ***Alizarin Red S Staining and Quantification***

At the end of experiments (28 and 21 days of treatment for VSMCs and osteoblasts, respectively), media were removed, and the cells were fixed using formalin (10%, Fisher Chemical, SF100) for

15 min. To visualize *in vitro* calcification, Alizarin Red S stain (ARS, Ricca, 500-32) was added to the wells and incubated for 30 min at room temperature. The stain was then removed, and the cells were washed three times with milliQ water. To quantify the *in vitro* calcification, ARS stain was extracted using acetic acid (1.67 M, Fisher Chemical, A38S) on a shaker. After 30 min, the supernatants were collected, briefly vortexed, and heated at 85°C for 10 min. The samples were then cooled on ice for 5 min and centrifuged at 20,000×g for 15 min to remove background particles. Sample absorbance of 405 nm light was measured using a multi-mode reader (BioTek, Synergy HTX).

### ***Kidney Histological Analysis***

To assess histological changes in kidneys due to renal injury, Hematoxylin and Eosin (H&E) staining was performed. The kidneys resected from the mice were fixed using formalin (10%) for three hours. Tissues were embedded using Tissue-Plus OCT (Fisher Scientific, 23-730-571). The samples were cryosectioned with a thickness of 12 µm and stained using rapid chrome H&E staining kit (Thermo Scientific, 9990001).

### ***Quantitative Real Time Polymerase Chain Reaction***

Following 7 or 14 days in control, OS, or OS plus EGFR inhibitor media, VSMCs and osteoblasts were lysed in 1 mL TRIzol solution (Invitrogen, 15596018). Total RNA was isolated according to the manufacturer's protocol. To perform the quantitative real time polymerase chain reaction (qRT-PCR), Power SYBR Green RNA-to-CT 1-Step Kit (Applied Biosystems, 4391178) was used. 50 ng of isolated template RNA were added to each reaction for qRT-PCR. The results were normalized to Glyceraldehyde 3-phosphate dehydrogenase (GAPDH) expression level as the housekeeping control. The relative gene expression levels were calculated using comparative CT method, considering control groups as the reference. The following human primers were purchased from Integrated DNA Technologies (IDT); *GAPDH* Forward:

CTTCGCTCTCTGCTCCTCCTGTTTCG and Reverse: ACCAGGCGCCCAATACGACCAAAT;  
*RUNX2* Forward: GCTCTCTAACCACAGTCTATGC and Reverse:  
AGGCTGTTTGATGCCATAGT; *ALPL* Forward: GGAGTATGAGAGTGACGAGAAAG and  
Reverse: GAAGTGGGAGTGCTTGTATCT; *Osteocalcin (BGLAP)* Forward:  
TCACACTCCTCGCCCTATT and Reverse: CTCCTGCTTGGACACAAAA.

To isolate RNA from the resected kidneys, the tissues were homogenized using a grinder (Sigma, Z529672) and lysed in 1 mL TRIzol solution. After 10 min incubation at room temperature, the samples were centrifuged at 12,000×g for 10 min at 4°C. The supernatants were collected and 200 µL of chloroform (Sigma Aldrich, C2432) were added to each sample. The samples were vortexed, incubated at room temperature for 10 min, and centrifuged for 15 min at 12,000×g, 4°C. The aqueous phase was collected from each sample and 500 µL of isopropanol were added; the samples were vortexed, incubated for 15 min at room temperature followed by 15 min on ice, and centrifuged at 21,000×g for 15 min. The supernatants were discarded, and pellets were washed twice with 500 µL cold ethanol (75% v/v) and centrifuged at 21,000×g for 5 min [186-188]. The isolated RNA templates were heated at 65°C for 15 min, and the concentrations were measured using a spectrophotometer (NanoDrop Lite, Thermo Scientific). Power SYBR Green RNA-to-CT 1-Step Kit with 100 ng isolated template RNA per reaction was used. The following mouse primers were purchased from Eurofins Scientific; *Gapdh* Forward: AACGACCCCTTCATTGAC and Reverse: TCCACGACATACTCAGCAC; *Colla1* Forward: CTCAGGGTATTGCTGGACAAC and Reverse: ACCACTTGATCCAGAAGGACCTT; *Tgfb1* Forward: TGGAGCAACATGTGGAACTC and Reverse: CAGCAGCCGTTACCAAG.

### ***Alkaline Phosphatase Activity Assay***

To assess the activity of intracellular tissue non-specific alkaline phosphatase (TNAP), a colorimetric assay kit (BioVision, K412) was used. VSMCs (n = 3) after 14 days and osteoblasts (n = 3) after 7 days, were lysed in 120 µL assay buffer. 80 µL of each sample were mixed with 50

$\mu\text{L}$  of 5 mM pNPP solution and incubated for 60 min at 25°C. The colorimetric change resulting from the reaction was detected using a plate reader to measure absorbance at 405 nm. The results were normalized to the total protein for associated samples measured by a BCA protein assay (BioVision, K813). For EV or matrix vesicle TNAP activity measurement, after ultracentrifugation at 100,000 $\times g$  for 1 hour, the pellets were re-suspended in 120  $\mu\text{L}$  assay buffer. The assessment was performed using the same assay protocol described for intracellular TNAP activity and the results were normalized to the total protein for each sample. For mouse serum TNAP activity, the samples were diluted 1:20 and assessed according to the manufacturer's protocol.

### ***Extracellular Collagen Assessment***

After 28 days of treatment, soluble collagen was extracted from the cultures using acetic acid (0.5 M) through overnight incubation at 4°C. A colorimetric assay, Sircol soluble collagen assay (Biocolor, S1000), measured the total soluble extracellular matrix (ECM) collagen in each group. Samples were prepared and assessed according to the manufacturer's protocol. Results were then normalized to the total protein measured using BCA assay.

### ***Subcellular Fractionation for VSMCs and Aortas***

8-week-old wild type C57BL/6J mice (n = 20, female) received the adenine-supplemented diet for 6 weeks to induce CKD, followed by two additional weeks of the diet containing 1.8% phosphate and 0.2% adenine to induce medial calcinosis. Mice were split into two groups (10 per group). The first group received daily tyrphostin AG1478 (10 mg/kg mouse), while the other group received vehicle (1% w/v, carboxymethylcellulose sodium salt). At study endpoint, the animals were euthanized, and the aortas were resected. A subcellular protein fractionation kit for tissue (ThermoFisher, 87790) was used to isolate cellular cytosolic fraction from the resected aortas, using the manufacturer's protocol. Briefly, the tissues were minced and homogenized using a grinder. The samples were then incubated in a cytoplasmic extraction buffer for 10 min at 4°C, followed by

centrifugation at 1000×g for 5 min. The supernatants yielded the cytosolic fraction. To obtain sufficient protein for analyses, two aortas were pooled per data point.

VSMCs were treated with control, OS, and OS supplemented with tyrphostin AG1478 (2.5 μM) for 14 days. At the experiment endpoint, using a subcellular protein fraction kit for cultured cells (ThermoFisher, 78840), cytosolic fraction was isolated according to the manufacturer's protocol. Briefly, VSMCs were harvested using 0.25% trypsin solution and resuspended in cytoplasmic extraction buffer. After 10 min incubation at 4°C, the samples were centrifuged at 1000×g for 5 min and the supernatants were collected as cytosolic fractions. The protein concentration for aortic tissue and VSMC fractions were quantified using a BCA assay and samples were prepared for protein immunoblotting.

### ***Gel Electrophoresis and Protein Immunoblotting***

VSMCs, osteoblasts, isolated EVs (either from cells or mouse aortas), and matrix vesicles (from osteoblasts) were lysed in RIPA lysis and extraction buffer supplemented with protease inhibitor. After adding Laemmli SDS-sample buffer (1:4 v/v, Boston BioProducts, BP-110R) to each lysate, the samples were denatured at 100°C for 10 min, loaded into 7.5-12% 1-mm SDS-PAGE gel (15 to 20 μg protein per lane), and run at 170 V. The proteins were then transferred to Trans-Blot turbo nitrocellulose membranes (BIO-RAD, 1704158) at 25 V for 7 min. To quantify the total protein, the membranes were stained using 2% w/v Ponceau stain (Alfa Aesar, AAJ6074409) for 20 min, followed by one wash with 5% acetic acid and milliQ water for 5 min. After imaging, the intensity of each lane was measured in ImageJ for total protein normalization. Membranes were blocked with 5% w/v bovine serum albumin (HyClone, SH30574.01) in TBS-Tween (1X) for 1 hour. The membranes were incubated with primary antibodies of interest, including CAV1 (1:200, Abcam, ab2910), TNAP (1:200, Invitrogen, 702454), EGFR (1:100, EMD Millipore, 06-874), CD63 (1:200, Abcam, ab231975), GAPDH (1:100, Abcam, ab181602), and Annexin V (1:200, proteintech, 11060-1-AP) overnight at 4°C. After three washes with TBS-Tween (1X), the membranes were

incubated with secondary antibody (1:1000, Li-Cor) for 1 hour, followed by three washes with TBS-Tween (1X). The protein bands were visualized with Odyssey CLx scanner (Li-Cor), and quantified using Image Studio Lite software (Li-Cor).

### ***Immunofluorescence Staining and Imaging***

VSMCs were fixed after 14 days of culture using formalin (10%) for 15 min and washed with PBS. A solution of PBS and Triton X (0.1% v/v) permeabilized the plasma membrane for 10 min at room temperature. To avoid non-specific antibody binding, the cells were incubated with a blocking buffer solution, consisting of BSA (1% w/v) and glycine (22.5 mg/mL) in PBS for 30 min at room temperature. Next, the cells were incubated for 2 hours with primary antibody against CAV1 (1:200) and washed three times with PBS. Cells were then incubated with a secondary antibody, Alexa Fluor 594 (1:500, Abcam, ab150080), for 1 hour at room temperature, followed by three washes with PBS. To visualize actin filaments, samples were incubated for 20 min with Phalloidin-iFluor 488 conjugate (1:50, Cayman Chemical, 20549) followed by three washes with PBS.

Resected mouse aortas were fixed in formalin (10%) for 2 hours. The tissues were rinsed with PBS and embedded in OCT. The samples were cryosectioned with a thickness of 7  $\mu$ m. The samples were incubated with a blocking buffer containing donkey serum (10% v/v), Triton X (0.3% v/v), and BSA (1% w/v) in PBS for 1 hour at room temperature. After blocking buffer removal, a solution of donkey serum (1% v/v), Triton X (0.3% v/v), BSA (1% w/v) in PBS, with primary antibody against either CAV1 (1:200), EGFR (1:100), or TNAP (1:200) was added to the samples. After an hour incubation at room temperature, the primary antibody solution was removed, and the samples were washed with PBS. Secondary antibody, Alexa Fluor 594 (1:500, Invitrogen, A21207) was added to the samples and incubated for 1 hour at room temperature. After washing the samples with PBS, they were stained with DAPI (0.2  $\mu$ g/mL, Cayman Chemical, 14285) for 10 min and washed with PBS. The samples were mounted using Fluoromount (Sigma Millipore, F4680). A confocal microscopy system (Eclipse Ti, Nikon) was used to image both cellular and tissue samples.

### ***X-ray Computed Tomography (X-ray CT)***

Femurs were dissected from mice, wrapped in parafilm and imaged directly in a Nikon XT H 225 scanner (macro-CT, Nikon Metrology, Tring, UK). The raw transmission images were reconstructed using commercial image reconstruction software package (CT Pro 3D, Nikon Metrology, Tring, UK), which employs a filtered back-projection algorithm. The scan was performed using 80 kV beam energy, 70  $\mu$ A beam current, and a power of 5.6 W. A PerkinElmer 1620 flat panel detector was used, with 200  $\mu$ m pixel size. The resulting effective pixel size was 5  $\mu$ m. The exposure time per projection was 0.5 s, and a total of 1601 projections were acquired, resulting in a scanning time of approximately 13 minutes per sample. Bone structural parameters, including thickness and volume fraction (the ratio of bone volume (BV) to total volume (TV)), for both cortical and trabecular regions were assessed using a plug-in module, BoneJ, in ImageJ (NIH, USA) [100].

### ***Statistics***

Data are presented as the mean of independent replications, and error bars represent the standard error of the mean. The reported  $n$  values represent independent biological replicates. Statistical significance between groups was calculated using one-way ANOVA with Tukey's post-hoc test in GraphPad Prism 8. A p-value less than 0.05 was considered statistically significant. In case of comparison between two groups, the statistical significance was calculated using t-test with p-values less than 0.05.

## **5.3. Results**

### ***Mendelian Randomization shows positive correlation between serum EGFR and CAC***

Of the 11 MR regressions performed in the MESA cohort, all regressions predicted positive correlation between serum EGFR concentration and CAC (i.e., elevated EGFR concentration

predicts increased incidence of elevated CAC). Two of the MR regressions reached statistical significance beyond the Bonferroni-adjusted significance threshold: robust MR-Egger and penalized robust MR-Egger. The intercept tests for the MR-Egger estimates are statistically significant at  $p = 1.9 \times 10^{-5}$ , suggesting the presence of vertical pleiotropy among the IV SNPs accounted for in the MR-Egger type regressions (**Fig. 14, A**). The causal estimates of the effect of EGFR concentration on increased CAC are associated with p-values of 0 (**Table 2**).

Table 2. Summary statistics of each MR regression in the MESA cohort. All statistically significant tests, including intercept tests for vertical pleiotropy, have their associated p-values highlighted in red.

Method	Estimate	Standard Error	95% CI lower	95% CI upper	p-value
Simple median	0.033	0.267	-0.49	0.556	0.9
Weighted median	0.093	0.244	-0.38	0.57	0.703
Penalized weighted median	0.093	0.244	-0.38	0.57	0.703
IVW	0.147	0.194	-0.23	0.53	0.446
Penalized IVW	0.147	0.194	-0.23	0.53	0.446
Robust IVW	0.144	0.126	-0.1	0.39	0.251
Penalized robust IVW	0.144	0.126	-0.1	0.39	0.251
MR-Egger	0.755	0.513	-0.23	1.78	0.131
Intercept	-0.101	0.076	-0.25	0.049	0.186
Penalized MR-Egger	0.775	0.513	-0.23	1.78	0.131
Intercept	-0.101	0.076	-0.25	0.049	0.186
Robust MR-Egger	0.775	0.074	0.63	0.92	0
Intercept	-0.101	0.024	-0.147	-0.05	0.000019
Penalized robust MR-Egger	0.775	0.074	0.63	0.92	0
Intercept	-0.101	0.024	-0.147	-0.05	0.000019

Replication of the 11 MR regressions in the FHS cohort also yielded significant estimates for the robust MR-Egger and penalized robust MR-Egger regression estimates with p-values of  $1.17 \times 10^{-6}$  for both. However, the intercept test for vertical pleiotropy was not statistically significant ( $p = 0.06$ ), possibly trending towards significance due to insufficient sample size. However, both regressions suggest a positive causal relation between serum EGFR concentration and CAC (**Table**

3). We subsequently explored the relationship between EGFR and vascular calcification via *in vivo* and *in vitro* models.

Table 3. Summary statistics of each MR regression in the Framingham Heart Study (FHS). All statistically significant tests, including intercept tests for vertical pleiotropy, have their associated p-values highlighted in red.

Method	Estimate	Standard Error	95% CI lower	95% CI upper	p-value
Simple median	0.164	0.422	-0.662	0.991	0.697
Weighted median	0.282	0.361	-0.426	0.991	0.435
Penalized weighted median	0.282	0.361	-0.426	0.991	0.435
IVW	0.235	0.312	-0.376	0.847	0.451
Penalized IVW	0.235	0.312	-0.376	0.847	0.451
Robust IVW	0.238	0.194	-0.141	0.617	0.219
Penalized robust IVW	0.238	0.194	-0.141	0.617	0.219
MR-Egger	0.688	0.723	-0.726	2.1	0.34
Intercept	-0.085	0.123	-0.323	0.154	0.487
Penalized MR-Egger	0.688	0.723	-0.726	2.1	0.34
Intercept	-0.085	0.123	-0.323	0.154	0.487
Robust MR-Egger	0.688	0.142	0.411	0.965	$1.17 \times 10^{-6}$
Intercept	-0.085	0.045	-0.173	0.0036	0.06
Penalized robust MR-Egger	0.688	0.142	0.411	0.965	$1.17 \times 10^{-6}$
Intercept	-0.085	0.045	-0.173	0.0036	0.06

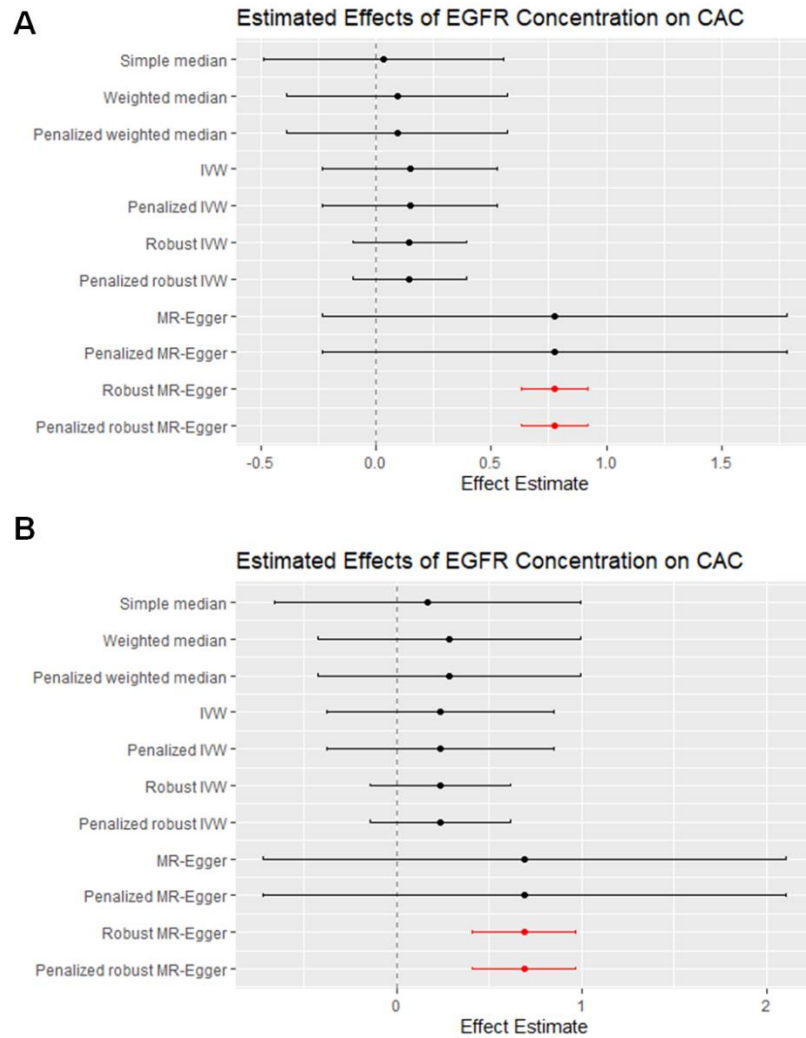


Figure 14. Serum EGFR positively correlates with coronary artery calcification. Forest plot summarizing effect estimates of each MR regression along with their 95% confidence intervals for: (A) MESA cohort; (B) Offspring cohort of FHS. Robust MR-Egger and penalized robust MR-Egger estimates of effect are statistically significant and highlighted in red.

### *EGFR inhibition reduces vascular calcification in a CKD mouse model*

Visualization of the calcium tracer, OsteoSense, showed widespread vascular calcification in CKD mice compared to the chow-fed control group. Daily EGFR inhibitor gavage (10 mg/kg/mouse) for two weeks dramatically reduced vascular calcification in CKD animals (**Fig. 15, A**). Quantification of the OsteoSense intensity revealed a significant reduction in vascular calcification in the EGFR inhibited group ( $p \leq 0.0001$ ), as shown in **Fig. 15, B**. The level of serum EGFR was elevated in the

CKD group compared to chow fed animals ( $p = 0.038$ ), with no significant difference between CKD and EGFR inhibited groups ( $p = 0.78$ ) (**Fig. 15, C**). Further, serum TNAP activity (**Fig. 15, D**) in CKD animals was significantly elevated compared to the control group ( $p = 0.003$ ). EGFR inhibition did not reduce serum TNAP activity ( $p = 0.06$ ). Gene expression of common renal fibrosis markers, *Tgfb1* and *Colla1* (**Fig. 15, E and F**), were significantly increased in both CKD mice ( $p = 0.02$  and  $p = 0.02$  for *Tgfb1* and *Colla1*, respectively) and CKD mice treated with EGFR inhibitor ( $p = 0.02$  and  $p = 0.03$  for *Tgfb1* and *Colla1*, respectively) when compared to chow-fed control, with no significant differences between the CKD groups ( $p = 0.7$  and  $p = 0.6$  for *Tgfb1* and *Colla1*, respectively). Qualitative assessment of histological sections of resected kidney tissues showed enlarged tubular structures in both CKD and EGFR inhibitor treated CKD groups, compared to the chow-fed control (**Fig. 15, G**). These results indicate that EGFR inhibition reduces vascular calcification in CKD animals independent of effects on renal injury.

#### ***EGFR inhibition attenuates in vitro vascular smooth muscle cell calcification***

VSMCs calcified following 28 days of culture in OS media, as shown by ARS staining (**Fig. 15, H**, representative image). Treatment of OS cultures with EGFR inhibitor abrogated *in vitro* calcification of the VSMCs (**Fig. 15, H**). Gene expression analysis of the common osteogenic markers, *RUNX2* and *ALPL*, revealed that VSMCs cultured in both OS ( $p = 0.02$  and  $p = 0.02$  for *RUNX2* and *ALPL*, respectively) and OS treated with EGFR inhibitor ( $p = 0.04$  and  $p = 0.03$  for *RUNX2* and *ALPL*, respectively) acquired an osteogenic phenotype after 14 days of culture (**Fig. 15, I and J**), with no significant differences between the groups ( $p = 0.4$  and  $p = 0.1$  for *RUNX2* and *ALPL*, respectively). Moreover, OS media promoted the accumulation of ECM collagen *in vitro*, which creates a platform for calcifying EVs to initiate calcification [5] (**Fig. 15, K**); EGFR inhibition did not affect the ECM collagen accumulation ( $p = 0.10$ ). These data indicate that EGFR inhibition attenuates VSMC calcification without affecting VSMC phenotypic changes.

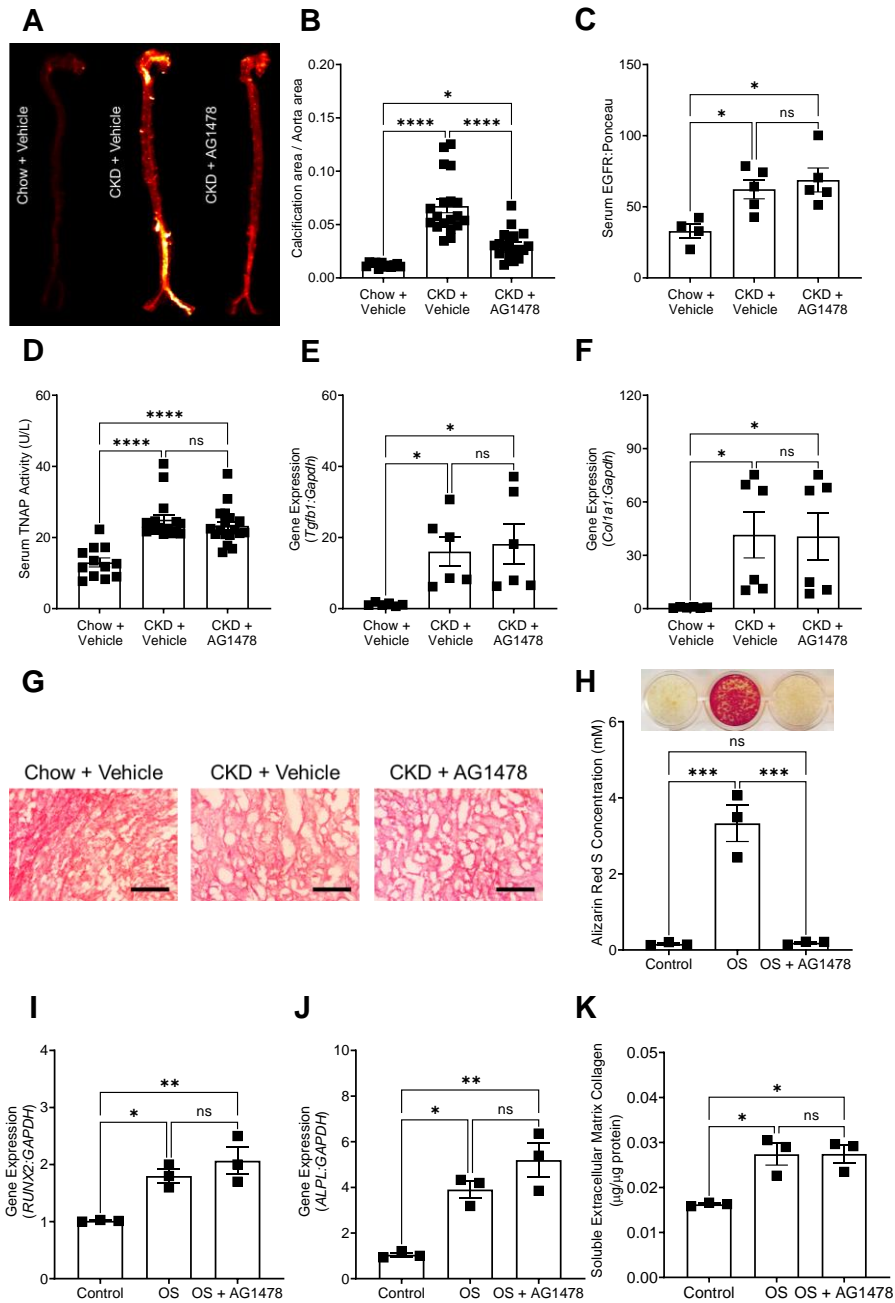


Figure 15. EGFR inhibition prevents vascular calcification *in vivo* and *in vitro*. (A) Visualization of vascular calcification using calcium tracer OsteoSense; (B) Quantification of the OsteoSense to correlate with vascular calcification burden; (C) Serum EGFR level collected from mouse groups; (D) Serum TNAP activity collected from mouse groups; (E and F) Gene expression of renal fibrotic markers, *Tgfb1* and *Colla1*; (G) H&E staining of mouse kidney tissues (20X, scale bar 0.5 mm); (H) *In vitro* calcification visualization using Alizarin Red S staining and quantification; (I and J) Gene expression of osteogenic markers, *RUNX2* and *ALPL* in VSMCs following 14 days of treatment; (K) Extracellular matrix collagen accumulation in VSMC cultures. \* $P < 0.05$ , \*\* $P \leq 0.01$ , \*\*\* $P \leq 0.001$ , and \*\*\*\* $P \leq 0.0001$ , ANOVA with Tukey's post-hoc test.

### ***EGFR inhibition alters CAV1/TNAP intracellular trafficking***

Both OS and OS cultured VSMCs treated with EGFR inhibitor significantly increased the total level of intracellular CAV1 in VSMCs compared to the control group ( $p < 0.0001$ ) (**Fig. 16, A**). OS media also increased intracellular EGFR in VSMCs compared to the control group ( $p = 0.019$ , **Fig. 16, B**). EGFR inhibition prevented the OS-induced increase in EGFR protein ( $p = 0.84$ ). Similar to the gene expression data (**Fig. 15, J**), both OS and OS cultured VSMCs treated with EGFR inhibitor exhibited elevated intracellular TNAP activity ( $p = 0.03$  and  $p = 0.03$  for intracellular CAV1 and TNAP activity, respectively, compared to control) (**Fig. 16, C**). Confocal micrographs of VSMCs (**Fig. 16, panel D**) showed alignment of CAV1 protein along actin filaments in VSMCs cultured in OS media. In the OS cultured VSMCs treated with EGFR inhibitor, larger clusters of CAV1 were observed between filaments. Subcellular protein fractionation of VSMCs revealed that both cytosolic CAV1 and TNAP were elevated in EGFR inhibited cultures compared to control ( $p = 0.02$  and  $p = 0.003$ , respectively) and OS groups ( $p = 0.04$  and  $p = 0.005$ , respectively, **Fig. 16, E and F**). Qualitative analysis of confocal micrographs of CAV1, EGFR, and TNAP immunofluorescence in the aorta of mice indicated elevation of all three proteins in CKD mice and CKD mice treated with EGFR inhibitor, compared to the chow-fed controls (**Fig. 17, panels A, C, and E**). Subcellular protein fractionation of aorta indicated higher cytosolic CAV1 and TNAP proteins in EGFR inhibited CKD animals compared to the CKD group ( $p = 0.04$  and  $p = 0.0001$ , and  $p = 0.018$ , respectively), similar to *in vitro* data (**Fig. 17, B, D, and F**).

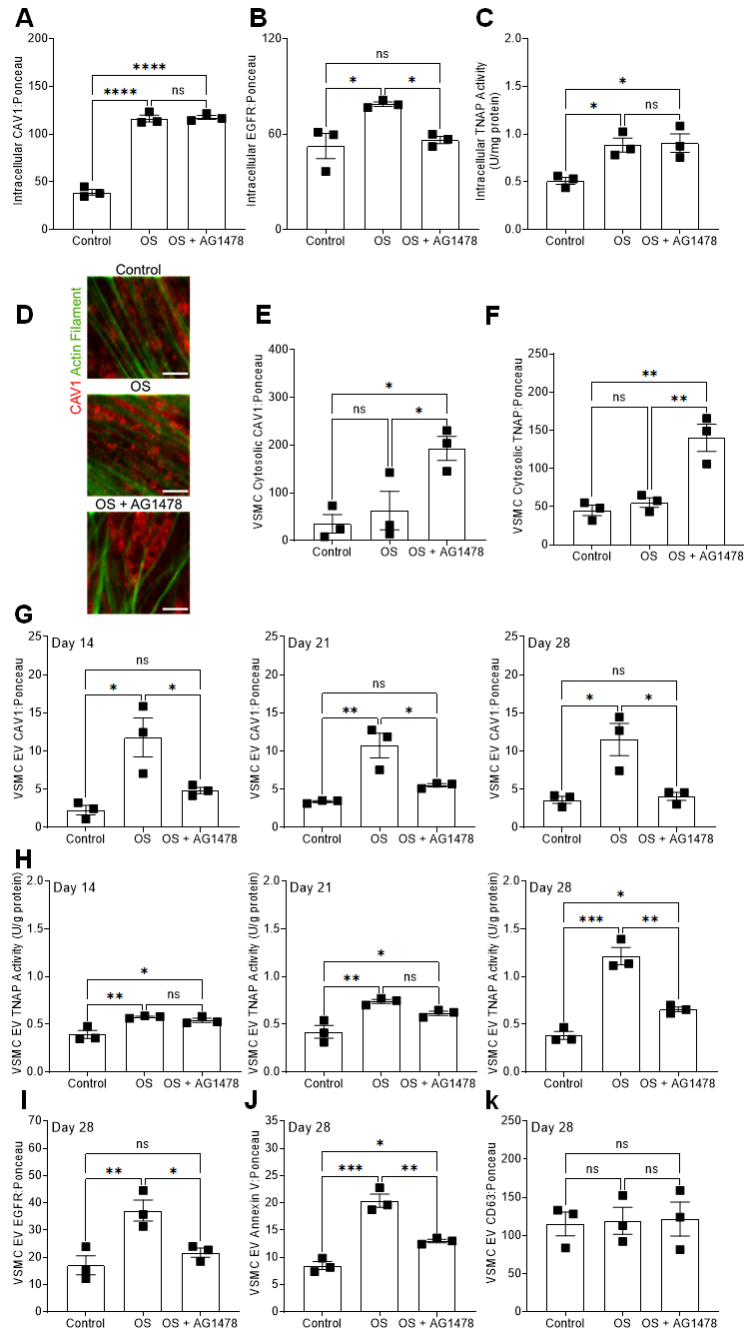


Figure 16. EGFR inhibition modulates CAV1 trafficking in VSMCs. Intracellular level of: (A) CAV1, (B) EGFR, and (C) TNAP activity in VSMCs after 14 days of culture; (D) Confocal micrographs of CAV1 distribution in VSMCs following 14 days of treatment (1200X, scale bar: 0.5 μm); Cytosolic level of: (E) CAV1, and (F) TNAP protein following 14 days of treatment; (G) CAV1 level on EVs isolated from VSMC cultures after 14, 21, and 28 days; (H) TNAP activity of the EVs isolated from VSMC cultures after 14, 21, and 28 days; EV level of: (I) EGFR, (J) Annexin V, and (K) CD63 liberated from VSMCs on day 28 of treatment. \*P < 0.05, \*\*P < 0.01, \*\*\*P < 0.001, and \*\*\*\*P < 0.0001, ANOVA with Tukey's post-hoc test.

***EGFR inhibition reduces the release of CAV1-positive EVs with high TNAP activity in vitro and in vivo***

EVs isolated from the aortas of CKD mice exhibited significantly elevated CAV1 protein and TNAP activity compared to chow-fed controls ( $p < 0.0001$  and  $p = 0.02$  for CAV1 and TNAP activity, respectively, **Fig. 17, G and H**). The EVs isolated from the CKD mice treated with EGFR inhibitor had significantly lower CAV1 protein and TNAP activity ( $p < 0.0001$  and  $p = 0.003$  for CAV1 and TNAP activity, respectively, **Fig. 17, G and H**). The EGFR inhibition led to similar outcomes *in vitro*. EVs obtained from VSMCs cultured in OS media contained significantly elevated CAV1 after 14, 21, and 28 days compared to controls (**Fig. 16, panel G**). EV TNAP activity increased in OS VSMC cultures over time (**Fig. 16, panel H**). EGFR inhibition reduced the release of CAV1-positive EVs by VSMCs (**Fig. 16, panel G**) and EV TNAP activity (**Fig. 16, panel H**). Furthermore, EVs isolated from VSMCs cultured in OS media were enriched with Annexin V, a calcium-binding protein, and EGFR (**Fig. 16, I and J**); EGFR inhibited groups showed reduced levels of Annexin V and EGFR on the EVs. Of note, the level of CD63, a common marker of the EVs, was preserved across the *in vitro* groups following 28 days of culture ( $p = 0.9$  between the groups), as shown in **Fig. 16, K**.

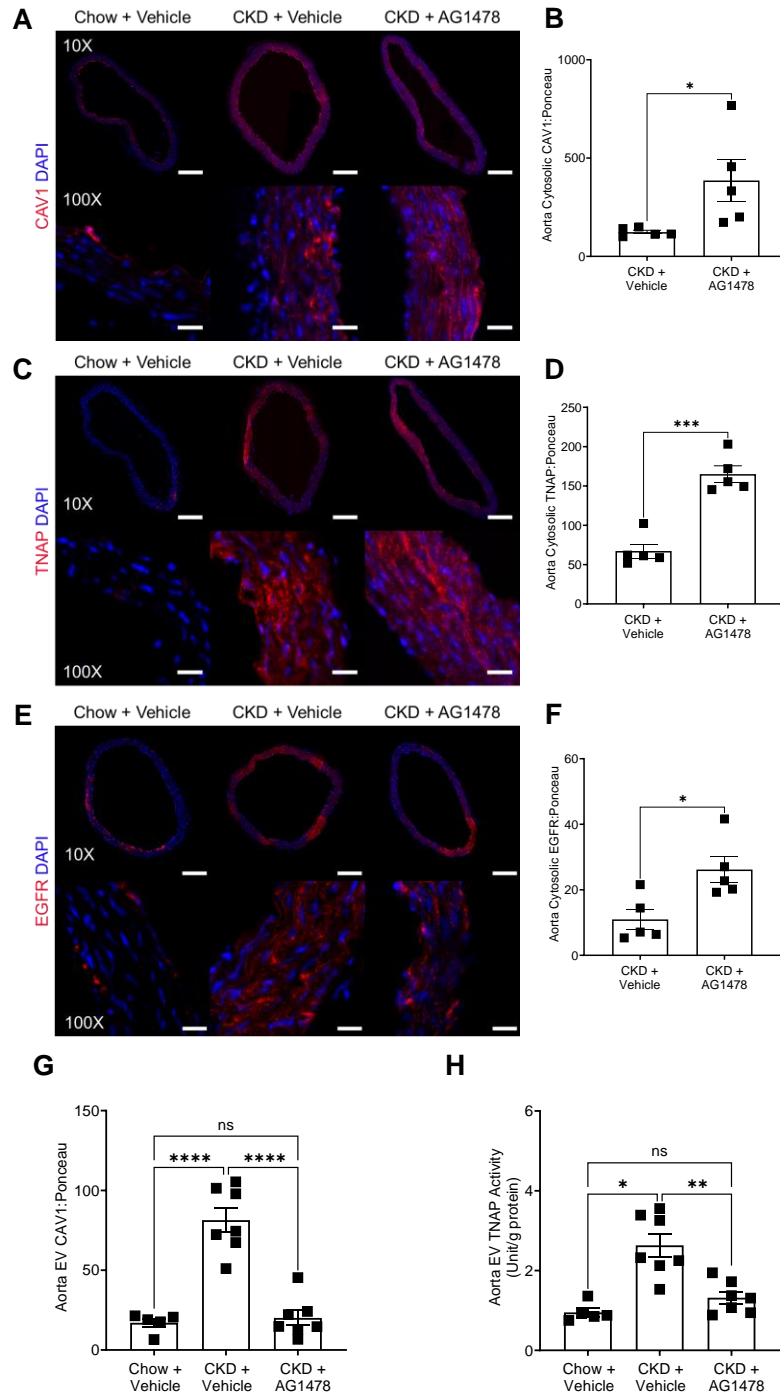


Figure 17. EGFR inhibition redistributes CAV1 and TNAP *in vivo*. (A) Immunofluorescence staining of CAV1 and (B) cytosolic level of CAV1 in aortic tissue; (C) Immunofluorescence staining of TNAP protein and (D) cytosolic level of TNAP protein in aortic tissue; (E) Immunofluorescence staining of EGFR and (F) cytosolic level of EGFR in aortic tissue; (G) Level of (G) CAV1 on EVs and (H) TNAP activity isolated from the mouse aortas. (scale bar for 10X and 100X, 200 and 20  $\mu$ m, respectively). \*P < 0.05, \*\*P  $\leq$  0.01, \*\*\*P  $\leq$  0.001, and \*\*\*\*P  $\leq$  0.0001, ANOVA with Tukey's post-hoc test.

### ***EGFR inhibition does not cause deleterious effects on physiological bone mineralization***

Both OS and OS cultured osteoblasts treated with EGFR inhibitor committed to osteogenic transition by downregulation of *RUNX2* [143, 144] (**Fig. 18, A**) and increased expression of *ALPL* and *Osteocalcin (BGLAP)* [143], after 7 days (**Fig. 18, B and C**), with no significant differences between the groups ( $p = 0.9$  and  $p = 0.9$  for *ALPL* and *BGLAP*, respectively). Like *ALPL* expression, the osteoblasts demonstrated significantly increased intracellular TNAP activity after 7 days in both cultures (**Fig. 18, D**). Alizarin red staining demonstrated *in vitro* calcification in both groups and quantification of the *in vitro* calcification showed no significant difference between the groups ( $p = 0.86$ , **Fig. 18, E**). In both OS and OS cultured osteoblasts treated with EGFR inhibitor, intracellular CAV1 protein was significantly increased compared to the control group ( $p = 0.02$  and  $p = 0.01$  for the OS and OS with EGFR inhibitor groups, respectively, **Fig. 18, F**). Matrix vesicles released by osteoblasts in both OS and OS treated with EGFR inhibitor groups had significantly increased TNAP activity; however, the EVs from these cells had lower levels of CAV1 protein compared to control on days 14 and 21 in culture (**Fig. 18, panel G and H**). We assessed the femurs resected from murine groups to analyze the effects of EGFR inhibition on bone mineralization (**Fig. 19, A to C**). The thickness and bone volume fraction of both trabecular (epiphyseal and metaphysical regions) and cortical bone was significantly reduced in CKD animals compared to chow-fed controls. EGFR inhibition increased the thickness of both trabecular and cortical bone significantly in the CKD mice ( $p = 0.04$  and  $p = 0.02$  for epiphyseal and metaphysical regions and  $p = 0.004$  for cortical bone) (**Fig. 19, D to F**). Interestingly, EGFR inhibition increased the bone volume fraction in trabecular bone, both epiphyseal ( $p = 0.009$ ) and metaphysical ( $p = 0.002$ ) regions, compared to CKD animals. However, it did not significantly change in cortical bone ( $p = 0.25$ ) (**Fig. 19, G to I**). Detailed quantification of the bone structural parameters can be found in **Table 4**.

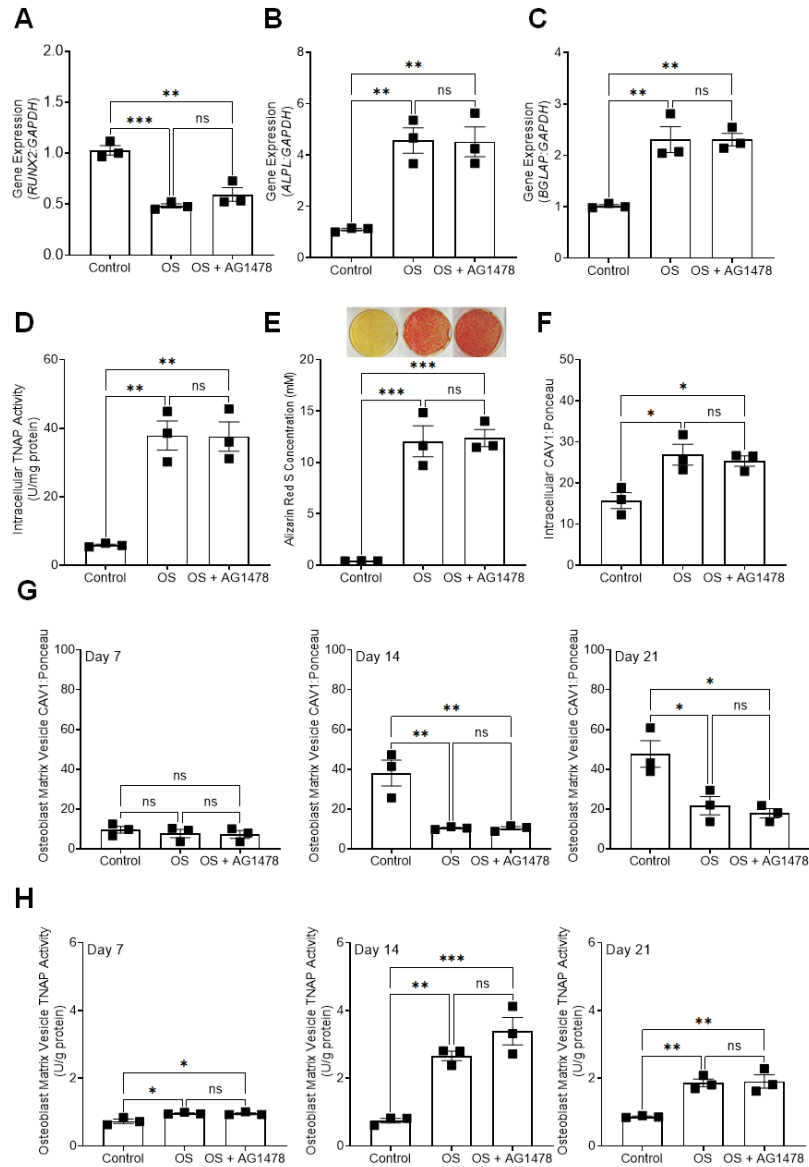


Figure 18. EGFR inhibition does not prevent osteoblast in vitro calcification. (A, B, and C) Gene expression of common osteogenic markers, RUNX2, ALPL, and BGLAP in osteoblasts following 7 days of treatment; (D) Osteoblast intracellular TNAP activity following 7 days of treatment; (E) Alizarin Red S staining and quantification of osteoblast cultures after 21 days; (F) Osteoblast intracellular CAV1 following 7 days of treatment; (G) CAV1 level on matrix vesicles liberated from osteoblasts on days 7, 14, and 21 of culture; (H) TNAP activity of matrix vesicles isolated from osteoblast cultures on days 7, 14, and 21. \* $P < 0.05$ , \*\* $P \leq 0.01$ , \*\*\* $P \leq 0.001$ , \*\*\*\* $P \leq 0.0001$ , ANOVA with Tukey's post-hoc test.

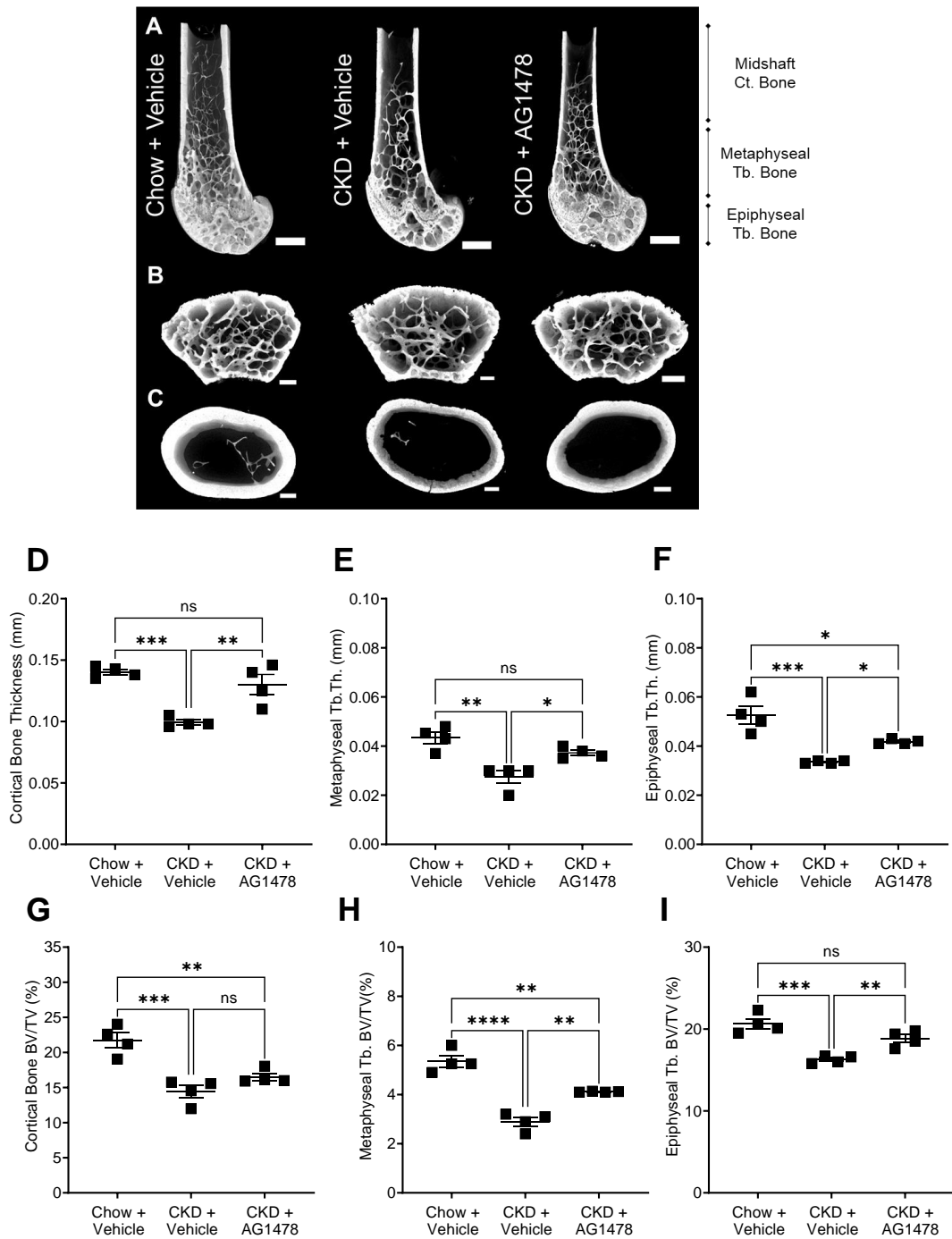


Figure 19. EGFR inhibition reverses deleterious effects on physiological bone mineralization. 3D reconstructions of (A) femoral head, (B) cancellous bone, and (C) cortical bone resected from mouse groups (scale bar: 0.5 mm); Bone thickness at: (D) Cortical, (E) Metaphyseal trabecular, and (F) Epiphyseal trabecular regions; Bone volume fraction (%) at: (G) Cortical, (H) Metaphyseal trabecular, and (I) Epiphyseal trabecular regions. \* $P < 0.05$ , \*\* $P \leq 0.01$ , \*\*\* $P \leq 0.001$ , and \*\*\*\* $P \leq 0.0001$ , ANOVA with Tukey's post-hoc test.

Table 4. Bone structural parameters for control, CKD, and EGFR-treated groups.

<b>Parameter</b>	<b>Chow + Vehicle n = 4</b>	<b>CKD + Vehicle n = 4</b>	<b>CKD + AG1478 n = 4</b>
<b>Distal femur</b>			
<i>Epiphyseal Trabecular Bone</i>			
BV/TV (%)	20.64±0.5	16.275±0.192	18.825±0.425
Tb.N (mm <sup>-1</sup> )	5.16±0.11	4.92±0.25	5±0.19685
Tb.Th (mm)	0.052±0.003	0.0335±0.0002	0.0417±0.0004
Tb.Sp (mm)	0.417±0.007	0.468±0.0106	0.450±0.0132
BS/BV (mm <sup>2</sup> /mm <sup>3</sup> )	65.32±5.52	87.77±11.896	81.82±5.7973
EF	0.0215±0.0009	0.0252±0.0012	0.0227±0.0006
EF <sub>max</sub>	0.876±0.007	0.8437±0.0082	0.8513±0.007
EF <sub>min</sub>	-0.805±0.008	-0.756±0.0175	-0.776±0.02
DA	1.462±0.030	1.263±0.0173	1.351±0.02
<i>Metaphyseal Trabecular Bone</i>			
BV/TV (%)	5.35±0.2	2.9±0.15	4.1±0.008
Tb.N (mm <sup>-1</sup> )	4.92±0.19	4.08±0.13	4.39±0.12
Tb.Th (mm)	0.043±0.002	0.027±0.002	0.037±0.001
Tb.Sp (mm)	0.408±0.02	0.472±0.013	0.44±0.017
BS/BV (mm <sup>2</sup> /mm <sup>3</sup> )	79.65±1.86	94.19±3.2	90.65±3.37
EF	0.086±0.004	0.117±0.006	0.098±0.004
EF <sub>max</sub>	0.86±0.008	0.73±0.05	0.81±0.004
EF <sub>min</sub>	-0.76±0.005	-0.565±0.056	-0.64±0.012
DA	2.1±0.084	1.44±0.005	1.66±0.054
<b>Femoral midshaft</b>			
<i>Cortical Bone</i>			
Mean Ct.Th (mm)	0.14±0.001	0.099±0.002	0.13±0.007
BV/TV (%)	21.72±0.73	14.46±0.75	16.51±0.44
Ps.Pm (mm)	4.935±0.08	4.36±0.02	4.63±0.02
Ec.Pm (mm)	3.730±0.06	3.70±0.07	3.66±0.01
J (mm <sup>4</sup> )	0.507±0.04	0.287±0.026	0.355±0.022

Data were collected using X-ray Computed Tomography of distal femur and femoral midshaft. Values represent the mean±SEM.

BV/TV= Bone Volume/Total Volume; Tb.N= Trabecular Number; Tb.Th= Trabecular Thickness; Tb.Sp= Trabecular Separation; BS/BV= Specific Bone Surface: Bone Surface Area/Bone Volume; EF= Ellipsoidal Factor; DA= Degree of Anisotropy; Ct.Th= Cortical Thickness; Ps.Pm= Periosteal Perimeter; Ec.Pm= Endocortical Perimeter; J= Polar Moment of Inertia.

#### 5.4. Discussion

CKD patients are prone to develop widespread vascular calcification, increasing from 25% of patients in stages 3 and 4 to 50-80% of the population in stage 5 [189]. Our data indicate that CKD-induced vascular calcification associates with increased serum EGFR in mice, like the association between circulating EGFR and CAC in the MR regression analyses. Osteogenic transition of VSMCs in the vessel wall and release of calcifying EVs orchestrate progression of vascular calcification [189]. These EVs share similarities with matrix vesicles released by osteoblasts and chondrocytes [162]. The plasma membrane protein, CAV1, plays a key role in formation of calcifying EVs and VSMC-mediated calcification. Knockdown of CAV1 led to prevention of VSMCs calcification *in vitro* [169]. EGFR co-localizes and interacts with CAV1 in caveolar domains of the plasma membrane. Previous studies showed that EGFR facilitates tyrosine kinase mediated phosphorylation of CAV1 and modulates CAV1 trafficking [190-193]. Therefore, we hypothesized that EGFR tyrosine kinase inhibition may prevent the CAV1-dependent formation of calcifying EVs in CKD.

Here, we show that inhibiting EGFR tyrosine kinase activity prevents vascular calcification in a CKD mouse model, with 100% survival rate. The *in vivo* results showed reduced calcium burden in the aorta of CKD mice treated with EGFR tyrosine kinase inhibitor, AG1478. This effect was independent of kidney remodeling as AG1478 treatment did not reduce the expression of common markers of renal injury. Furthermore, previous reports indicated the correlation between elevated serum TNAP activity and renal injury due to endothelial dysfunction and inflammation [194, 195]. High serum TNAP activity correlates with vascular calcification and dysfunctional bone turnover in CKD [196]. Indeed, TNAP facilitates the hydrolysis of a common calcification inhibitor, inorganic pyrophosphate, and mediates the calcification process [194, 197]. We showed similar elevated serum TNAP activity in both CKD mice and CKD mice treated with EGFR inhibitor,

demonstrating that EGFR inhibition prevented vascular calcification independent from serum TNAP activity and renal injury.

We hypothesized that EGFR inhibition would prevent calcification by altering CAV1 trafficking and disrupting the biogenesis of calcifying EVs. Our findings demonstrated elevated CAV1-positive EVs in the aorta of CKD mice, which was reduced by EGFR inhibition. Similarly, TNAP activity was elevated in EVs isolated from the aortae of CKD mice, while EGFR inhibition reduced the activity of this enzyme in the EVs. Calcifying EVs are enriched in Annexin V, a collagen-binding  $\text{Ca}^{2+}$  channel [62, 162]. We found that Annexin V was elevated in VSMC EVs, which was also reduced by EGFR inhibition. Taken together, these results support our hypothesis and suggest that targeting the CAV1-dependent formation of calcifying EVs by EGFR inhibition reduced vascular calcification in the CKD mouse model.

Since our data indicate that EGFR inhibition disrupts calcifying EV formation, we also set out to determine whether the treatment alters other types of EV formation. We began by blotting for CD63, a widely utilized marker enriched in exosomes and other EV subtypes, including high phosphate-induced VSMC calcification [198]. The data demonstrate no differences in CD63 protein within EVs from VSMCs cultured in control, OS, or OS media samples treated with AG1478. It is unclear whether calcifying EVs considered in our study derive from a CD63-positive population that is loaded with pro-calcific components, or whether they derive from a distinct population of EVs. Though these data do not show changes in CD63, it is possible that CD63-positive vesicles acquire pro-calcific properties in pathological conditions. The current data, however, suggest that CD63-positive EV release is not altered by EGFR inhibition.

Our *in-silico* data analyses of the MESA and Framingham cohorts ultimately led us to our *in vitro* results, which supported the *in vivo* findings that EGFR inhibition reduced the release of pro-calcific CAV1-positive EVs. This cardiinformatics workflow [199] highlights the importance of bridging not only the bench-to-bedside, also the informatics-to-medicine divide that still exists in modern precision cardiology research to enable computationally-derived therapeutics.

Interestingly, EGFR inhibition did not prevent osteogenic changes in the VSMCs cultures, suggesting that the effect was specific to calcifying EV biogenesis. In addition to increased gene expression of common osteogenic markers, VSMCs in OS media exhibited increased intracellular TNAP activity and CAV1 protein levels, even in the presence of the EGFR inhibitor. However, the EGFR inhibition prevented the release of active TNAP and CAV1 in calcifying EVs. Both *in vivo* and *in vitro* outcomes confirm EGFR inhibition increases cytosolic TNAP and CAV1 protein compared to other groups, indicating the role of EGFR in trafficking of these proteins. However, the precise intracellular trafficking mechanisms within VSMCs that result in TNAP activation, vesicle loading, and EV release remain unclear. These data suggest that EGFR inhibition blocks vesicle maturation somewhere between CAV1-dependent TNAP activation and EV release.

Our data also suggest that osteogenic function of osteoblasts was not affected by EGFR inhibition. Culturing osteoblasts in OS media resulted in the release of TNAP-positive EVs and robust mineralization, neither of which was altered by EGFR inhibition. Interestingly, we showed reduced CAV1 levels in matrix vesicles released by osteoblasts cultured in OS media. These observations further suggest that, despite many commonalities, bone matrix vesicles and vascular calcifying EVs originate through different mechanisms. CKD patients often exhibit bone disorders, including decreased bone mass density [200]. Previous reports demonstrated that trabecular and cortical bone mass density increased in CAV1-deficient mice [201, 202]. Here, we demonstrated that EGFR inhibition significantly reversed reductions in trabecular and cortical thickness in the CKD mice; bone volume fraction in trabecular regions significantly increased by the treatment, while cortical bone volume fraction was not improved. At the least, these results suggest that EGFR inhibition does not induce deleterious bone remodeling and—at best—may improve CKD-induced bone pathologies. The calcification paradox—the observation that bone and vascular mineral are often negatively correlated [203]—is poorly understood. Future studies that further explore the role of CAV1 and EGFR in calcification may provide new mechanistic insight into physiological and pathological mineralization differences.

## 5.5. Summary

Cardiovascular disease is the leading cause of death in patients with CKD, and the risk of mortality is directly associated with the presence of vascular calcification. Therefore, the development of a therapeutic strategy to prevent vascular mineralization in these patients would represent a breakthrough in CKD management. Other therapeutic strategies in promising clinical trials slow CKD-mediated vascular calcification by interacting directly with mineral [204]. Other proposed pre-clinical strategies include targeting mechanisms that lead to a pro-calcific SMC phenotype. However, a myriad of initiators results in vascular calcification. Our data suggest that EGFR inhibition does not alter SMC phenotype, but directly affects caveolin-1 trafficking. This provides a unique therapeutic strategy to modulate calcifying EV formation independent of cell phenotype. EGFR inhibitors have demonstrated clinical safety and efficacy in cancer treatments [205]. The accessibility of EGFR has led to the suggestion that it may represent a therapeutic target worth exploring for cardiovascular diseases [206]. CKD patients represent an identifiable population in need of therapeutics for vascular calcification. The confluence of an accessible target with approved therapeutics and a clear patient population that lack therapeutic options could accelerate the start of clinical trials.

## **Impact and Future Studies**

According to American Heart Association, cardiovascular diseases (CVDs), including coronary heart disease, heart failure, stroke, and hypertension, threaten 49.2% of adults (20 and older), and positively correlate with age [79]. Of note, cardiovascular calcification is the most significant predictor of cardiovascular events [11]. A National Heart, Lung, and Blood Institute report on the MESA cohort (comprising White, Black, Chinese, and Hispanic adults, mean age of 63) shows that the prevalence of coronary artery calcification is 70.4, 52.1, 65.2, and 59.2%, respectively, in males, and 44.6, 36.5, 34.9, and 41.9%, respectively, in females [79]. Calcification compromises the biomechanical integrity of cardiovascular tissues. Despite the vital role of cardiovascular calcification in morbidity and mortality, there is no known pharmaceutical to either reduce or prevent pathological calcification. In this study, first, we investigated the off-target effects of common anti-osteoporosis pharmaceuticals, bisphosphonates, on cardiovascular calcification. We showed that bisphosphonates can alter calcification burden and mineral morphology in the vasculature, both important factors in the association between calcification and cardiovascular morbidity. Next, we studied the cellular mechanism through which vascular calcification occurs and identified caveolin-1 dependent mechanisms that differentiate pathological cardiovascular calcification from physiological bone mineralization. Finally, we assessed the role of epidermal growth factor receptor (EGFR), a known caveolin-1 interactor, in vascular calcification in vitro and in vivo in a mouse model of chronic kidney disease. We showed that inhibition of EGFR prevents vascular calcification. Given the efficacy and safety of EGFR inhibition in other pathologies, it may represent an ideal target for future clinical trials to prevent vascular calcification.

## References

1. Goetsch, C., et al., *Sortilin mediates vascular calcification via its recruitment into extracellular vesicles*. The Journal of clinical investigation, 2016. 126(4): p. 1323.
2. Bakhshian Nik, A., J.D. Hutcheson, and E. Aikawa, *Extracellular vesicles as mediators of cardiovascular calcification*. Frontiers in cardiovascular medicine, 2017. 4: p. 78.
3. Hutcheson, J.D., et al. *Revisiting cardiovascular calcification: A multifaceted disease requiring a multidisciplinary approach*. in *Seminars in cell & developmental biology*. 2015. Elsevier.
4. Hutcheson, J.D., et al., *Genesis and growth of extracellular-vesicle-derived microcalcification in atherosclerotic plaques*. Nat Mater, 2016. 15(3): p. 335-43.
5. Hutcheson, J.D., et al., *Genesis and growth of extracellular-vesicle-derived microcalcification in atherosclerotic plaques*. Nature materials, 2016. 15(3): p. 335-343.
6. Persy, V. and P. D'Haese, *Vascular calcification and bone disease: the calcification paradox*. Trends in molecular medicine, 2009. 15(9): p. 405-416.
7. Elmariah, S., et al., *Bisphosphonate use and prevalence of valvular and vascular calcification in women: MESA (The Multi-Ethnic Study of Atherosclerosis)*. Journal of the American College of Cardiology, 2010. 56(21): p. 1752-1759.
8. Skolnick, A.H., et al., *Osteoporosis treatment and progression of aortic stenosis*. The American journal of cardiology, 2009. 104(1): p. 122-124.
9. Perkins, R.M., et al., *Bisphosphonates and Mortality in Women with CKD and the Presence or Absence of Cardiovascular Disease*. Clinical Journal of the American Society of Nephrology, 2014. 9(5): p. 874-880.
10. Persy, V. and P. D'Haese, *Vascular calcification and bone disease: the calcification paradox*. Trends Mol Med, 2009. 15(9): p. 405-16.
11. Hutcheson, J.D., M.C. Blaser, and E. Aikawa, *Giving Calcification Its Due: Recognition of a Diverse Disease*. Circulation research, 2017. 120(2): p. 270-273.
12. Ruiz, J.L., et al., *Zooming in on the genesis of atherosclerotic plaque microcalcifications*. The Journal of physiology, 2016. 594(11): p. 2915-2927.
13. Hsu, J.J., et al., *Cell-matrix mechanics and pattern formation in inflammatory cardiovascular calcification*. Heart, 2016. 102(21): p. 1710-1715.
14. Thompson, B. and D.A. Towler, *Arterial calcification and bone physiology: role of the bone-vascular axis*. Nature Reviews Endocrinology, 2012. 8(9): p. 529-543.
15. Reznikov, N., et al., *A materials science vision of extracellular matrix mineralization*. Nature Reviews Materials, 2016. 1: p. 16041.

16. Proudfoot, D. and C.M. Shanahan, *Biology of calcification in vascular cells: intima versus media*. Herz, 2001. 26(4): p. 245-251.
17. Lampropoulos, C.E., I. Papaioannou, and D.P. D'cruz, *Osteoporosis—a risk factor for cardiovascular disease?* Nature Reviews Rheumatology, 2012. 8(10): p. 587-598.
18. Shroff, R.C. and C.M. Shanahan. *Vascular calcification in patients with kidney disease: the vascular biology of calcification*. in *Seminars in dialysis*. 2007. Wiley Online Library.
19. Lusis, A.J., *Atherosclerosis*. Nature, 2000. 407(6801): p. 233-241.
20. Di Pietro, N., G. Formoso, and A. Pandolfi, *Physiology and pathophysiology of oxLDL uptake by vascular wall cells in atherosclerosis*. Vascular pharmacology, 2016. 84: p. 1-7.
21. London, G.M., et al., *Arterial media calcification in end-stage renal disease: impact on all-cause and cardiovascular mortality*. Nephrology Dialysis Transplantation, 2003. 18(9): p. 1731-1740.
22. Harper, E., et al., *Vascular calcification in type-2 diabetes and cardiovascular disease: Integrative roles for OPG, RANKL and TRAIL*. Vascular pharmacology, 2016. 82: p. 30-40.
23. Hutcheson, J.D., E. Aikawa, and W.D. Merryman, *Potential drug targets for calcific aortic valve disease*. Nature Reviews Cardiology, 2014. 11(4): p. 218-231.
24. Liu, A.C., V.R. Joag, and A.I. Gotlieb, *The emerging role of valve interstitial cell phenotypes in regulating heart valve pathobiology*. The American journal of pathology, 2007. 171(5): p. 1407-1418.
25. Galeone, A., et al., *Aortic valvular interstitial cells apoptosis and calcification are mediated by TNF-related apoptosis-inducing ligand*. International journal of cardiology, 2013. 169(4): p. 296-304.
26. Murshed, M., *Mechanism of bone mineralization*. Cold Spring Harbor perspectives in medicine, 2018. 8(12): p. a031229.
27. Bonucci, E., *Bone mineralization*. Front Biosci (Landmark Ed), 2012. 17: p. 100-28.
28. Iwayama, T., et al., *Osteoblastic lysosome plays a central role in mineralization*. Science advances, 2019. 5(7): p. eaax0672.
29. Bonucci, E., *Fine structure of early cartilage calcification*. Journal of ultrastructure research, 1967. 20(1-2): p. 33-50.
30. Anderson, H.C., *Vesicles associated with calcification in the matrix of epiphyseal cartilage*. The Journal of cell biology, 1969. 41(1): p. 59-72.
31. Schmidt, J.R., et al., *Osteoblast-released matrix vesicles, regulation of activity and composition by sulfated and non-sulfated glycosaminoglycans*. Molecular & Cellular Proteomics, 2016. 15(2): p. 558-572.

32. Aikawa, E., *Extracellular vesicles in cardiovascular disease: Focus on vascular calcification*. The Journal of physiology, 2016. 594(11): p. 2877-2880.
33. Shapiro, I.M., W.J. Landis, and M.V. Risbud, *Matrix vesicles: Are they anchored exosomes?* Bone, 2015. 79: p. 29-36.
34. Golub, E.E., *Role of matrix vesicles in biomineralization*. Biochimica et Biophysica Acta (BBA)-General Subjects, 2009. 1790(12): p. 1592-1598.
35. Cui, L., et al., *Characterisation of matrix vesicles in skeletal and soft tissue mineralisation*. Bone, 2016. 87: p. 147-158.
36. Kirsch, T., W. Wang, and D. Pfander, *Functional differences between growth plate apoptotic bodies and matrix vesicles*. Journal of Bone and Mineral Research, 2003. 18(10): p. 1872-1881.
37. New, S.E. and E. Aikawa, *Role of Extracellular Vesicles in De Novo Mineralization*. Arteriosclerosis, thrombosis, and vascular biology, 2013. 33(8): p. 1753-1758.
38. Anderson, H.C., *Matrix vesicles and calcification*. Current rheumatology reports, 2003. 5(3): p. 222-226.
39. Genetos, D.C., et al., *Impaired osteoblast differentiation in annexin A2-and-A5-deficient cells*. PloS one, 2014. 9(9): p. e107482.
40. Anderson, H.C., *Molecular biology of matrix vesicles*. Clinical orthopaedics and related research, 1995. 314: p. 266-280.
41. Lieben, L. and G. Carmeliet, *The delicate balance between vitamin D, calcium and bone homeostasis: lessons learned from intestinal-and osteocyte-specific VDR null mice*. The Journal of steroid biochemistry and molecular biology, 2013. 136: p. 102-106.
42. Anderson, H.C., et al., *Impaired calcification around matrix vesicles of growth plate and bone in alkaline phosphatase-deficient mice*. The American journal of pathology, 2004. 164(3): p. 841-847.
43. Genge, B.R., L.N. Wu, and R.E. Wuthier, *In vitro modeling of matrix vesicle nucleation synergistic stimulation of mineral formation by annexin A5 and phosphatidylserine*. Journal of Biological Chemistry, 2007. 282(36): p. 26035-26045.
44. Taraboletti, G., et al., *Shedding of the matrix metalloproteinases MMP-2, MMP-9, and MT1-MMP as membrane vesicle-associated components by endothelial cells*. The American journal of pathology, 2002. 160(2): p. 673-680.
45. D'Angelo, M., et al., *Authentic Matrix Vesicles Contain Active Metalloproteases (MMP) A ROLE FOR MATRIX VESICLE-ASSOCIATED MMP-13 IN ACTIVATION OF TRANSFORMING GROWTH FACTOR- $\beta$* . Journal of Biological Chemistry, 2001. 276(14): p. 11347-11353.
46. Kowal, J., et al., *Proteomic comparison defines novel markers to characterize heterogeneous populations of extracellular vesicle subtypes*. Proceedings of the National Academy of Sciences, 2016. 113(8): p. E968-E977.

47. Boulanger, C.M., et al., *Extracellular vesicles in coronary artery disease*. Nature Reviews Cardiology, 2017. 14(5): p. 259-272.
48. Cicero, A.L., P.D. Stahl, and G. Raposo, *Extracellular vesicles shuffling intercellular messages: for good or for bad*. Current opinion in cell biology, 2015. 35: p. 69-77.
49. Janas, T., et al., *Mechanisms of RNA loading into exosomes*. FEBS letters, 2015. 589(13): p. 1391-1398.
50. Nolte, E.N., et al., *Deep sequencing of RNA from immune cell-derived vesicles uncovers the selective incorporation of small non-coding RNA biotypes with potential regulatory functions*. Nucleic acids research, 2012: p. gks658.
51. Hergenreider, E., et al., *Atheroprotective communication between endothelial cells and smooth muscle cells through miRNAs*. Nature cell biology, 2012. 14(3): p. 249-256.
52. Krohn, J.B., et al., *Extracellular vesicles in cardiovascular calcification: expanding current paradigms*. The Journal of physiology, 2016.
53. Reynolds, J.L., et al., *Human vascular smooth muscle cells undergo vesicle-mediated calcification in response to changes in extracellular calcium and phosphate concentrations: a potential mechanism for accelerated vascular calcification in ESRD*. Journal of the American Society of Nephrology, 2004. 15(11): p. 2857-2867.
54. Shroff, R., D.A. Long, and C. Shanahan, *Mechanistic insights into vascular calcification in CKD*. Journal of the American Society of Nephrology, 2013. 24(2): p. 179-189.
55. Hutcheson, J.D., N. Maldonado, and E. Aikawa, *Small entities with large impact: microcalcifications and atherosclerotic plaque vulnerability*. Current opinion in lipidology, 2014. 25(5): p. 327-332.
56. Goetsch, C., J.D. Hutcheson, and E. Aikawa, *MicroRNA in Cardiovascular Calcification*. Circulation research, 2013. 112(7): p. 1073-1084.
57. Aikawa, E., et al., *Osteogenesis associates with inflammation in early-stage atherosclerosis evaluated by molecular imaging in vivo*. Circulation, 2007. 116(24): p. 2841-2850.
58. Tzaphlidou, M., *Bone architecture: collagen structure and calcium/phosphorus maps*. Journal of biological physics, 2008. 34(1): p. 39-49.
59. Kelly-Arnold, A., et al., *Revised microcalcification hypothesis for fibrous cap rupture in human coronary arteries*. Proceedings of the National Academy of Sciences, 2013. 110(26): p. 10741-10746.
60. Hutcheson, J.D., et al., *Enrichment of calcifying extracellular vesicles using density-based ultracentrifugation protocol*. Journal of extracellular vesicles, 2014. 3(1): p. 25129.
61. Osteikoetxea, X., et al., *Extracellular vesicles in cardiovascular disease: are they Jedi or Sith?* The Journal of physiology, 2016. 594(11): p. 2881-2894.

62. Chen, N.X., et al., *Annexin-mediated matrix vesicle calcification in vascular smooth muscle cells*. Journal of Bone and Mineral Research, 2008. 23(11): p. 1798-1805.
63. Goettsch, C., et al., *miR-125b regulates calcification of vascular smooth muscle cells*. The American journal of pathology, 2011. 179(4): p. 1594-1600.
64. Kapustin, A.N., et al., *Vascular smooth muscle cell calcification is mediated by regulated exosome secretion*. Circulation research, 2015: p. CIRCRESAHA. 114.305012.
65. Kapustin, A., et al., *Calcium regulates key components of vascular smooth muscle cell-derived matrix vesicles to enhance mineralization*. Circulation research, 2011: p. CIRCRESAHA. 110.238808.
66. Krohn, J.B., et al., *Discoidin domain receptor-1 regulates calcific extracellular vesicle release in vascular smooth muscle cell fibrocalcific response via transforming growth factor- $\beta$  signaling*. Arteriosclerosis, thrombosis, and vascular biology, 2016: p. ATVBAHA. 115.307009.
67. Ruiz, J.L., J.D. Hutcheson, and E. Aikawa, *Cardiovascular calcification: current controversies and novel concepts*. Cardiovascular Pathology, 2015. 24(4): p. 207-212.
68. Hjortnaes, J., et al., *Valvular interstitial cells suppress calcification of valvular endothelial cells*. Atherosclerosis, 2015. 242(1): p. 251-260.
69. Cui, L., et al., *End Stage Renal Disease-induced Hypercalcemia May Promote Aortic Valve Calcification via Annexin VI Enrichment of Valve Interstitial Cell Derived Matrix Vesicles*. Journal of Cellular Physiology, 2017.
70. Deguchi, J.-o., et al., *Chronic hypoxia activates the Akt and  $\beta$ -catenin pathways in human macrophages*. Arteriosclerosis, thrombosis, and vascular biology, 2009. 29(10): p. 1664-1670.
71. Hjortnaes, J., et al., *Arterial and aortic valve calcification inversely correlates with osteoporotic bone remodelling: a role for inflammation*. European heart journal, 2010. 31(16): p. 1975-1984.
72. Aikawa, M., et al., *An HMG-CoA reductase inhibitor, cerivastatin, suppresses growth of macrophages expressing matrix metalloproteinases and tissue factor in vivo and in vitro*. Circulation, 2001. 103(2): p. 276-283.
73. Deguchi, J.-o., et al., *Inflammation in Atherosclerosis. Visualizing Matrix Metalloproteinase Action in Macrophages In Vivo*, 2006. 114(1): p. 55-62.
74. Kapustin, A. and C.M. Shanahan, *Targeting vascular calcification: softening-up a hard target*. Current opinion in pharmacology, 2009. 9(2): p. 84-89.
75. New, S.E., et al., *Macrophage-derived matrix vesicles: an alternative novel mechanism for microcalcification in atherosclerotic plaques*. Circulation research, 2013: p. CIRCRESAHA. 113.301036.
76. Ruiz, J.L., et al., *Nanoanalytical analysis of bisphosphonate-driven alterations of microcalcifications using a 3D hydrogel system and in vivo mouse model*. Proceedings of the National Academy of Sciences, 2021. 118(14).

77. Bentzon, J.F., et al., *Mechanisms of plaque formation and rupture*. *Circulation research*, 2014. 114(12): p. 1852-1866.
78. Braun, M., et al., *Cellular adhesion molecules on vascular smooth muscle cells*. *Cardiovascular research*, 1999. 41(2): p. 395-401.
79. Virani, S.S., et al., *Heart disease and stroke statistics—2021 update: a report from the American Heart Association*. *Circulation*, 2021. 143(8): p. e254-e743.
80. Peng, A.W., et al., *Long-term all-cause and cause-specific mortality in asymptomatic patients with  $CAC \geq 1,000$ : results from the CAC Consortium*. *Cardiovascular Imaging*, 2020. 13(1\_Part\_1): p. 83-93.
81. Jin, H.-Y., et al., *The relationship between coronary calcification and the natural history of coronary artery disease*. *Cardiovascular Imaging*, 2021. 14(1): p. 233-242.
82. Libby, P., *Collagenases and cracks in the plaque*. *The Journal of clinical investigation*, 2013. 123(8): p. 3201-3203.
83. Maldonado, N., et al., *The explosive growth of small voids in vulnerable cap rupture; cavitation and interfacial debonding*. *Journal of biomechanics*, 2013. 46(2): p. 396-401.
84. Wang, Y., et al., *Imaging cardiovascular calcification*. *Journal of the American Heart Association*, 2018. 7(13): p. e008564.
85. Criqui, M.H., et al., *Calcium density of coronary artery plaque and risk of incident cardiovascular events*. *Jama*, 2014. 311(3): p. 271-278.
86. Recker, R.R., et al., *Safety of bisphosphonates in the treatment of osteoporosis*. *The American journal of medicine*, 2009. 122(2): p. S22-S32.
87. Neven, E.G., M.E. De Broe, and P.C. d'Haese, *Prevention of vascular calcification with bisphosphonates without affecting bone mineralization: a new challenge?* *Kidney international*, 2009. 75(6): p. 580-582.
88. Rodan, G.A. and H.A. Fleisch, *Bisphosphonates: mechanisms of action*. *The Journal of clinical investigation*, 1996. 97(12): p. 2692-2696.
89. Kirchmayer, U., et al., *Bisphosphonates and cardiovascular risk in elderly patients with previous cardiovascular disease: a population-based nested case-control study in Italy*. *Therapeutic advances in drug safety*, 2019. 10: p. 2042098619838138.
90. Wu, S.-T., J.-F. Chen, and C.-J. Tsai, *The impact of bisphosphonates on mortality and cardiovascular risk among osteoporosis patients after cardiovascular disease*. *Journal of the Formosan Medical Association*, 2021. 120(11): p. 1957-1966.
91. Ylitalo, R., et al., *Accumulation of bisphosphonates in the aorta and some other tissues of healthy and atherosclerotic rabbits*. *Journal of Laboratory and Clinical Medicine*, 1996. 127(2): p. 200-206.
92. Ylitalo, R., et al., *Accumulation of bisphosphonates in human artery and their effects on human and rat arterial function in vitro*. *Pharmacology & toxicology*, 1998. 83(3): p. 125-131.

93. Goettsch, C., H. Iwata, and E. Aikawa, *Parathyroid hormone: critical bridge between bone metabolism and cardiovascular disease*. 2014, Am Heart Assoc.
94. Tacey, A., et al., *Potential role for osteocalcin in the development of atherosclerosis and blood vessel disease*. *Nutrients*, 2018. 10(10): p. 1426.
95. Geng, Z., et al., *Short-term administration of the bisphosphonate ibandronate increases bone volume and prevents hyperparathyroid bone changes in mild experimental renal failure*. *Clinical nephrology*, 2000. 54(1): p. 45-53.
96. Lomashvili, K.A., et al., *Effect of bisphosphonates on vascular calcification and bone metabolism in experimental renal failure*. *Kidney international*, 2009. 75(6): p. 617-625.
97. Pirmohamed, M., *Commentary—bisphosphonates and calcium homeostasis*. *Postgraduate medical journal*, 2000. 76(897): p. 418-419.
98. MacAskill, M.G., et al., *Characterisation of an atherosclerotic micro-calcification model using ApoE<sup>-/-</sup> mice and PET/CT*. *International Journal of Cardiology. Heart & Vasculature*, 2020. 31.
99. Domander, R., A.A. Felder, and M. Doube, *BoneJ2-refactoring established research software*. Wellcome Open Research, 2021. 6.
100. Steiner, L., A. Synek, and D.H. Pahr, *Comparison of different microCT-based morphology assessment tools using human trabecular bone*. *Bone reports*, 2020. 12: p. 100261.
101. Rattazzi, M., et al., *Calcification of advanced atherosclerotic lesions in the innominate arteries of ApoE-deficient mice: potential role of chondrocyte-like cells*. *Arteriosclerosis, thrombosis, and vascular biology*, 2005. 25(7): p. 1420-1425.
102. Veseli, B.E., et al., *Animal models of atherosclerosis*. *European journal of pharmacology*, 2017. 816: p. 3-13.
103. Whitman, S.C., *A practical approach to using mice in atherosclerosis research*. *The Clinical Biochemist Reviews*, 2004. 25(1): p. 81.
104. Casula, M., et al., *Association between the cumulative exposure to bisphosphonates and hospitalization for atherosclerotic cardiovascular events: A population-based study*. *Atherosclerosis*, 2020. 301: p. 1-7.
105. Maldonado, N., et al., *A mechanistic analysis of the role of microcalcifications in atherosclerotic plaque stability: potential implications for plaque rupture*. *American Journal of Physiology-Heart and Circulatory Physiology*, 2012. 303(5): p. H619-H628.
106. Linder, C.H., et al., *Isozyme profile and tissue-origin of alkaline phosphatases in mouse serum*. *Bone*, 2013. 53(2): p. 399-408.
107. Mukaiyama, K., et al., *Elevation of serum alkaline phosphatase (ALP) level in postmenopausal women is caused by high bone turnover*. *Aging clinical and experimental research*, 2015. 27(4): p. 413-418.

108. Kovesdy, C.P., et al., *Outcome predictability of serum alkaline phosphatase in men with pre-dialysis CKD*. *Nephrology Dialysis Transplantation*, 2010. 25(9): p. 3003-3011.
109. Ploumis, A., et al., *Association between alendronate, serum alkaline phosphatase level, and heterotopic ossification in individuals with spinal cord injury*. *The journal of spinal cord medicine*, 2015. 38(2): p. 193-198.
110. Klein, B.Y., et al., *Structurally different bisphosphonates exert opposing effects on alkaline phosphatase and mineralization in marrow osteoprogenitors*. *Journal of cellular biochemistry*, 1998. 68(2): p. 186-194.
111. Guney, E., et al., *Effects of bisphosphonates on lipid metabolism*. *Neuroendocrinology Letters*, 2008. 29(2): p. 252-255.
112. Adami, S., et al., *Chronic intravenous aminobisphosphonate therapy increases high-density lipoprotein cholesterol and decreases low-density lipoprotein cholesterol*. *Journal of bone and mineral research*, 2000. 15(3): p. 599-604.
113. Whyte, M.P., et al., *Elevated serum lactate dehydrogenase isoenzymes and aspartate transaminase distinguish Albers-Schönberg disease (chloride channel 7 deficiency osteopetrosis) among the sclerosing bone disorders*. *Journal of Bone and Mineral Research*, 2010. 25(11): p. 2515-2526.
114. New, S.E., et al., *Macrophage-derived matrix vesicles: an alternative novel mechanism for microcalcification in atherosclerotic plaques*. *Circulation research*, 2013. 113(1): p. 72-77.
115. Rogers, M.A., M. Aikawa, and E. Aikawa, *Macrophage heterogeneity complicates reversal of calcification in cardiovascular tissues*. 2017, Am Heart Assoc.
116. Pablo Rodríguez, J., et al., *Cytoskeletal organization of human mesenchymal stem cells (MSC) changes during their osteogenic differentiation*. *Journal of cellular biochemistry*, 2004. 93(4): p. 721-731.
117. Wang, H.-L., et al., *Dexamethasone-induced cellular tension requires a SGK1-stimulated Sec5-GEF-H1 interaction*. *J Cell Sci*, 2015. 128(20): p. 3757-3768.
118. Zhang, Y., et al., *Mechanical strain-induced RhoA activation requires NADPH oxidase-mediated ROS generation in caveolae*. *Antioxidants & redox signaling*, 2010. 13(7): p. 959-973.
119. Schlörmann, W., et al., *The shape of caveolae is omega-like after glutaraldehyde fixation and cup-like after cryofixation*. *Histochemistry and cell biology*, 2010. 133(2): p. 223-228.
120. Qin, B., et al., *Activated Src and Ras induce gefitinib resistance by activation of signaling pathways downstream of epidermal growth factor receptor in human gallbladder adenocarcinoma cells*. *Cancer chemotherapy and pharmacology*, 2006. 58(5): p. 577-584.
121. Hsu, J.L. and M.-C. Hung, *The role of HER2, EGFR, and other receptor tyrosine kinases in breast cancer*. *Cancer and Metastasis Reviews*, 2016. 35(4): p. 575-588.

122. Bae, M.S., et al., *Mammographic features of calcifications in DCIS: correlation with oestrogen receptor and human epidermal growth factor receptor 2 status*. *European radiology*, 2013. 23(8): p. 2072-2078.
123. Holland, P.M. and J.A. Cooper, *Protein modification: docking sites for kinases*. *Current Biology*, 1999. 9(9): p. R329-R331.
124. Sverdlov, M., A.N. Shajahan, and R.D. Minshall, *Tyrosine phosphorylation-dependence of caveolae-mediated endocytosis*. *Journal of cellular and molecular medicine*, 2007. 11(6): p. 1239-1250.
125. Echarri, A., et al., *Caveolar domain organization and trafficking is regulated by Abl kinases and mDial*. *Journal of cell science*, 2012. 125(13): p. 3097-3113.
126. Zimnicka, A.M., et al., *Src-dependent phosphorylation of caveolin-1 Tyr-14 promotes swelling and release of caveolae*. *Molecular biology of the cell*, 2016. 27(13): p. 2090-2106.
127. Sverdlov, M., et al., *Filamin A regulates caveolae internalization and trafficking in endothelial cells*. *Molecular biology of the cell*, 2009. 20(21): p. 4531-4540.
128. Echarri, A. and M.A. Del Pozo, *Caveolae-mechanosensitive membrane invaginations linked to actin filaments*. *J Cell Sci*, 2015. 128(15): p. 2747-2758.
129. Hu, J., et al., *Opposing FlnA and FlnB interactions regulate RhoA activation in guiding dynamic actin stress fiber formation and cell spreading*. *Human molecular genetics*, 2017. 26(7): p. 1294-1304.
130. Lian, G., et al., *Cytoskeletal associated filamin A and RhoA affect neural progenitor specification during mitosis*. *Cerebral cortex*, 2019. 29(3): p. 1280-1290.
131. Nuno, D.W., S.K. England, and K.G. Lamping, *RhoA localization with caveolin-1 regulates vascular contractions to serotonin*. *American Journal of Physiology-Regulatory, Integrative and Comparative Physiology*, 2012. 303(9): p. R959-R967.
132. Dubroca, C., et al., *RhoA activation and interaction with Caveolin-1 are critical for pressure-induced myogenic tone in rat mesenteric resistance arteries*. *Cardiovascular research*, 2007. 73(1): p. 190-197.
133. Nguyen, L.K., B.N. Kholodenko, and A. Von Kriegsheim, *Rac1 and RhoA: Networks, loops and bistability*. *Small GTPases*, 2018. 9(4): p. 316-321.
134. Kunschmann, T., et al., *The small GTPase Rac1 increases cell surface stiffness and enhances 3D migration into extracellular matrices*. *Scientific reports*, 2019. 9(1): p. 1-18.
135. Zuo, L., et al., *Caveolin-1 is essential for activation of Rac1 and NAD(P)H oxidase after angiotensin II type 1 receptor stimulation in vascular smooth muscle cells: role in redox signaling and vascular hypertrophy*. *Arteriosclerosis, thrombosis, and vascular biology*, 2005. 25(9): p. 1824-1830.
136. Goettsch, C., et al., *miR-125b regulates calcification of vascular smooth muscle cells*. *Am. J. Pathol.*, 2011. 179(4): p. 1594-1600.

137. Bandaru, S., et al., *Filamin A Regulates Cardiovascular Remodeling*. International Journal of Molecular Sciences, 2021. 22(12): p. 6555.
138. Wang, T., et al., *Rho-kinase inhibitor Y-27632 facilitates the proliferation, migration and pluripotency of human periodontal ligament stem cells*. Journal of cellular and molecular medicine, 2017. 21(11): p. 3100-3112.
139. Tian, B. and P.L. Kaufman, *Comparisons of actin filament disruptors and Rho kinase inhibitors as potential antiglaucoma medications*. Expert review of ophthalmology, 2012. 7(2): p. 177-187.
140. Rodal, S.K., et al., *Extraction of cholesterol with methyl- $\beta$ -cyclodextrin perturbs formation of clathrin-coated endocytic vesicles*. Molecular biology of the cell, 1999. 10(4): p. 961-974.
141. Mundhara, N., A. Majumder, and D. Panda, *Methyl- $\beta$ -cyclodextrin, an actin depolymerizer augments the antiproliferative potential of microtubule-targeting agents*. Scientific reports, 2019. 9(1): p. 1-12.
142. Graziani, A., et al., *Cholesterol and caveolin-rich membrane domains are essential for phospholipase A2-dependent EDHF formation*. Cardiovascular research, 2004. 64(2): p. 234-242.
143. Rutkovskiy, A., K.-O. Stenslkken, and I.J. Vaage, *Osteoblast differentiation at a glance*. Med. Sci. Monit. Basic Res., 2016. 22: p. 95.
144. Komori, T., *Regulation of bone development and extracellular matrix protein genes by RUNX2*. Cell and tissue research, 2010. 339(1): p. 189-195.
145. Insel, P.A. and H.H. Patel, *Membrane rafts and caveolae in cardiovascular signaling*. Current opinion in nephrology and hypertension, 2009. 18(1): p. 50.
146. Negi, P., R.S. Cheke, and V.M. Patil, *Recent advances in pharmacological diversification of Src family kinase inhibitors*. Egyptian Journal of Medical Human Genetics, 2021. 22(1): p. 1-16.
147. Rivera-Torres, J. and E. San Jos, *Src tyrosine kinase inhibitors: new perspectives on their immune, antiviral, and senotherapeutic potential*. Frontiers in pharmacology, 2019. 10: p. 1011.
148. Bedolla, R.G., et al., *Nuclear versus cytoplasmic localization of filamin A in prostate cancer: immunohistochemical correlation with metastases*. Clinical Cancer Research, 2009. 15(3): p. 788-796.
149. Andersen, J.N., et al., *Pathway-based identification of biomarkers for targeted therapeutics: personalized oncology with PI3K pathway inhibitors*. Science translational medicine, 2010. 2(43): p. 43ra55-43ra55.
150. Zhang, L., et al., *Filamin A inhibition reduces seizure activity in a mouse model of focal cortical malformations*. Science translational medicine, 2020. 12(531).
151. Tang, D.D., *Critical role of actin-associated proteins in smooth muscle contraction, cell proliferation, airway hyperresponsiveness and airway remodeling*. Respiratory research, 2015. 16(1): p. 1-14.

152. Ng, H.H., et al., *Cellular Contraction is Required for Hyperglycemia-Induced Vascular Calcification*. *Circulation*, 2019. 140(Suppl\_1): p. A16072-A16072.
153. Honjo, M., et al., *Effects of rho-associated protein kinase inhibitor Y-27632 on intraocular pressure and outflow facility*. *Investigative ophthalmology & visual science*, 2001. 42(1): p. 137-144.
154. Chevrier, V., et al., *The Rho-associated protein kinase p160ROCK is required for centrosome positioning*. *The Journal of cell biology*, 2002. 157(5): p. 807-817.
155. Fujisawa, K., et al., *Identification of the Rho-binding domain of p160ROCK, a Rho-associated coiled-coil containing protein kinase*. *Journal of Biological Chemistry*, 1996. 271(38): p. 23022-23028.
156. Uehata, M., et al., *Calcium sensitization of smooth muscle mediated by a Rho-associated protein kinase in hypertension*. *Nature*, 1997. 389(6654): p. 990-994.
157. Kovac, B., et al., *Assembly of non-contractile dorsal stress fibers requires  $\alpha$ -actinin-1 and Rac1 in migrating and spreading cells*. *Journal of cell science*, 2013. 126(1): p. 263-273.
158. Fisher, J.L. and S.S. Margulies, *Modeling the effect of stretch and plasma membrane tension on  $Na^+$ - $K^+$ -ATPase activity in alveolar epithelial cells*. *American Journal of Physiology-Lung Cellular and Molecular Physiology*, 2007. 292(1): p. L40-L53.
159. Bakhshian Nik, A., et al., *Epidermal Growth Factor Receptor Inhibition Prevents Caveolin-1-dependent Calcifying Extracellular Vesicle Biogenesis*. 2021, bioRxiv.
160. Ho, C.Y. and C.M. Shanahan, *Medial arterial calcification: an overlooked player in peripheral arterial disease*. *Arterioscler. Thromb. Vasc. Biol.*, 2016. 36(8): p. 1475-1482.
161. Marinelli, A., et al., *Diagnosis of arterial media calcification in chronic kidney disease*. *Cardiorenal Med.*, 2013. 3(2): p. 89-95.
162. Bakhshian Nik, A., J.D. Hutcheson, and E. Aikawa, *Extracellular vesicles as mediators of cardiovascular calcification*. *Front. cardiovasc. med.*, 2017. 4: p. (78)1-12.
163. Manzoor, S., et al., *Progression of medial arterial calcification in CKD*. *Kidney Int. Rep.*, 2018. 3(6): p. 1328-1335.
164. London, G.M., et al., *Arterial media calcification in end-stage renal disease: impact on all-cause and cardiovascular mortality*. *Nephrol. Dial. Transplant.*, 2003. 18(9): p. 1731-40.
165. Moe, S.M. and N.X. Chen, *Mechanisms of vascular calcification in chronic kidney disease*. *J. Am. Soc. Nephrol.*, 2008. 19(2): p. 213-216.
166. Ruiz, J.L., J.D. Hutcheson, and E. Aikawa, *Cardiovascular calcification: current controversies and novel concepts*. *Cardiovasc. Pathol.*, 2015. 24(4): p. 207-212.
167. New, S.E. and E. Aikawa, *Role of extracellular vesicles in de novo mineralization: an additional novel mechanism of cardiovascular calcification*. *Arterioscler. Thromb. Vasc. Biol.*, 2013. 33(8): p. 1753-1758.

168. Aikawa, E. and J.D. Hutcheson, *Cardiovascular Calcification and Bone Mineralization*. 2020: Springer.
169. Goettsch, C., et al., *Sortilin mediates vascular calcification via its recruitment into extracellular vesicles*. *J. Clin. Investig.*, 2016. 126(4): p. 1323-1336.
170. Hardin, C.D. and J. Vallejo, *Caveolins in vascular smooth muscle: form organizing function*. *Cardiovasc. Res.*, 2006. 69(4): p. 808-815.
171. Gratton, J.-P., P. Bernatchez, and W.C. Sessa, *Caveolae and caveolins in the cardiovascular system*. *Circ. Res.*, 2004. 94(11): p. 1408-1417.
172. Liu, P., M. Rudick, and R.G. Anderson, *Multiple functions of caveolin-1*. *J. Biol. Chem.*, 2002. 277(44): p. 41295-41298.
173. Wieduwilt, M. and M. Moasser, *The epidermal growth factor receptor family: biology driving targeted therapeutics*. *Cell. Mol. Life Sci.*, 2008. 65(10): p. 1566-1584.
174. Zhang, Y., et al., *Mechanical strain-induced RhoA activation requires NADPH oxidase-mediated ROS generation in caveolae*. *Antioxid. Redox Signal*, 2010. 13(7): p. 959-973.
175. Zhang, B., et al., *Caveolin-1 phosphorylation is required for stretch-induced EGFR and Akt activation in mesangial cells*. *Cell. Signal.*, 2007. 19(8): p. 1690-1700.
176. Wykosky, J., et al., *Therapeutic targeting of epidermal growth factor receptor in human cancer: successes and limitations*. *Chin. J. Cancer*, 2011. 30(1): p. 5.
177. Liang, Y.N., et al., *Combined caveolin-1 and epidermal growth factor receptor expression as a prognostic marker for breast cancer*. *Oncol. Lett.*, 2018. 15(6): p. 9271-9282.
178. Shin, S.U., et al., *Gene expression profiling of calcifications in breast cancer*. *Sci. Rep.*, 2017. 7(1): p. 1-11.
179. Wang, L., et al., *Inhibition of epidermal growth factor receptor attenuates atherosclerosis via decreasing inflammation and oxidative stress*. *Sci. Rep.*, 2017. 7(1): p. 1-14.
180. Burgess, S., et al., *Guidelines for performing Mendelian randomization investigations*. Wellcome Open Research, 2019. 4.
181. Sun, B.B., et al., *Genomic atlas of the human plasma proteome*. *Nature*, 2018. 558(7708): p. 73-79.
182. Yavorska, O.O. and S. Burgess, *MendelianRandomization: an R package for performing Mendelian randomization analyses using summarized data*. *International journal of epidemiology*, 2017. 46(6): p. 1734-1739.
183. RCoreTeam, *R: A language and environment for statistical computing*. 2021, R Foundation for Statistical Computing, Vienna, Austria.
184. Tani, T., et al., *Development of a novel chronic kidney disease mouse model to evaluate the progression of hyperphosphatemia and associated mineral bone disease*. *Sci. Rep.*, 2017. 7(1): p. 1-12.

185. Chen, N.X., et al., *Transglutaminase 2 accelerates vascular calcification in chronic kidney disease*. Am. J. Nephrol, 2013. 37(3): p. 191-198.
186. Ng, H.H., et al., *Increased superoxide production and altered nitric oxide-mediated relaxation in the aorta of young but not old male relaxin-deficient mice*. AM J PHYSIOL-HEART C, 2015. 309(2): p. H285-H296.
187. Ng, H.H., C.H. Leo, and L.J. Parry, *Serelaxin (recombinant human relaxin-2) prevents high glucose-induced endothelial dysfunction by ameliorating prostacyclin production in the mouse aorta*. Pharmacol. Res., 2016. 107: p. 220-228.
188. Ng, H.H., et al., *Serelaxin treatment reverses vascular dysfunction and left ventricular hypertrophy in a mouse model of Type 1 diabetes*. Sci. Rep., 2017. 7(1): p. 1-15.
189. Dusso, A., M.I. Colombo, and C.M. Shanahan, *Not all vascular smooth muscle cell exosomes calcify equally in chronic kidney disease*. Kidney Int., 2018. 93(2): p. 298-301.
190. Kim, Y.-N., et al., *Epidermal growth factor-stimulated tyrosine phosphorylation of caveolin-1: enhanced caveolin-1 tyrosine phosphorylation following aberrant epidermal growth factor receptor status*. J. Biol. Chem, 2000. 275(11): p. 7481-7491.
191. Abulrob, A., et al., *Interactions of EGFR and caveolin-1 in human glioblastoma cells: evidence that tyrosine phosphorylation regulates EGFR association with caveolae*. Oncogene, 2004. 23(41): p. 6967-6979.
192. Dittmann, K., et al., *Radiation-induced caveolin-1 associated EGFR internalization is linked with nuclear EGFR transport and activation of DNA-PK*. Molecular cancer, 2008. 7(1): p. 1-9.
193. Wang, Y., et al., *Hypoxia promotes ligand-independent EGF receptor signaling via hypoxia-inducible factor-mediated upregulation of caveolin-1*. Proceedings of the National Academy of Sciences, 2012. 109(13): p. 4892-4897.
194. Sciacqua, A., et al., *Alkaline phosphatase affects renal function in never-treated hypertensive patients: effect modification by age*. Sci. Rep., 2020. 10(1): p. 1-7.
195. Perticone, F., et al., *Serum alkaline phosphatase negatively affects endothelium-dependent vasodilation in naive hypertensive patients*. Hypertension, 2015. 66(4): p. 874-880.
196. Taliercio, J.J., et al., *Prognostic importance of serum alkaline phosphatase in CKD stages 3-4 in a clinical population*. American journal of kidney diseases, 2013. 62(4): p. 703-710.
197. Schoppet, M. and C. Shanahan, *Role for alkaline phosphatase as an inducer of vascular calcification in renal failure?* Kidney Int., 2008. 73(9): p. 989-991.
198. Kapustin, A.N., et al., *Vascular smooth muscle cell calcification is mediated by regulated exosome secretion*. Circ. Res., 2015. 116(8): p. 1312-1323.
199. Khomtchouk, B.B., et al., *Cardioinformatics: the nexus of bioinformatics and precision cardiology*. Briefings in bioinformatics, 2020. 21(6): p. 2031-2051.

200. Pan, B.-L. and S.-S. Loke, *Chronic kidney disease associated with decreased bone mineral density, uric acid and metabolic syndrome*. PloS one, 2018. 13(1): p. e0190985.
201. Rubin, J., et al., *Caveolin-1 knockout mice have increased bone size and stiffness*. Journal of Bone and Mineral Research, 2007. 22(9): p. 1408-1418.
202. Lee, Y.D., et al., *Caveolin-1 regulates osteoclastogenesis and bone metabolism in a sex-dependent manner*. J. Biol. Chem, 2015. 290(10): p. 6522-6530.
203. Persy, V. and P. D'Haese, *Vascular calcification and bone disease: the calcification paradox*. Trends. Mol. Med., 2009. 15(9): p. 405-416.
204. Raggi, P., et al., *Slowing Progression of Cardiovascular Calcification With SNF472 in Patients on Hemodialysis: Results of a Randomized Phase 2b Study*. Circulation, 2020. 141(9): p. 728-739.
205. Seshacharyulu, P., et al., *Targeting the EGFR signaling pathway in cancer therapy*. Expert Opin. Ther. Targets, 2012. 16(1): p. 15-31.
206. Mindur, J.E. and F.K. Swirski, *Growth factors as immunotherapeutic targets in cardiovascular disease*. Arterioscler. Thromb. Vasc. Biol., 2019. 39(7): p. 1275-1287.

## Appendices

### *Appendix I*

MATLAB script used for analysis the OsteoSense signal along the aorta.

```
clear all

cd('C:\FILE ADDRESS');
File_dir = ('RAW SCANNED IMAGE');
FileList = dir(strcat(File_dir, '*.tif'));
FileNames = {FileList.name};
FileNumber = length(FileNames);

for i = 1:FileNumber

    Image_name = num2str(FileNames{i});
    Fraction_Positive_Matrix{i,1} = Image_name;
    Mean_Intensity_Matrix{i,1} = Image_name;
    Image_string = strcat(File_dir, Image_name);
    Image = b fopen(Image_string);
    Image = Image{1,1};
    Image = Image{1,1};
    Image = uint16(Image)*80;
    Image(Image(:)==65535)=0;
    figure, imshow(Image)
    title(Image_name);
    colormap('hot')
    prompt = 'How many specimens are in this image? ';
    n = input(prompt);

    for k = 1:n

        figure, BW = roipoly(Image);
        Calc_image = imbinarize(Image,0.3);
        Total_image = imbinarize(Image,0.05);
        Calc_image = Calc_image.*BW;
        Total_image = Total_image.*BW;
        figure, imshow(Calc_image)
        figure, imshow(Total_image)
        Calcification_area = sum(sum(Calc_image));
        Total_area = sum(sum(Total_image));
        Percent_positive = Calcification_area/Total_area;
        Fraction_Positive_Matrix{i,k+1} = Percent_positive;
        Double_image = double(Image);
        Masked_image = Total_image.*Double_image;
        Mean_Intensity_Matrix{i,k+1} =
mean(mean(Masked_image))/Total_area;

    end

end
```

## *Appendix II*

The MATLAB script to analyze the total, mean, and maximum calcification in aortic roots.

Clear all

```
Image_dir = 'C:\FILE ADDRESS';
file_type = '*.nd2';
filelist = dir(strcat(Image_dir,file_type));
Number_of_Images = length(filelist);
kk=0;

for ii = 1:2:Number_of_Images

    image = b fopen(strcat(Image_dir, filelist(ii,1).name));

    image = image(1,1);
    image = image{1,1};
    image = image{1,1};
    image = image*8;

    image_smoothed = imgaussfilt(image,1);

    bw = imbinarize(image_smoothed,0.4);

    components = bwconncomp(bw);
    stats = regionprops(components, 'basic');

    Calcification_areas{ii-kk,1} = filelist(ii,1).name;

    Calcification_areas{ii-kk,2} = stats(:,1);

    kk = kk +1;

end
```

The MATLAB script to extract data from the analyzed images.

```
clear,clc,close all
%% Load in data
load FileName.mat
%% Parse data
data_to_parse=Calcification_areas(:,2);
n = numel(data_to_parse);
for ii = 1:n
    temp = cell2mat(data_to_parse(ii));
    temp = struct2table(temp);
    temp = table2array(temp);
    if isempty(temp)
        Calc(ii,1) = 0;
        Calc(ii,2) = 0;
        Calc(ii,3) = 0;
    else
        Areas = temp(:,1);
        Calc(ii,1) = (1/1.59^2)*mean(Areas,'all');
        Calc(ii,2) = (1/1.59^2)*max(Areas);
        Calc(ii,3) = (1/1.59^2)*sum(Areas,'all');
    end
end
end
```

### Appendix III

```
cd('C:\FILE ADDRESS');
File_dir = ('RAW SCANNED IMAGE');
FileList = dir(strcat(File_dir, '*.tif'));
FileNames = {FileList.name};
FileNumber = length(FileNames);

for i = 1:FileNumber

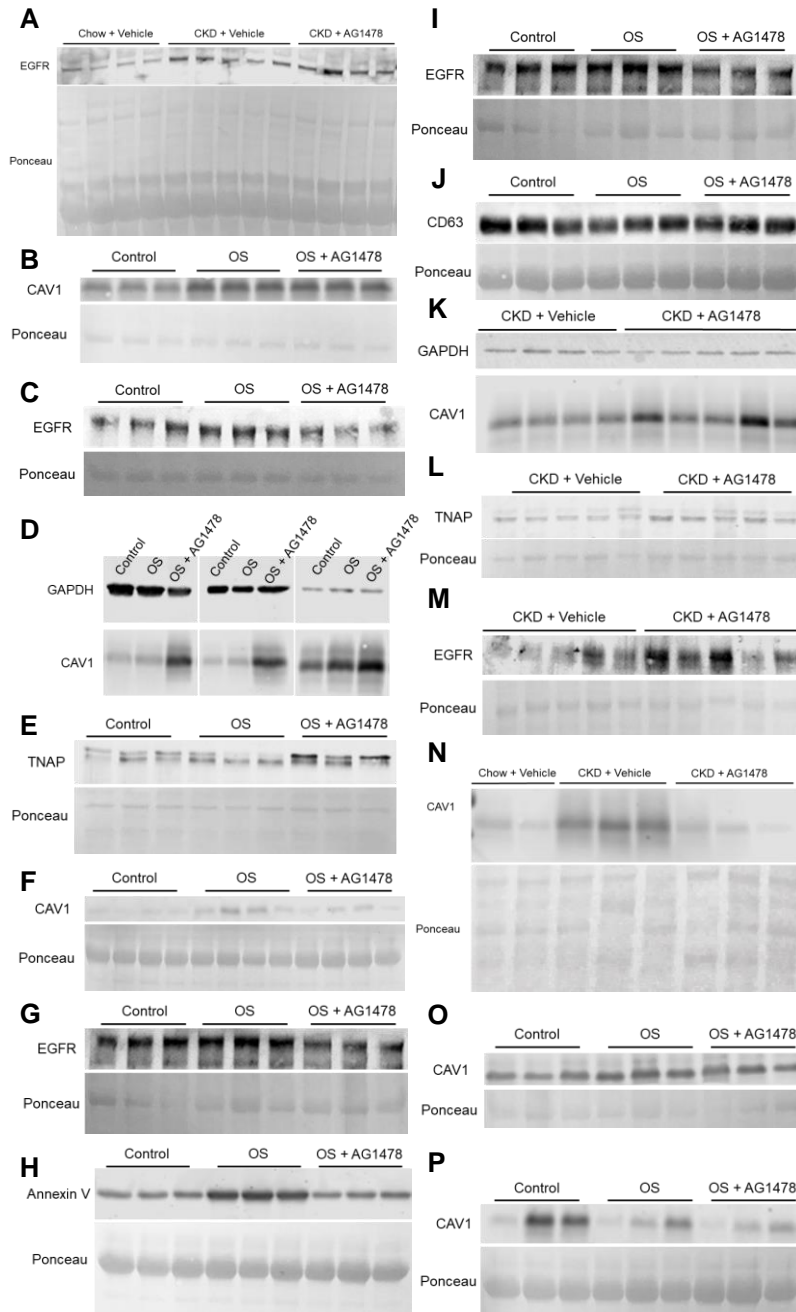
    Image_name = num2str(FileNames{i});
    Fraction_Positive_Matrix{i,1} = Image_name;
    Mean_Intensity_Matrix{i,1} = Image_name;
    Image_string = strcat(File_dir, Image_name);
    Image = fopen(Image_string);
    Image = Image{1,1};
    Image = Image{1,1};
    Image = uint16(Image)*75;
    Image(Image(:)==65535)=0;
    figure, imshow(Image)
    title(Image_name);
    colormap('hot')
    figure, Scale_sample = roipoly(Image);
    Scale_image = double(Image).*Scale_sample;
    Max_pixel = max(max(Scale_image));
    colormap('hot')
    caxis((0 Max_pixel));
    title('Re-scaled Colormap')
    prompt = 'How many specimens are in the image? ';
    n = input(prompt);

    for k = 1:n

        figure, BW = roipoly(Image);
        Calc_image = im2bw(Image,0.3);
        Total_image = im2bw(Image,0.05);
        Calc_image = Calc_image.*BW;
        Total_image = Total_image.*BW;
        figure, imshow(Calc_image)
        figure, imshow(Total_image)
        Calcification_area = sum(sum(Calc_image));
        Total_area = sum(sum(Total_image));
        Percent_positive = Calcification_area/Total_area;
        Fraction_Positive_Matrix{i,k+1} = Percent_positive;
        Double_image = double(Image);
        Masked_image = Total_image.*Double_image;
        Mean_Intensity_Matrix{i,k+1} =
mean(mean(Masked_image))/Total_area;
    end

end
```

## Appendix IV



Blot and Ponceau staining for: (A) serum EGFR, (B) intracellular CAV1 in VSMCs, (C) Intracellular EGFR in VSMCs, (D) VSMCs cytosolic CAV1 and GAPDH, (E) VSMCs cytosolic TNAP, (F) VSMCs EV CAV1, (G) VSMCs EV EGFR, (H) VSMCs EV Annexin V, (I) VSMCs EV EGFR, (J) VSMCs EV CD63, (K) Aorta cytosolic CAV1 and GAPDH, (L) Aorta cytosolic TNAP, (M) Aorta cytosolic EGFR, (N) Aorta EV CAV1, (O) Intracellular CAV1 in HOBs, and (P) HOBs Matrix Vesicles CAV1.

## VITAE

### AMIRALA BAKHSHIANNIK

Born, Tehran, Iran

- 2007-2012      B.S., Materials Engineering  
Iran University of Science and Technology  
Tehran, Iran
- 2007-2012      Full-ride Scholarship  
Iran University of Science and Technology  
Tehran, Iran
- 2012-2015      M.S., Biomedical Engineering  
University of Tehran  
Tehran, Iran
- 2017-2021      Research Assistant  
Florida International University  
Miami, Florida
- 2018 -2022      Doctoral Candidate  
Florida International University  
Miami, Florida
- 2020            *en route* M.S., Biomedical Engineering  
Florida International University  
Miami, Florida
- 2021            Dissertation Year Fellowship Recipient  
Florida International University  
Miami, Florida

U.S. Patent Provisional Patent Application Filed, June 2021, entitled “Targeting Epidermal Growth Factor Receptor in Cardiovascular Calcification”.

A Bakhshian Nik, F Iacoviello, PR Shearing, S Bertazzo, JD Hutcheson, “Time-dependent Role of Bisphosphonates on Atherosclerotic Plaque Calcification”, Journal of Cardiovascular Development and Disease, (under review)

A Bakhshian Nik, HH Ng, P Sun, F Iacoviello, PR Shearing, S Bertazzo, B Khomtchouk, JD Hutcheson, “Epidermal Growth Factor Receptor Inhibition Prevents Caveolin-1-dependent Calcifying Extracellular Vesicle Biogenesis”, Circulation Research, (under full review)

JL Ruiz, JD Hutcheson, L Cardoso, A Bakhshian Nik, et al, S Weinbaum, E Aikawa, “Nanoanalytical Analysis of Bisphosphonate-Induced Alterations of Microcalcifications using a 3D Hydrogel Platform”, Proceedings of the National Academy of Science (PNAS), 118(14), 2021

HH Ng, D Medina, A Bakhshian Nik, JD Hutcheson, “Cellular contraction is required for hyperglycemia-induced vascular calcification”, *Circulation*, 140 (Supp\_1), A16072-A16072

A Bakhshian Nik, JD Hutcheson, E Aikawa, “Extracellular Vesicles as Mediators of Cardiovascular Calcification” *Frontiers in Cardiovascular Medicine*, 4, 2017

A Bakhshian Nik\*, HH Ng, F Iacoviello, PR Shearing, S Bertazzo, JD Hutcheson, “EGFR Inhibition Prevents Vascular Calcification in Chronic Kidney Disease by Modulating Caveolin-1-dependent Extracellular Vesicle Formation”, Poster Presentation, NAVBO Vascular Biology, Virtual Conference, 10/2021

A Bakhshian Nik\*, V Dargam, JD Hutcheson, “In-vitro and In-vivo Assessments of Time-dependent Bisphosphonates Treatment in Development of Cardiovascular Calcification”, Poster Presentation, 51st Biomedical Engineering Society Annual Meeting, Philadelphia, PA, 10/2019

A Bakhshian Nik\*, D Medina, M Garcia Russo, W Heatherly, JD Hutcheson, “The Role of Prestress in Calcification of Human Coronary Artery Smooth Muscle Cells In Vitro”, Poster Presentation, Summer Biomechanics, Bioengineering, and Biotransport Conference, Seven Springs, PA, 06/2019

A Bakhshian Nik\*, V Dargam, JD Hutcheson, “In-vitro and In-vivo Assessments of Time-dependent Bisphosphonates Treatment in Development of Cardiovascular Calcification”, Poster Presentation, Conference of Florida Graduate Schools, Miami, FL, 04/2019

A Bakhshian Nik\*, D Medina, JD Hutcheson, “Glucose-mediated Smooth Muscle Cell Contraction Is Required for Calcification In Vitro”, Podium Presentation, 50th Biomedical Engineering Society Annual Meeting, Atlanta, GA, 10/2018

A Bakhshian Nik\*, JD Hutcheson, “Effect of Biomechanical Environment on Vascular Calcification”, Podium Presentation, 20th Biomedical & Comparative Immunology Symposium, Miami, FL, 03/2018